CZECH TECHNICAL UNIVERSITY IN PRAGUE

Faculty of Civil Engineering
Experimental Centre

Development of high-load-bearing energy-absorbing system with controlled deformation

DOCTORAL THESIS

Ing. Petr Hála

Ph.D. Programme: Civil Engineering
Branch of study: Constructions and traffic structures

Supervisor: Assoc. Prof. Radoslav Sovják

Prague, 2020

Declaration of Authorship

PhD student's name: Petr Hála

Title of the PhD Thesis: Development of high-load-bearing energy-absorbing system with controlled deformation

I declare that I have prepared this PhD Thesis independently under the guidance of the supervisor Assoc. Prof. Radoslav Sovják.

I have always clearly attributed where I have consulted the published work of others, I have given the source of each quotation, and I have acknowledged all main sources of help.

Date: _____

Signed: _____

CZECH TECHNICAL UNIVERSITY IN PRAGUE

Abstract

Faculty of Civil Engineering

Experimental Centre

Doctor of Philosophy

Development of high-load-bearing energy-absorbing system with controlled deformation

by Petr Hála

Even though the number of deadly traffic incidents is decreasing, the proportion of motor vehicle crash deaths involving a collision with fixed objects is not. To address this issue and consequently to decrease transportation hazards, a novel load-bearing energy-absorbing system (EAS) comprised of brittle blocks with cellular structures is presented here. The brittle blocks are designed as cushioning elements dissipating the impact energy because of the gradual brittle fracture process in their cellular structures with their cell walls serving as supporting elements. The EAS is subjected to a testing program involving a quasi-static load generated by a hydro-static loading machine and impacts of a 50 kg flat-nosed impactor, a 1,000 kg flat-nosed cart, and a 1,100 kg passenger vehicle. During the conducted car crash test, the crumple zone of the car was not crumpled; car bounce of was eliminated and gradual deceleration of the car was recorded. It is demonstrated that EAS is able to gradually absorb different levels of impact energy by combining blocks with different crashworthiness, and the comparative study on the crashworthiness of blocks with different cellular structures is presented. It is shown that relatively small changes in the design can lead to the production of blocks with distinguishable levels of crashworthiness and several observations that could guide future crashworthiness design are given. High-performance concrete (HPC) is proposed as a base material and the production process of such EAS is presented. Use of HPC makes EAS suitable for use in harsh environments while still keying an eye towards reasonable production costs and the ability to be mass-produced. All components of the HPC employed are commonly available in large volumes for a reasonable price, and the resulting material is characterised by reasonable volume stability and very low porosity, which makes it highly durable. These specifications allow for a wide range of applicability even in places where currently produced energy-absorbing systems cannot be installed. The focus is on replacing stones and solid blocks in cross-drainage culverts by the proposed EAS as cushioning element, but hypothetically it could also be used in other structures which pose risks around traffic lanes or in underwater protection of bridge piers. Proper EAS functionality is demonstrated using experimental methods and validated by numerical simulations. The developed numerical models are able not only to replicate the motion of the impacting body but also the gradual fracture process of the cellular structure and can be used in future research. This thesis additionally laid the cornerstone for cooperating with a private sector partner.

ČESKÉ VYSOKÉ UČENÍ TECHNICKÉ V PRAZE

Abstrakt

Fakulta stavební

Experimentální centrum

Disertační práce

Vývoj vysoce únosného energii absorbujícího systému s kontrolovanou deformací

Petr Hála

Přestože počet smrtelných dopravních nehod klesá, podíl kolize motorového vozidla s pevnou překážkou na počtu úmrtí zůstává neměnný. Za účelem snížení závažnosti těchto nehod a s tím spojených rizik silniční dopravy je v této práci představen nový nosný systém pohlcující energii složený z křehkých bloků s buněčnými strukturami. Tyto bloky jsou navrženy tak, aby pohlcovaly rázovou energii pomocí postupného křehkého kolapsu jejich buněčných struktur, přičemž jejich buněčné stěny mohou sloužit jako nosné prvky. Navržený absorbér byl podroben testovacímu programu, který zahrnoval kvazistatické zatížení generované hydrostatickým zařízením a nárazy 50kg závaží s plochým čelem, 1000kg vozítka s plochým čelem a 1100kg osobního vozidla. Během nárazu osobního automobilu nedošlo ke zmáčknutí deformačních zón vozidla, byl odstraněn zpětný ráz a vozidlo bylo postupně zpomaleno. Bylo demonstrováno, že absorbér složený z bloků s rozdílnou odolností proti nárazu je schopen absorbovat různé úrovně kinetické energie. Tato práce zároveň obsahuje srovnávací studii nárazové odolnosti bloků s různými buněčnými strukturami. Bylo ukázáno, že relativně malé změny v buněčné struktuře mohou vést k výrobě bloků s rozlišitelnou úrovní odolnosti proti nárazu a bylo uvedeno několik poznatků, které by mohly být použity během budoucího návrhu bloků. V rámci této práce je představen výrobní proces absorbéru vyrobeného z vysoce hodnotného betonu. Využití tohoto materiálu zaručí absorbéru dostatečnou životnost v nepříznivých prostředích, přičemž jeho výrobní náklady zůstanou přiměřené a bude možné jej sériově vyrábět. Všechny složky použité během výroby jsou běžně dostupné ve velkých objemech za rozumnou cenu a výsledný materiál se vyznačuje dostatečnou objemovou stabilitou a velmi nízkou porozitou, díky čemuž je vysoce odolný. Tyto specifikace umožňují širokou škálu použití a to i v místech, kde nelze instalovat doposud známé absorbéry. Záměrem je nahradit kameny a pevné bloky v propustcích navrhovaným absorbérem, ale hypoteticky by tento absorbér mohl být také použit v jiných konstrukcích, které představují rizika kolem silničních cest nebo při ochraně mostních pilířů pod vodou. Správná funkčnost absorbéru byla demonstrována pomocí experimentálních metod a ověřena numerickými simulacemi. Vyvinuté numerické modely dokážou nejen simulovat pohyb narážejícího tělesa, ale také postupný kolaps buněčné struktury a mohou být použity v rámci budoucího výzkumu. Tato práce zároveň položila základní kámen pro spolupráci se soukromým sektorem.

Acknowledgements

I would like to sincerely thank my supervisor, Radoslav Sovják, for entrusting me with this topic, for his friendly support, and for securing funding. At the same time, I would like to thank the head of the Experimental Centre, Petr Konvalinka, for creating excellent conditions in the workplace and for enabling my internships abroad.

I also gratefully acknowledge the help of the co-authors of the three research articles, of which this dissertation consists. Specifically, I would like to thank my colleagues from the Faculty of Transportation Sciences, Tomáš Mičunek, Luboš Nouzovský, and Michal Frydrýn, for securing funding and conducting full-scale crash tests. I would also like to thank Michal for recording reduced-scale impact tests with a high-speed camera. Many thanks go to Petr Máca from the Technical University of Dresden for consulting on data filtering and for proofreading Chapter 3.

I would like to extend my thanks to Stephanie Krueger from the Czech National Library of Technology for proofreading Chapters 2 and 3 and giving me useful advice concerning my first presentation overseas.

During my internships, I was fortunate to meet scientists, to whom I also want to express my gratitude here. Although they did not directly influence this work, I gained a lot of experience under their supervision, which I subsequently used in working on this thesis. Namely, I would like to thank Fan Sau Cheong and Paolo Del Linz from Nanyang Technological University in Singapore; Jean-Philippe Charron and Najib Bouaanani from École Polytechnique de Montréal in Canada; and Jos Brouwers from the Eindhoven University of Technology in the Netherlands.

Contents

List of Figures

List of Tables

List of Abbreviations

α	Alpha version of EAS made of FC
β	Beta version of EAS made of HPC
CFC	Channel Frequency Class
CSCM	Continuous Surface Cap Model
EAS	Energy Absorbing System
F30	Sample cut out of ceramic brick Heluz Family 30
F44	Sample cut out of ceramic brick Heluz Family 44
F50	Sample cut out of ceramic brick Heluz Family 50
FC	Fired Clay
HPC	High Performance Concrete
K&C	Karagozian & Case Concrete Model
MK	Sample cut out of ceramic brick Heluz AKU MK 36.5
P15	Sample cut out of ceramic brick Heluz P15 30
RH	Relative Humidity
RHT	Riedel, Hiermaier, Thoma Model
STI44	Sample cut out of ceramic brick Heluz STI 44
+40	Sample cut out of ceramic brick Heluz Plus 40
+44	Sample cut out of ceramic brick Heluz Plus 44

List of Symbols

a	deceleration of impactor	$\mathrm{m/s^2}$
A_j^+	ideal alternative	
A_j^-	negative ideal alternative	
CE	crush efficiency	dimensionless
$CE_{\max}$	maximum crush efficiency	dimensionless
CFE	crush force efficiency	dimensionless
D_i^+	sums of beneficial alternatives	
D_i^-	sums of non-beneficial alternatives	
$D_{\min}^-$	minimum of D_i^-	
EA	energy absorption	J
EAE	energy absorption efficiency	J/N
EE	energy efficiency	dimensionless
E_k	kinetic energy of impactor	J
F	instantaneous crushing force	N
i	a row of a matrix	
j	a column of a matrix	
L	length of EAS	m
m	mass of EAS	kg
m_0	mass of impactor	kg
MCF	mean crush force	N
PCF	peak crush force	N
R	normalised evaluation matrix	
r_{ij}^+	beneficial design criteria	
r_{ij}^-	non-beneficial design criteria	
S	relative significance	
$S_{\max}$	maximum of S	
SEA	specific energy absorption	J/kg
t	time	s
u	instantaneous crushing stroke	m
U	quantitative utility	dimensionless
u_{eff}	effective crush stroke	m
$u_{\max}$	maximum crush stroke	m
v	velocity of impactor	m/s
V	volume of EAS	$\mathrm{m^3}$
$VSEA$	volume specific energy absorption	$\mathrm{J/m^3}$
WE	work effectiveness	J/kg
X	evaluation matrix	
x_{ij}	entry of X	

Chapter 1

Introduction

1.1 Aim of the thesis

Aim of the thesis is to develop an energy-absorbing system (EAS) that

1. dissipates the impact energy,
2. has sufficient load-bearing capacity in the direction perpendicular to the expected impact,
3. has reasonable production cost,
4. is suitable for mass production and
5. for use in harsh environments.

These specifications will allow for a wide range of applicability even in places where currently produced energy-absorbing systems cannot be installed. The focus is on replacing stones and solid blocks in cross-drainage culverts by the proposed EAS as cushioning element, but hypothetically it could also be used in other structures which pose risks around traffic lanes or in underwater protection of bridge piers.

1.2 Content of the thesis

The thesis is a collection of three full-length research articles published in peer-reviewed international journals indexed in Web of Science and Scopus and placed in the top quartile Q1. All these three articles are closely related to the development of a high-load-bearing energy-absorbing system (EAS) with controlled deformation and together form comprehensive publication. In these articles, the author of the thesis carried out most of the studies, including the formulation of methodologies, conducting experimental and numerical analyses, interpretation of results, and drafting the manuscripts. The co-authors contributed mainly to securing funding, conducting full-scale crash tests, and reviewing the manuscripts. The specific role of each co-author is given in the "Acknowledgements" section. Introducing and concluding chapters are also included to supplement the standalone articles.

This chapter gives an overview of the literature and explains the motivation behind the development of the novel EAS. Notable types of existing EAS related to the one developed within the framework of this thesis are mentioned. This includes brittle EAS made of high-performance concrete that absorbs impact energy by brittle fracture process and plastic EAS that absorbs impact energy because of a gradual collapse of its laterally loaded cells. These studies are essential for understanding experimental and assessment methodologies used in this work and are, therefore, listed in the Section 1.3. Research

significance is discussed in Section 1.4. The statistics showing the number of traffic incidents involving a collision with fixed objects in the Czech Republic and abroad are given. Fixed objects are ordered by the number of associated crash deaths. Collisions with cross-drainage culverts are described in detail by defining the different accident scenarios and the severity of their consequences. The current safety treatments for cross-drainage culverts are also discussed.

The next chapter (reproduced from [1]) presents an alpha version of the energy-absorbing system that was built into culvert embedded in the ground. This version has fulfilled all the requirements mention in Section 1.1 with the exception of durability. It is comprised of commercially available fired clay blocks with trimmed longitudinal sides to eliminate tongue and groove joints. The ability of these deformation blocks to absorb impact energy because of the gradual brittle fracture process which occurs in their cellular structures is demonstrated and their load-bearing capacities are verified. Based on two non-deformable flat-nosed cart impact tests, it is showed that it is possible to design a specimen composed of brittle blocks with cellular structures able to gradually absorb different levels of impact energy by combining elements of different stiffness. In order to determine the ability of blocks to gradually absorb the kinetic energy of vehicular impact, two full-scale field crash tests involving passenger vehicles with crumple zones were conducted. During these experiments, an ordinary passenger vehicle frontally impacted a reinforced concrete wall and a specimen comprised of deformation blocks. It is demonstrated that the severe consequences of a collision with cross-drainage culverts can be significantly reduced by using brittle blocks with cellular structures as cushioning elements. In fact, the crumple zone of the passenger vehicle which collided with a brittle block culvert was not crumpled; vehicle bounce off was eliminated and gradual deceleration of the vehicle was recorded.

The third chapter (reproduced from [2]) lays the foundation for the assessment of the crashworthiness of brittle blocks with cellular structures. Six fired clay blocks were subjected to quasi-static and impact tests. The experiments were conducted using a hydro-static loading machine equipped with stationary and movable steel plates and an impact pendulum machine with a flat-nosed impactor travelling in a circular trajectory and hitting the specimen at the bottom-return point. The responses of blocks are compared based on force-displacement curves and indicators of crashworthiness. The gradual brittle fracture process which occurs in a cellular structure is studied in detail. Blocks with different levels of crashworthiness are identified for subsequent studies and several observations that could guide future crashworthiness design are given. It is shown that relatively small changes in the design can lead to the production of blocks with distinguishable levels of crashworthiness.

Unfortunately, the considered fired clay blocks have a limited lifetime in harsh environmental conditions and may, therefore, fail during the service life of a structure. Therefore, the fourth chapter (reproduced from [3]) introduces a beta version of the energy-absorbing system where durability is provided by the use of high-performance concrete (HPC) as the base material. The HPC employed is a self-consolidating concrete with fast strength development. It does not require heat curing or special mixing techniques. All its components are commonly available in large volumes for a reasonable price, and the resulting material is characterised by reasonable volume stability and very low porosity, which makes it highly durable. The deformation blocks were produced in the lab using a special mould with the perforated bottom and subjected to a complete testing program. A full-scale specimen was subjected to the impact of a non-deformable flat-nosed cart with initial conditions identical to those in Chapter 2. A reduced-scale specimen was subjected to the impact of a flat-nosed impactor with initial conditions identical to those

in Chapter 3. The load-bearing ability of the block in the direction perpendicular to the expected impact was verified using a reduced-scale specimen and a hydro-static loading machine. The experiments are validated by numerical analyses. The developed numerical models are able not only to replicate the motion of the impacting body but also the gradual fracture process of the cellular structure. It is concluded that the developed deformation block can be used as a structural element in cross-drainage culverts.

In the last chapter, both versions are compared, conclusions drawn, and potential extensions and outlooks for future work are discussed.

The findings of this thesis were presented at the Second International Interactive Symposium on Ultra-High Performance Concrete in Albany, New York [4]. Cooperation with a private sector partner has been established in the area of product development and manufacture and is supported by the Technology Agency of the Czech Republic [grant number TH04010066].

1.3 State of the art

During impact, the kinetic energy of the impacting body can be transformed into other forms of energy by means of energy absorbing systems (EAS). The transformation process can be reversible or irreversible depending on the type of the material used and the construction of the particular system. As an example of the reversible process would be a shear thickening fluid [5–11] that dissipates impact energy due to shear thickening behaviour. The irreversible process can be illustrated by a progressive EAS collapse when kinetic energy is gradually removed from an impacting object with controlled damage to the EAS. The irreversible transformation process can be further divided into brittle and plastic absorbers used in an EAS.

1.3.1 Brittle energy absorbing systems

Notable types of brittle EAS include a hollow concrete masonry unit made of frangible concrete introduced by O'Neil et al. [12] to reduce blast-related casualties. The frangible concrete they developed is a high-performance concrete that breaks into small pieces when it fractures. It absorbs impact energy through the process of fracturing and by loss into the atmosphere. This unit was designed specifically for use in perimeter security walls to eliminate the potential of lethal fragments of broken concrete to be generated by a blast force from a terrorist vehicle bomb.

Shen et al. introduced in [13] a safety block made of a no-fine concrete solidified by an alkali-activated slag. Due to the presence of the slag, heat treatment, and optimised gradation of aggregate, a network of micro-cracks throughout the volume of the block was developed. Under quasi-static loading, the safety concrete behaved like normal concrete. However, under impact loading, the micro-cracks propagated, connected, and disintegrated the safety block into fragments smaller than 4.7 mm. It was reported that a highway crash barrier made of such concrete could reduce the velocity of an impacting vehicle and thus protect vehicle passengers.

Brittle fracture has also been recorded during the axial collapse of fibre reinforced composite tubes [14].

1.3.2 Plastic energy absorbing systems

Although the energy absorbing process has not, to the author's knowledge, been studied when brittle energy absorbers are impacted parallel to the longitudinal axis of their cells, many authors have studied the axial collapse of metallic thin-walled tubes with openings (with patterned windows or made of expanded metal) or the lateral collapse of metallic tubes. Their studies are essential for understanding experimental and assessment methodologies used in this work and are, therefore, listed below. It was also reported in [15] that tubes exhibit a different way of absorbing energy during lateral crushing and bending tests and therefore, these two loading conditions should be studied separately.

1.3.2.1 Axially loaded tubes with patterned windows

Song et al. introduced [16] lightweight thin-walled structures with patterned windows and conducted a parametric study to investigate the effect of the size of the window on the tube's collapse characteristics. They demonstrated that the introduction of the window to the tube could significantly reduce the peak crush force without significant reduction of energy absorption. However, it was also noted [17] that windowed tubes can achieve higher average crush forces. Recently, Nikkhah et al. [18] investigated the crushing responses of tubes with circular, rectangular, square, hexagonal, convex, and elliptical windows under axial and oblique loading conditions and found that tubes with square and rectangular windows have the most desirable overall crushing performance.

1.3.2.2 Axially loaded tubes made of expanded metal

Graciano et al. [19] introduced square and round tubes made of expanded metal sheeting. Theoretical and numerical models were later developed in [20] and validated with experimental values. Using these models, a parametric analysis was conducted in order to investigate the relationship between cell geometry and load-displacement response. In a follow-up work, Martínez et al. [21] investigated the influence of the length-to-diameter ratio. Smith et al. [22] investigated an enhancement in energy absorption characteristics due to the flattening of expanded metal. In a subsequent work, Borges et al. [23] investigated the impact response of tubes made from expanded metal sheets and found that their collapse mode changes with impact velocity. For lower impact velocities, the deformed shapes resembled a quasi-static case. Jahromi and Hatami [24] showed that by placing concentric expanded metal tubes within each other, the crashworthiness of a system can be increased. Hatami et al. [25] studied the response of tubes made of flattened expanded metal under impact loading using experimental, numerical, and analytical approaches.

1.3.2.3 Laterally loaded simple metallic tubes

Among tubes loaded laterally, the circular tube is the most investigated shape [26]. Avalle and Goglio [27] experimentally and numerically analysed circular aluminium tubes under quasi-static lateral compression and found that the Reid-Reddy theoretical model realistically described the collapse process. Lateral collapses of circular tubes with different displacement to thickness ratios were investigated by Gupta et al. [28] who found that as the ratio increases, the energy absorption decreases. The mode of deformation remains unaffected. With an increase in the tube thickness, the energy absorbing capacity and the average crush force increases. With an increase in the diameter of a tube, the energy absorption and the average crush force tends to decrease. The dynamic lateral crushing behaviours of circular tubes was studied by Fan et al. [29] and Xu et al. [30]. Fan et

al. [29] examined tubes loaded with a constant velocity and observed a considerable increase in energy absorption for higher velocities. Xu et al. [30] studied the lateral impact of flying tubes upon a rigid target and stated that larger initial velocity leads to a larger peak force magnitute. The crashworthiness optimisation of circular tubes was presented by Baroutaji et al. [31].

Oblong tubes were studied by Baroutaji et al. [32] who found that an oblong tube has almost the same magnitude of collapse load as a circular tube and that the post-collapse stage is more stable due to the residual stresses created during formation of the oblong tube.

Gupta et al. [33] experimentally and numerically investigated square and rectangular metallic tubes and found that a square tube absorbs more energy than a rectangular tube with an equal cross-sectional area. They also observed that energy absorption increases as tube thickness increases and that it is not significantly affected by the friction coefficient between a tube and compressing plates. Niknejad et al. [34] derived theoretical relations to predict energy absorption and the instantaneous crush force during lateral compression of square and rectangular tubes. Tran and Ton [35] presented theoretical relations to predict an average crush force and conducted lateral compression tests to verify the formulas.

Niknejad and Rahmani [36] experimentally tested hexagonal tubes under lateral quasi-static loading and introduced a new analytical model for their plastic deformation during the flattening process. They found that crushing force is proportional to tube length and is dependent on the second power of tube wall thickness.

Wang et al. [37] studied the collapse mechanisms and energy absorbing abilities of triangular tubes under lateral compression. A plastic model including six plastic hinges and one travelling plastic hinge was proposed and the authors reported that this model captures the collapse process and consistently predicts the average crush force. In a follow-up work, Fan et al. [38] focused on the response of equilateral triangular tubes which, using numerical analysis, confirmed and supported the previous conclusions. Recently, Tran [39] experimentally analysed multi-cell triangular tubes and investigated their lateral crushing behaviours, finding that the average crush force is governed by its plastic hinge lines and is dependent on the flow stress of a material, its wall thickness, and tube length.

Researchers have been improving the laterally loaded metallic tubes and have proposed many modifications such as an addition of exterior constraints [32, 40, 41], a self-locked system [42, 43], nested tubes [40, 44–51], and foam-filled tubes [26, 29, 36, 51].

1.3.2.4 Laterally loaded constraint tubes

Reddy and Reid [41] studied the quasi-static lateral compression of a constrained tube. They introduced side constraints to the tube so that its horizontal diameter could not increase. This encouraged the tube to deform in alternative modes involving more plastic hinges. Baroutaji et al. [32] examined the influence of inclined and vertical constraints on the energy absorption characteristics of oblong tubes and found that exposing the oblong tubes to external constraints allowed more volume of the oblong tube to be deformed and that energy absorption, as well as crushing force, increased.

1.3.2.5 Laterally loaded self-locked system

Chen at al. [42] introduced a novel self-locked energy absorbing system composed of thin-walled tubes with a dumbbell-shaped cross section and demonstrated its ability to gradually reduce impact force. The self-locked system prevented lateral splash from impact loading without any constraints. In a follow-up work, Yang et al. [43] proposed an internally nested self-locked energy-absorbing system in which small round tubes were nested into a dumbbell-shaped outer tube. This modification significantly improved energy absorption properties of the system.

1.3.2.6 Laterally loaded internally nested tubes

Morris et al. [40], for example, studied nested metallic tube type energy absorbers consisting of three tubes of varying diameter placed within each other with their axes being parallel. The authors analysed its response under quasi-static loading with vertical and inclined side exterior constraints. It was shown that although the constraints increase the specific energy absorption of the system, crush efficiency suffers as a consequence and hence weight effectiveness is reduced. In follow-up works, the authors have presented two different modifications to the system. It was demonstrated [45] that an elliptical shape tube system has greater energy absorbing capacity than circular counterparts due to greater displacement stroke. It was also shown [46, 47] that once the collapse load was reached, the crushing force could be kept relatively constant by adding cylindrical rods between the gaps of the tubes. Later, these two modifications were combined to create the nested oblong tube energy absorber [48] and the oblong tubes were subjected to crashworthiness optimization [32].

Wang et al. [49] proposed a theoretical model for an internally nested circular tube system under lateral impact loading and verified predictions of displacement and reaction force using numerical and experimental analyses. By using the multi-tube system, the force–time curves of the system exhibited a staircase pattern due to the contacts between the tubes. Baroutaji at al. [50] proposed nested systems in the form of short, internally stacked circular and oblong tubes. Niknejad and Orojloo [51] introduced a longitudinal grooved nested system of tubes with a special cross-section and experimentally investigated the influence of the inner tube on energy absorption behaviour and the deformation mode.

1.3.2.7 Cellular structures

Tubes can be bonded to each other to form a cellular structure. Papka and Kyriakides [52] studied in-plane crushing of close-packed polycarbonate circular tubes and found that the length of the bond has a stiffening effect on the compressive response. The researchers analysed the compressive responses under displacement controlled loadings at six different end-displacement rates and found that because of the rate dependence of the material the crushing stress increases as the rate of crushing is increased. At the same time, the extent of the stress plateau remains essentially unaffected by loading rate. In follow-up work, they [53] studied the in-plane mechanical behaviour of hexagonal aluminium cellular structures quasi-statically crushed between parallel rigid surfaces and found that the crushing stress and extent of the stress plateau are relatively unaffected by the size of the specimen. Later, they conducted the experimental study of biaxial crushing of circular polycarbonate cellular structures [54] and validated it with numerical analysis [55]. They demonstrated that the prevalent mechanisms of collapse and the energy absorption capacity depend on the ratio of biaxial loading rates and that the highest

crushing energy is required when these rates are equal. They also showed that the energy absorption capacity of the specimen under the confined uniaxial test is more than 9% higher than under the pure uniaxial test. The shape of the crushing band was observed to be affected by the cell alignment [54].

Ruan et al. [56] numerically analysed the dynamic crushing of hexagonal aluminium cellular structures and investigated the influence of cell wall thickness and impact velocity on the mode of deformation and the plateau stress. For different values of cell wall thickness and impact velocity, they identified three different deformation modes, each having different shape of crushing band. Zheng at el. [57] followed up on their study and noted that the shape of the crushing band at low velocities is also highly sensitive to the details of boundary conditions and specimen height-to-width ratio. They further extended the study by the influence of the cell irregularity. In both studies [56, 57], the plateau stress was found to increase with the crushing velocity. Zou et al. [58] compared the numerical prediction of dynamic crushing of hexagonal cellular structures with a one-dimensional shock theory [59] based on a rigid-perfectly plastic-locking stress-strain curve and proposed a modification of this theory. They also showed that in contrast to the crushing stress at the impacted end of cellular structure which increases with the crushing velocity, crushing velocity has much less effect on the stress at the supported end over the entire crushing process. This effect of loading rate on crushing stress was also mentioned by Ma et al. [60], who investigated it on a mesoscale numerical model based on Voronoi tessellation. They found that the crushing stress at the impacted end increases with loading rate primarily due to the inertia effect of cell wall motions. The crushing stress at the supported end was proven to be insensitive to loading rate unless the base material is strongly rate dependent. Hu and Yu [61] conducted a numerical study of hexagonal cellular structures and confirmed that the crushing stress at the impacted end increases with impact velocity, but also showed that the crushing stress at the supported end decreases at the same time. They defined these stresses as functions of impact velocity, cell dimensions, and the mechanical properties of the base material, and derived the analytical formula on the critical velocity determining the boundary between low-velocity and high-velocity impacts. Ajdari et al. [62] demonstrated that irregular cellular structures have energy absorption similar to their regular counterparts of the same relative density and mass. They also showed that the cell wall size had no significant effect on the crushing response of a regular hexagonal cellular structure as long as its relative density was kept constant. Decreasing the relative density in impact direction was found to enhance the energy absorption in the early stages of a high-velocity crushing. This enhancement is connected to the joint crush of cells adjacent to the impact mass and thin cells adjacent to the support. According to the analytical model [63] based on the shock-wave theory, crushing stress can be decreased by designing a cellular structure with increasing relative density in impact direction. Qiao and Chen [64] introduced a hexagonal cellular structure with cell walls consisting of an equilateral triangular cellular structure and found that while this hierarchical design shows higher quasi-static and low-velocity crushing stresses compared to traditional hexagonal and triangular cellular structure, its effect on high-velocity crushing stress is negligible.

1.4 Research significance

Energy-absorbing systems such as a cross-beam of an automobile bumper [51] or front longitudinal rails [65–67] are being constantly improved and widely used to dissipate the impact energy during collisions. Unfortunately, even though the number of deadly traffic incidents is decreasing, the proportion of motor vehicle crash deaths involving a

collision with fixed objects has remained between 19% and 23% since 1979 in the USA (Figure 1.1) according to the U.S. National Highway Traffic Safety Administration [68]. These roadside hazards are equally serious in the Czech Republic where one-fifth of all traffic accidents (Figure 1.2) and one-fourth of fatal traffic accidents (Figure 1.3) are caused by a collision of a vehicle with fixed objects [69]. This indicates that not enough attention has been paid to the crashworthiness of fixed objects and that by addressing this issue, transportation hazards could be significantly decreased.

Reasons, why a vehicle leaves a traffic lane and collides with fixed objects, include avoiding a collision with oncoming vehicles, sleep-deprived driving, vehicle skidding or unsafe overtaking [69]. This sudden lane departure cannot always be prevented, as it is often the only solution to avoid a pileup. If a vehicle leaves a road, all fixed objects in its vicinity present an imminent danger to its occupants. These objects can be divided into natural objects, such as trees, and artificial objects, such as traffic lights, barriers, noise protection walls, or cross-drainage culverts. Cross-drainage culverts are the fifth most common fixed artificial object struck (Figure 1.4); collision with such culverts as currently designed is comparable to frontal impact with a rigid wall, because a car leaving a road with drainage ditches is directed—via the ditches—straight into a culvert face.

In the Czech Republic, many culverts are clogged and even though they do not fulfil their function, they are not removed or repaired after the collision (Figure 1.5) [69]. According to a survey of 315 cross-drainage culverts in the Central Bohemia region of the Czech Republic [69], 36 vehicles collided with cross-drainage culverts during years 2006 and 2007. In these accidents, 59 people were injured: 32 of them slightly, 19 seriously and 8 passengers succumbed to their injuries. Two accidents caused car fire and one driver burned to death. It can be concluded that almost half of the injuries related to a vehicle colliding with a cross-drainage culvert are fatal or serious (Figure 1.6).

Based on an in-depth analysis of survey data [69], three basic accident scenarios have been defined. In the most common scenario, a vehicle leaves a traffic lane in the immediate vicinity of a cross-drainage culvert and hits the culvert with the edge of the front bumper. The impact energy is not absorbed by the crumple zones but is converted to deformation energy which dislocates and deforms the front wheel suspension and pushes the front wheel against the bodywork. This type of deformation usually causes widespread damage to the vehicle body and severe injuries of vehicle passengers, who often cannot abandon the vehicle unassisted. The second most common scenario is a frontal impact where a vehicle is directed via the ditch straight into a culvert face. During this scenario, the kinetic energy is more or less absorbed by the crumple zones. In the event of an eccentric impact, a vehicle rollover can occur. In the least common scenario, the front tire or the lower front bumper edge hits a cross-drainage culvert. This type of accident usually does not cause severe injuries but is accompanied by serious damage to the vehicle, often irreparable.

It was also noted in [69] that a collision with culverts located in a ditch on the right side of the road occurred only in 55% of cases, and with those located in a ditch on the left side of the road in 45% of cases. This leads to the conclusion that it is necessary to secure both the front and rear face of culverts.

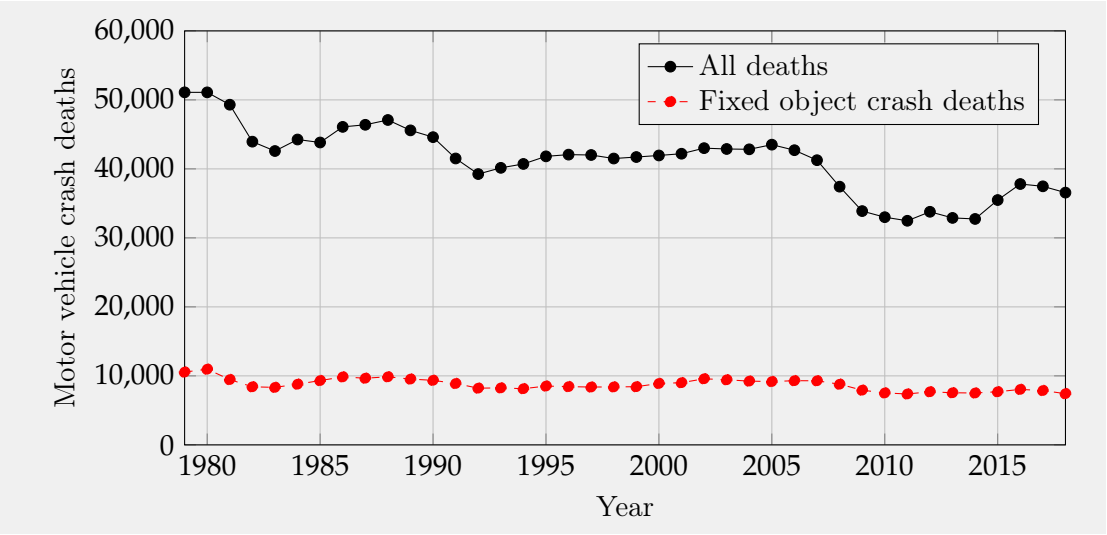

Figure 1.1: Motor vehicle crash deaths in USA in the years 1979–2018. [70]

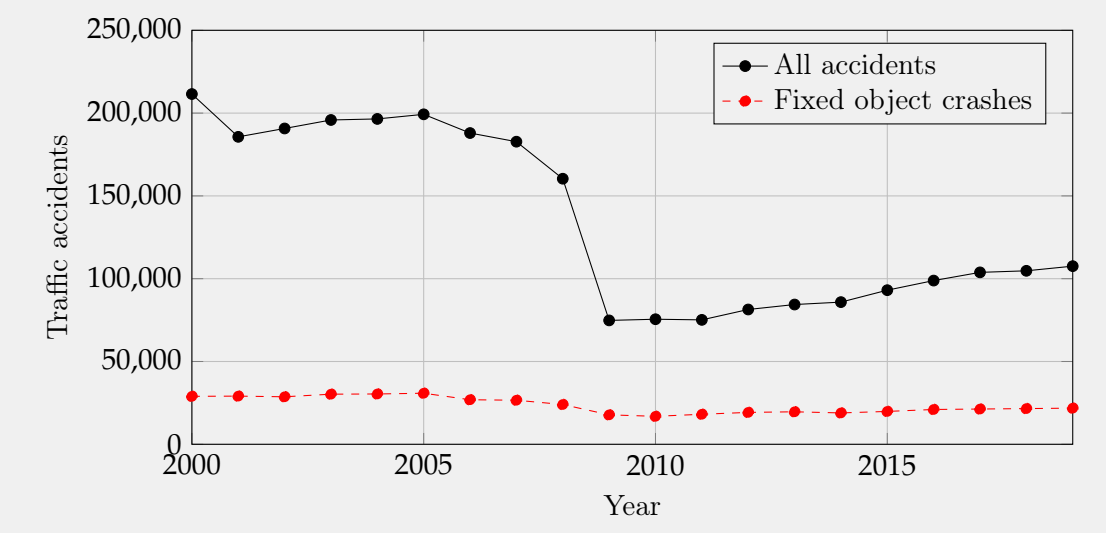

Figure 1.2: Traffic accidents in the Czech Republic in the years 2000–2019. [71]

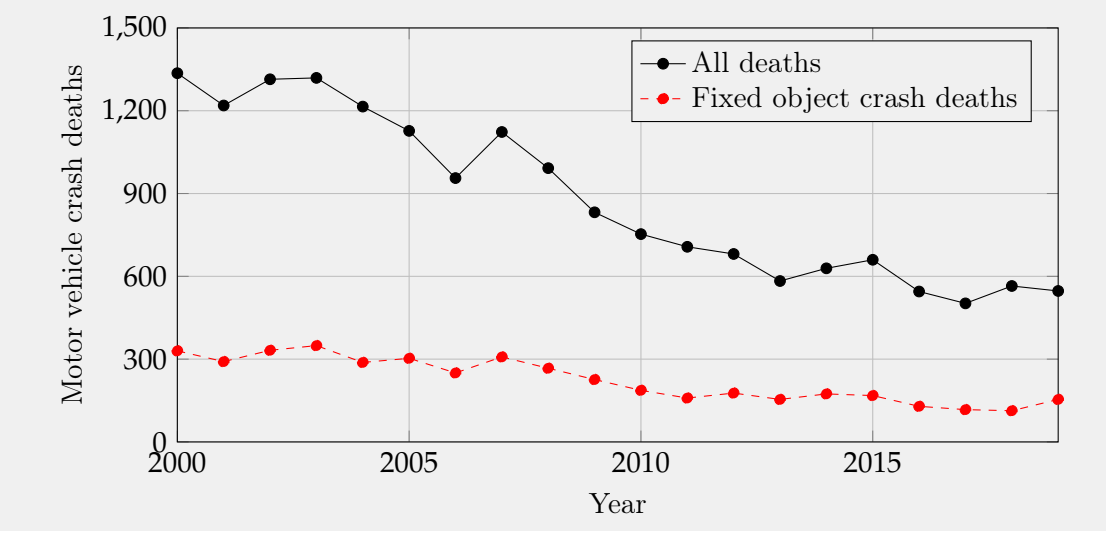

Figure 1.3: Motor vehicle crash deaths in the Czech Republic in the years 2000–2019. [71]

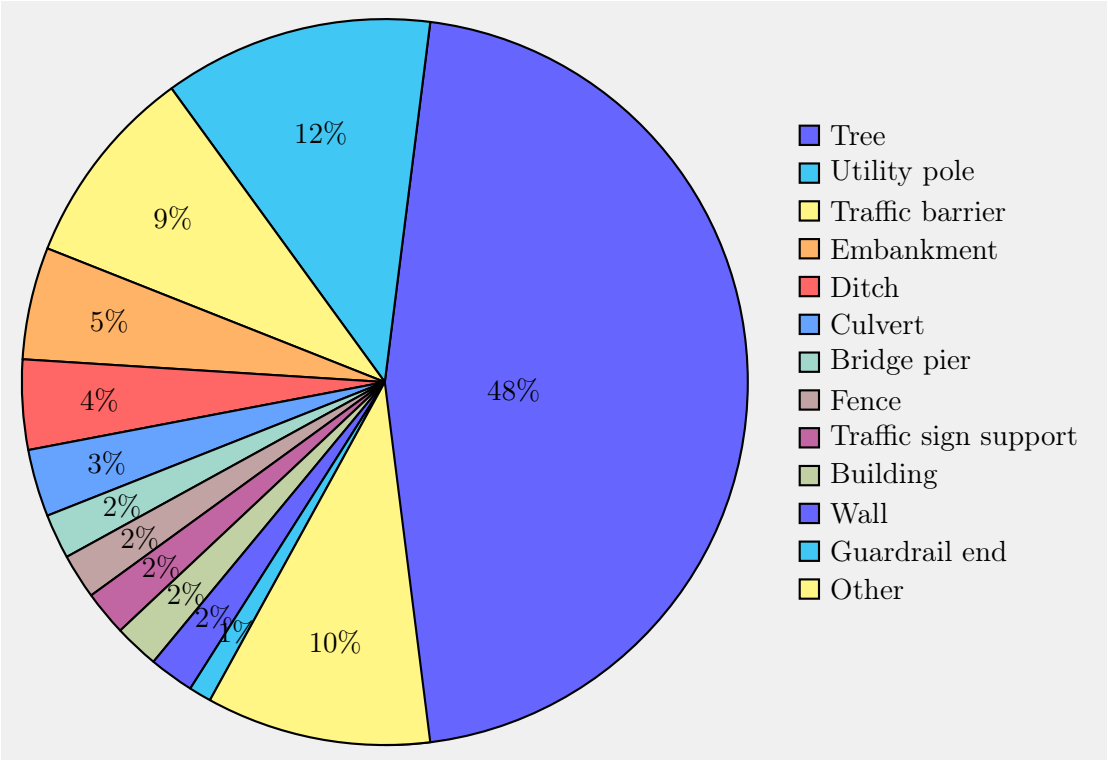

Figure 1.4: Percent distribution of fixed-object crash deaths by object struck in USA in 2018. [70]

Figure 1.5: Example of a cross-drainage culvert. [1]

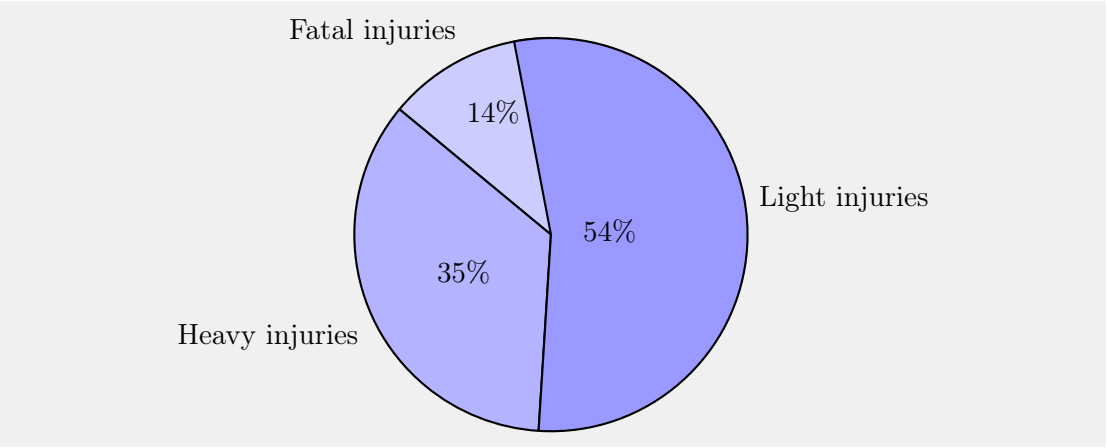

Figure 1.6: Injuries related to a vehicle colliding with a cross-drainage culvert in the Central Bohemia region of the Czech Republic in 2006 and 2007. [69]

Safety treatments for roadside cross-drainage culverts include relocating a culvert, placing a guardrail, bevelling a culvert, placing an energy-absorbing system in front of a culvert, and using load-bearing cushioning elements in culverts. It was argued in [69] that relocating cross-drainage culverts would not significantly decrease the number of accidents since the accident sites were distributed over the entire road network. A guardrail could be installed to prevent lane departure and subsequent collision with the culvert. However, lane departure is sometimes the only way to avoid a collision with an oncoming vehicle and the introduction of this measure could lead to pileups. It was also noted in [72] that the installation of long guardrails would be necessary to prevent collisions with culverts. This would produce numerous guardrail crashes for every culvert impact that is prevented. Another possibility would be to build culverts with sloped ends. However, the bevelled culvert only changes the trajectory of an impacting vehicle and does not absorb its kinetic energy. This can sometimes be even more dangerous when an uncontrolled vehicle is returned to a busy road or redirected to another fixed object. Instead of the slopes, energy-absorbing systems could be placed on the sides of culverts. But this solution has many drawbacks: it is highly expensive and space-consuming; modification of the EAS design would be required to allow water to flow; and also it would be necessary to prevent vehicles from crossing the EAS, as the EAS are commonly not designed to withstand the vertical loading.

The aim of this thesis is to develop a novel high-load-bearing energy-absorbing system that simultaneously fulfils the function of a culvert and an energy absorber. It has been proposed [69] that an energy-absorbing system with cellular structures might dissipate the impact energy because of deformation of the cells and have sufficient load bearing capacity in the direction perpendicular to the expected impact. The energy-absorbing system should be designed in a way that the cells are impacted laterally with their walls serving as supporting elements.

Chapter 2

Energy-absorbing system composed of fired clay blocks

Abstract

This chapter[1] lays the foundation for the development of a high-load-bearing energy-absorbing system with controlled deformation. Brittle ceramic blocks made of bricks with thin-walled cellular structures are presented and tested with impact loading. It is demonstrated that such blocks are able to absorb impact energy because of the gradual brittle fracture process which occurs in the cellular structures. Full-scale specimens were subjected to laboratory impact tests: two non-deformable flat-nosed cart tests as well as two full-scale field crash tests involving passenger vehicles with crumple zones. The experiments were designed specifically to prove that block specimens are able to gradually absorb different levels of impact energy and to examine the applicability of using such blocks in the design of cross-drainage culverts. Based on a comparison of the two collisions with test culverts, it is shown that consequences of the collision can be significantly reduced by using brittle blocks with cellular structures in culverts. In fact, the crumple zone of the passenger vehicle which collided with a brittle block culvert was not crumpled; vehicle bounce off was eliminated and gradual deceleration of the vehicle was recorded.

Highlights

- Brittle fracture process of ceramic blocks is examined.
- The gradual absorption of impact energy by fracturing cellular structure is presented.
- Response under different levels of the impact energy is examined.
- Non-deformable flat-nosed cart impact tests are performed and evaluated.
- Passenger vehicle impact tests are performed and evaluated.

[1] reproduced from Petr Hála et al. "Fracture behaviour of ceramic blocks with thin-walled cellular structures under dynamic loadings". In: Thin-Walled Structures 122 (2017), pp. 597–605. issn: 02638231. doi: 10.1016/j.tws.2017.10.050.

2.1 Introduction

The ability of a cellular structure made of brittle material to collapse progressively and gradually decelerate a vehicle's impact have, to date, only been proposed [69] and have never been verified. It is presumed that a block with cellular structures, which has high-load bearing capacity in the direction parallel to cell direction, would also be able to absorb impact energy in the direction perpendicular to cell direction because of rapid brittle fracture of the cellular structure. It is assumed that the energy absorbing process would be divided into two stages. In the first stage, a block would be systematically destroyed and debris pushed inside the block up to the absolute fill of the free space in the cells. The second stage would begin when compacted material is crushed.

This chapter presents two experiments specifically designed to support this theory and investigates blocks made of industrial ceramic bricks with thin-walled cellular structures originally designed as a load-bearing and thermal-insulating elements. It is demonstrated how these blocks can dissipate impact energy because of brittle fracture of their cells. Responses of blocks to impacts with a non-deformable flat-nosed cart and two passenger vehicles with crumple zones are analysed. Both experiments verify the ability of cells to collapse progressively. In addition, an impact test with a non-deformable flat-nosed cart demonstrates that a specimen is able to gradually absorb different levels of impact energy. Two impact tests with passenger vehicles were designed to determine the suitability of brittle blocks to be used as cushioning elements in cross-drainage culverts. The load-bearing capacities of experimental blocks are also verified.

Usually, car crash experiments or their numerical simulations are focused on the development or improvement of existing barriers and protecting sensitive structures, neglecting vehicle passenger safety. Namely, researchers have investigated the resistance of a barrier to impact loading [73]; effectiveness in reducing possible vehicle crossovers [74, 75]; protecting a perimeter around significant buildings or infrastructures and consequent reduction of blast and debris threats from vehicles bearing improvised explosive devices [76, 77]. The effect of a crash on the safety of passengers has not, to my knowledge, been investigated in the aforementioned literature. The experiments presented in this chapter were designed not only to demonstrate the ability of the target to stop the impact of a vehicle but also to determine the effect of a collision on vehicle passengers. The suitability of the tested specimens to be used as cushioning elements in cross-drainage culverts is determined and their load-bearing capacities are also verified.

2.2 Material and methods

2.2.1 Design

Ground bricks (commercially available HELUZ 50 Family) were chosen for the specimens considered in this study (Figure 2.1). These bricks are made primarily of clay mixed with saw dust and papermaking sludge as aeration agents. Ceramic bricks are manufactured structural elements, making them easily and inexpensively obtainable in large quantities and ideal for the purpose of this study. Such bricks have thermal-insulating structural elements containing hollow cells with a designated volume (58%) to ensure thermal insulation properties but still provide sufficient load-bearing capacity. These cells are hexagonal and are distributed regularly; each row is offset by the half the cell spacing. These cellular structures do not contain any walls which could brace impact. Their ability to collapse progressively was preliminary verified using a reduced-scale specimen and high speed camera recording. The reduced-scale specimen was tested using an impact

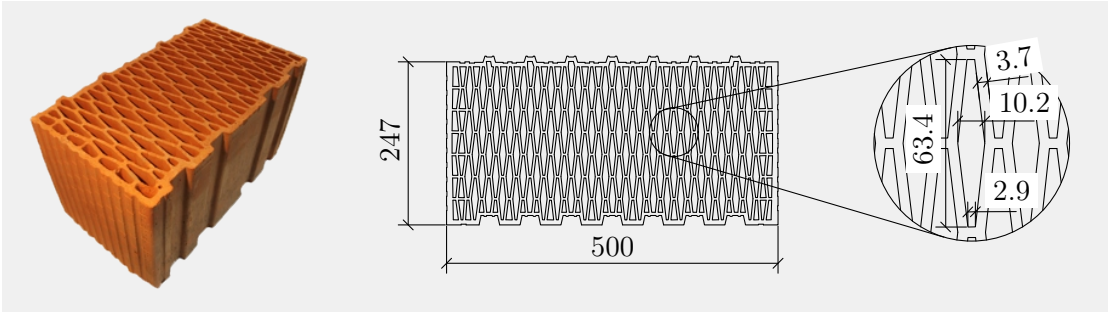

Figure 2.1: Grinded ceramic brick; its cellular structure and detailed sketch of one cell; dimensions in mm.

Table 2.1: Measured characteristics of grinded brick. Values in parentheses give the standard deviation.

	Manufacturer	Experimentally measured
Characteristic compressive strength (MPa)	8.0	-
Mean compressive strength (MPa)	-	10.1 (1.4)
Modulus of elasticity (GPa)	3.3	3.4 (0.2)
Poisson's ratio (-)	-	0.24 (0.05)

pendulum machine with a 37 kg flat-nosed impactor travelling in a circular trajectory and hitting the specimen in the bottom-return point [78]. According to footage recorded (Figure 2.2), cells collapsed systematically with brittle fracture. This led to gradual deceleration of the impactor.

According to the manufacturer, the mass of the grinded brick is 19.7 kg; and width, height, and depth 247 mm, 249 mm, and 500 mm, respectively. Thickness of the wall is 3.7 mm. The mean compressive strength, secant modulus of elasticity, and Poisson's ratio were determined experimentally using conventional procedures. Bricks were transferred to the laboratory 14 days before experimental measurements to ensure constant properties. Temperature in the laboratory was 19-19.5 ℃ and relative humidity was 45-49%. Mean compressive strength was measured for seven specimens in a hydraulic loading machine using monotonic increments of load at speed 0.36 MPa/s up to brittle failure of the brick. Tests were performed using a DSM 2500-100 testing apparatus. The apparatus consists of a stiff loading frame with loading capacity of 2500 kN. The loading frame has a hydraulic servomechanism that allows both force increment and close-loop feedback deformation loading. The secant modulus of elasticity and Poisson's ratio were determined based on results for five specimens. The modulus of elasticity and Poisson's ratio were measured using two strain gauges attached vertically to the sides of each specimen and another two strain gauges glued horizontally to the longitudinal sides of specimens at the middle of their heights. In the first step, specimens were loaded to 1/3 of expected maximal compressive strength for 60 seconds. Following this, specimens were unloaded to 0.5 MPa. This procedure was repeated three times. The secant modulus of elasticity and Poisson's ratio were calculated during the third unloading cycle. The results of the experiments are summarised in Table 2.1.

Bricks with two different modifications were considered in this study. When a brittle specimen was required, the longitudinal sides of the brick were trimmed (Figure 2.3) to eliminate tongue and groove joints. When a stiffer specimen was required, cells of brick were filled with polystyrene.

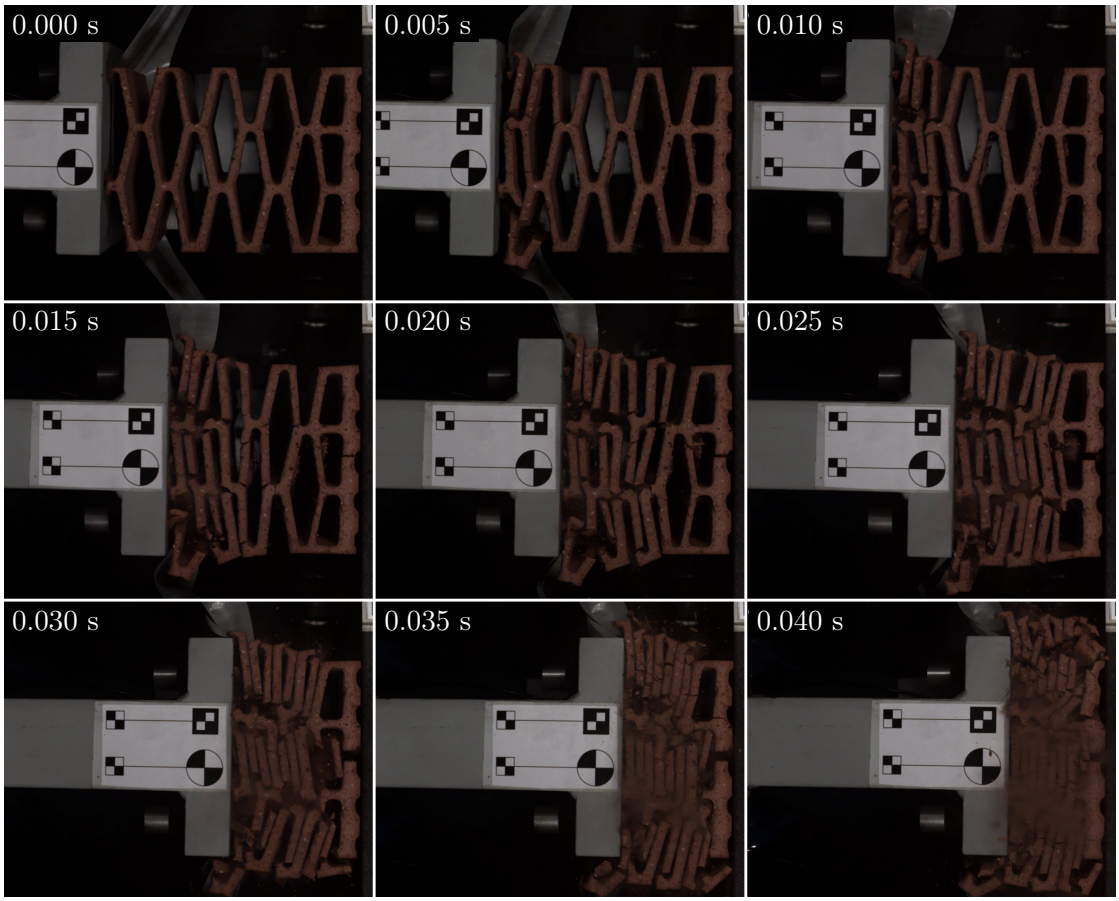

Figure 2.2: Fracture process of cellular structure under impact loading.

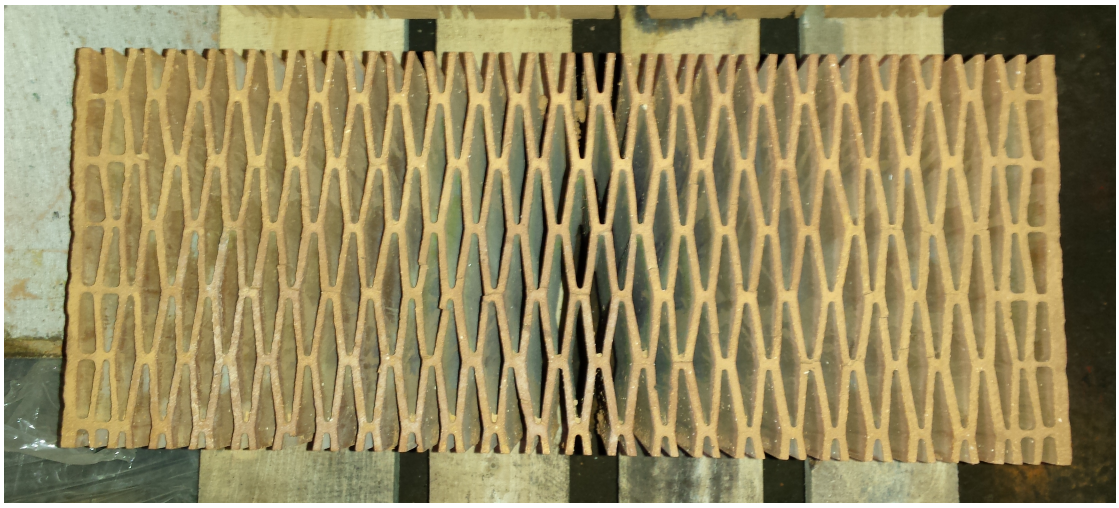

Figure 2.3: Trimmed brick.

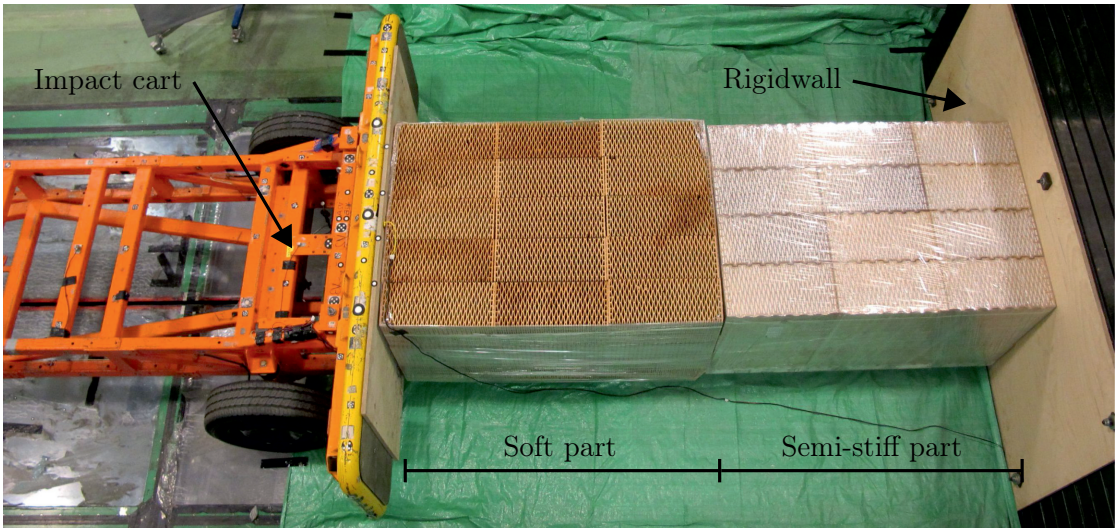

Figure 2.4: Top view of impact cart showing contact of soft and semi-stiff specimen parts.

2.2.2 Impact of a non-deformable flat-nosed cart

Two impact experiments using a 1000 kg non-deformable flat-nosed impact cart were conducted, varying only in impact energies. During one experiment, the impact velocity was 30 km/h (8.33 m/s); during the other, velocity was 50 km/h (13.89 m/s). Impact energies were 34.7 kJ and 96.5 kJ, respectively. The tested specimen had soft and semi-stiff parts. The soft part was comprised of 45 trimmed bricks, 5 wide and 3 tall/long. The semi-stiff part was wrapped in plastic foil and comprised of 36 bricks filled with polystyrene, 4 wide and 3 tall/long. Dimensions of the entire specimen were approximately 750 mm × 1000 mm × 3000 mm (height × width × length). The back face of the specimen was placed against a rigid wall (Figure 2.4). The progressive collapse of the cellular structure was recorded with a high speed camera operating at frequency 3000 fps. Deceleration of the impact cart was measured by an accelerometer attached to its nose.

2.2.3 Impact of passenger vehicle with crumple zones

In order to determine the fracture process of the cellular structures, including their ability to gradually absorb kinetic energy of vehicular impact, two vehicular crash tests were conducted. During these experiments, an ordinary passenger vehicle (commercially available Skoda Fabia, 3rd generation) frontally impacted a non-deformable specimen made of reinforced concrete and a deformable specimen of trimmed bricks at approximately 50 km/h.

Both impacted specimens were built into cross-drainage culverts embedded in the ground. A hole for specimens was excavated together with a ditch which directed the impacting car to each specimen after the car left its guide rail. The non-deformable specimen was transported to the test site directly from the factory and inserted in the hole with a crane. The rest of the hole was filled with soil then rammed down with a tamping machine. The non-deformable specimen was cast from concrete grade C20/25 and consisted of a bottom plate surrounded by four walls (Figure 2.5). The outer dimensions of the culvert were 3.25 m (length), 2.55 m (width), and 1 m (height). Wall and plate thickness was 0.25 m. The impacted front wall of the specimen was reinforced with reinforcing mesh 12 mm in diameter with 100 mm spacing. The rest of the specimen contained a mesh 8 mm in diameter with the same spacing. Reinforced meshes were embedded in both surfaces with

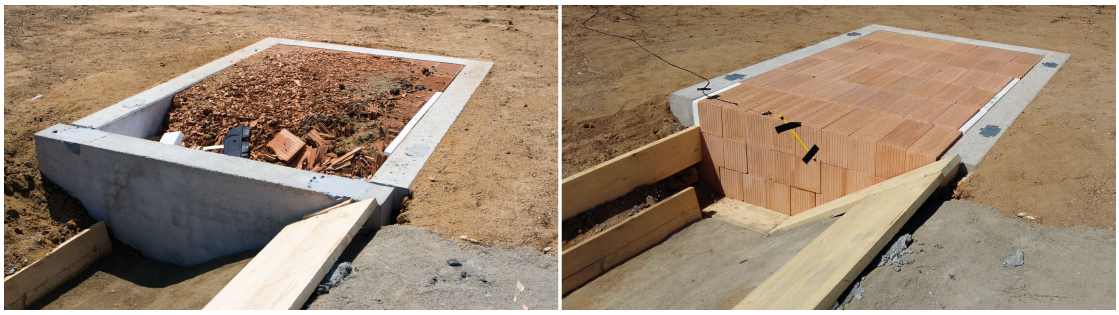

Figure 2.5: Non-deformable reinforced concrete specimen (left) and deformable specimen of trimmed bricks (right).

a 20 mm concrete cover. In contrast to the non-deformable specimen, the deformable specimen did not have a front wall. It was filled with 162 bricks with trimmed longitudinal sides to eliminate tongue and groove joints. Trimmed bricks were placed inside in 3 rows, 9 columns, and 6 layers in the depth and impacted perpendicular to their shorter sides.

The vehicles were 3.99 m long, 1.73 m wide, and 1.47 m tall. The weight of each vehicle, including driver, was 1.1 t. Each test vehicle was set to neutral gear and accelerated to the required velocity with a reverse towing system consisting of a tow vehicle, tow cable, re-directional pulley anchored to the ground, and quick-release mechanism that disconnected the tow cable and steering guidance. Guidance for test vehicles was provided by a rigid rail prior to release, after which each vehicle was allowed to proceed according to its own momentum, guided by the ditch before impact with a test specimen.

Two crash test dummies were placed in each vehicle. Adult dummy type H III was placed in the driver's seat, and child dummy type P6 was placed in a child restraint system in the back seat behind the driver. Dummies' seat belts were fastened and airbags turned off. A triaxial accelerometer was placed on the body of each vehicle near the airbag control unit and the data obtained were used to determine the level of energy absorbed during the experiments. The field test was also recorded with high-speed cameras to observe progressive deformation of the deformable specimen, the motion of vehicles, and the dummies themselves immediately before and after impact. Specific points on the impacted vehicles were tracked using fiducials which enabled tracking of selected points during impact. High-speed video and still images from cameras were used to determine the change in the movement of the vehicle and its velocity at various times.

2.3 Results and discussion

2.3.1 Impact of non-deformable flat-nosed cart

The progressive collapse of the specimen while subjected to 34.7 kJ and 96.5 kJ impact energies is depicted for 60 ms intervals in Figure 2.6 and Figure 2.7, respectively. Immediately after each impact, gradual brittle fracture for the soft part and accumulation of resulting debris were recorded. Deformation of the semi-stiff part was not observed. Progressive collapse lasted 140 ms for the 34.7 kJ impact, and 80 ms for the 96.5 kJ impact. After collapse, the cellular structure of the soft part disintegrated completely and the remaining kinetic energy of the cart was absorbed by material accumulation and deformation of the semi-stiff part. The deformation process for the semi-stiff part can be divided into four modes: plastic wrap stretch, brittle fracture of cells, compression of polystyrene filling, and accumulation of material. These modes of deformation took

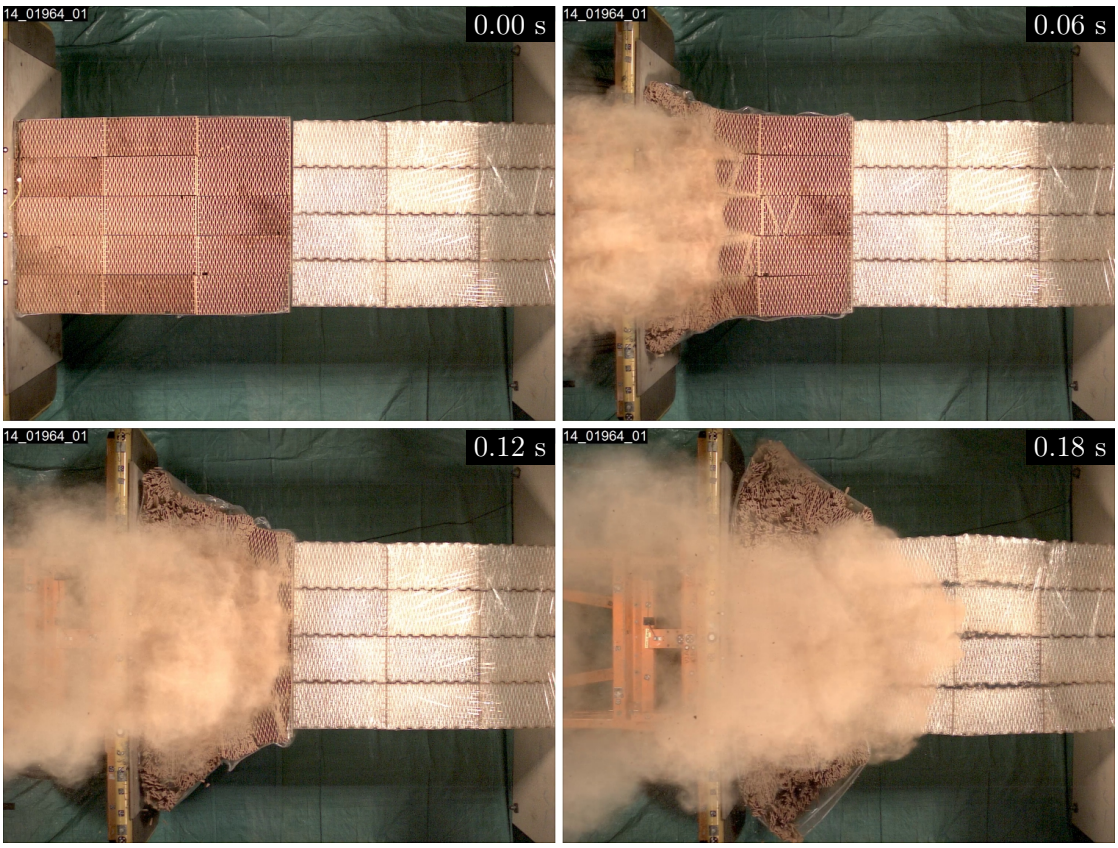

Figure 2.6: Time evolution of progressive collapse for 34.7 kJ impact.

place at the same time and cannot be clearly distinguished in photographs. Impact energy was completely absorbed by the specimen after 216 ms for the 34.7 kJ impact and at approximately 300 ms for the 96.5 kJ impact, at which point deceleration was no longer recorded and 99.9% (96.4 kJ) of impact energy had already been absorbed. During both experiments, the soft part of the specimen disintegrated completely, but the semi-stiff part collapsed only for the 96.5 kJ impact (Figure 2.8). It can be concluded that part of the deformation process of the semi-stiff part was elastic because the semi-stiff part tended to return to its initial form (Figure 2.9) and the slow cart reversal movement was recorded at the end of the 34.7 kJ impact.

Deceleration of the impact cart was measured using an accelerometer attached to its nose. Time (t) evolution for non-deformable flat-nosed cart velocity (v) and motion (u) after crashing into the specimen was determined to be the first (Figure 2.10) and the second integral (Figure 2.11) of measured deceleration (a).

$$v = \int a \mathrm{d}t \tag{2.1}$$

$$u = \int \int a \mathrm{d}t^2 \tag{2.2}$$

During both experiments, the velocity of the cart was reduced systematically and the cart decelerated smoothly. During the 34.7 kJ impact, the cart decelerated to zero at approximately one third (0.9 m) of the length of the specimen (3 m) and did not reach the end of the soft part (1.5 m). During the 96.5 kJ impact, the cart travelled approximately

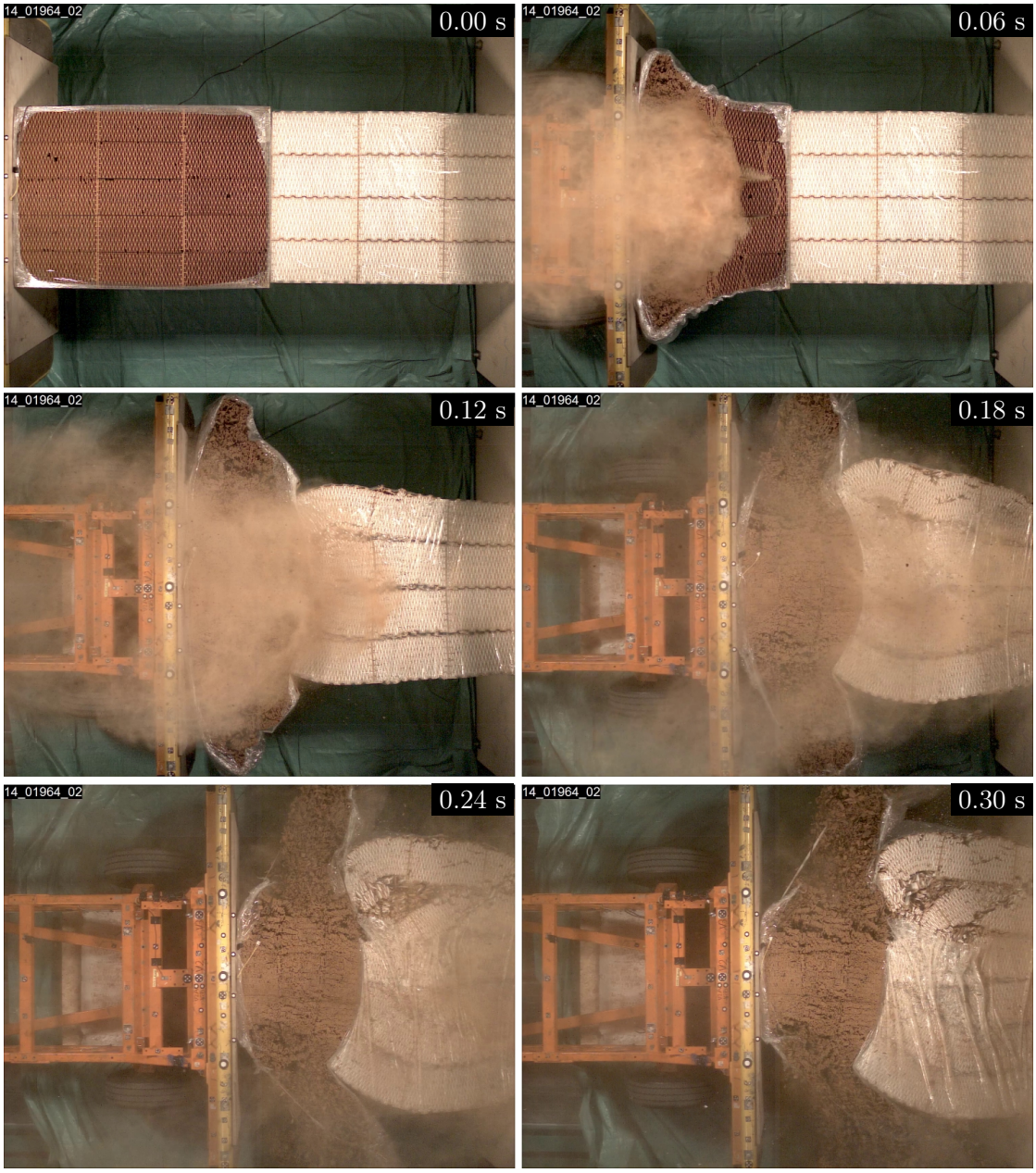

Figure 2.7: Time evolution of progressive collapse for 96.5 kJ impact.

Figure 2.8: Soft and semi-stiff part of specimen after 34.7 kJ impact (left) and 96.5 kJ impacts (right).

Figure 2.9: Semi-stiff part of specimen after 34.7 kJ impact.

two times as long as during the 34.7 kJ impact and compressed the semi-stiff part by one eighth of its original length. It is expected that even higher impact energies could be absorbed, because more energy could be dissipated by accumulated materials.

Measured deceleration (a) was multiplied with the mass (m_0) of the cart and integrated from its travelled distance (u) to obtain energy absorption (EA) of the specimen (Figure 2.12).

$$EA = \int m_0 a \mathrm{d}u \tag{2.3}$$

The resulting energy absorption is presented with regard to normalized distance as proposed by Chen et al [42]. Normalized distance is the distance over the total length of the specimen (3 m). Impact energy was absorbed gradually and there is no sudden increase in energy absorption at the end of the impact process. This means the material was not crushed and the kinetic energy was absorbed only because of brittle fracture of the cells, accumulation of materials, and deformation of the semi-stiff part.

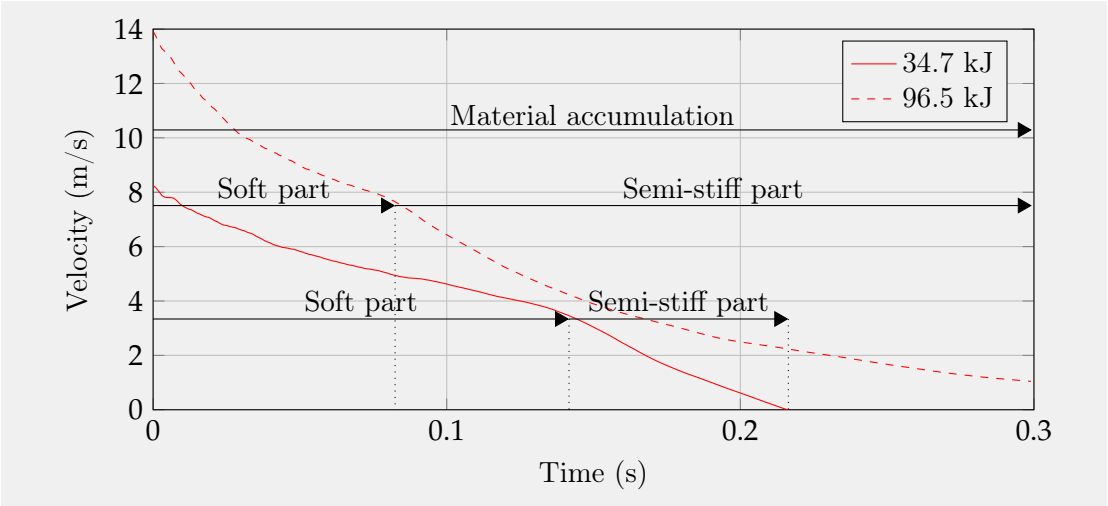

Figure 2.10: Time evolution of non-deformable flat-nosed cart velocity after crashing into specimen at various impact energies.

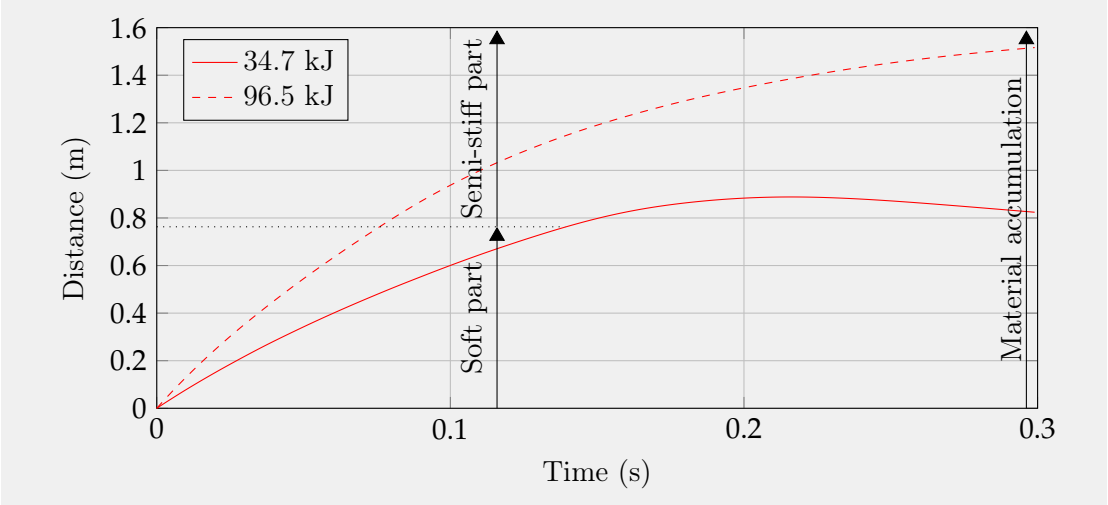

Figure 2.11: Time evolution of travelled distance of non-deformable flat-nosed cart after crashing into specimen at various impact energies.

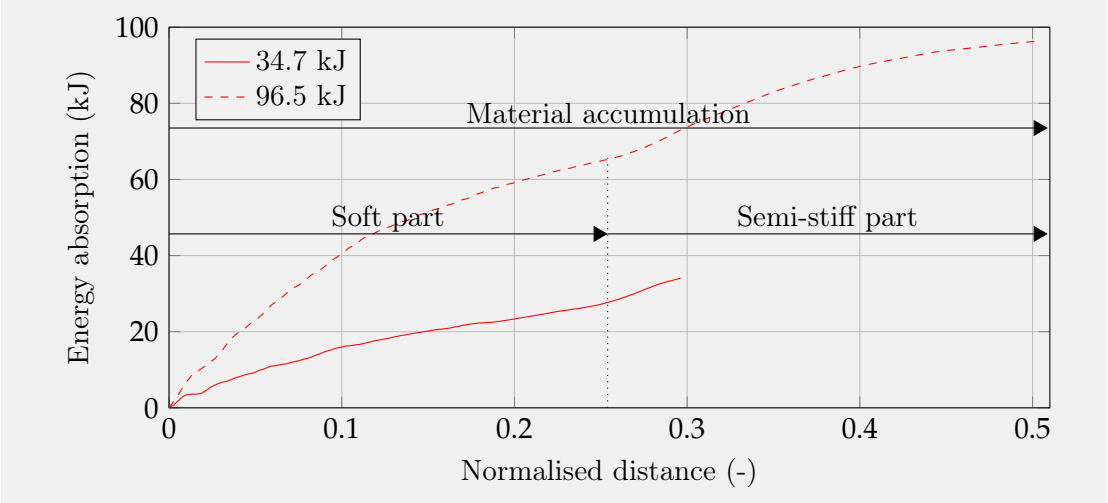

Figure 2.12: Energy absorption of specimen impacted by non-deformable flat-nosed cart at different impact energies.

2.3.2 Impact of passenger vehicle with crumple zones

Post-test investigation showed only minor cracks were formed on the front wall of the reinforced concrete specimen. This supports the theory that the specimen absorbs insignificant amounts of energy from vehicular impact and justifies its classification as a non-deformable object. It can also be concluded that the correct amount of bricks was chosen to form the interior of the deformable specimen because their collapse progressed systematically throughout the entire specimen. This led to gradual deceleration of the vehicle.

Real impact velocities obtained during the tests as recorded by high-speed camera were 47 km/h (13.06 m/s) for the non-deformable specimen and 45 km/h (12.38 m/s) for the deformable specimen. The resulting deviation from expected velocity might have been caused by natural deceleration of the vehicle as it proceeded under its own momentum following separation from the pulling wire, and perhaps also due to the tachometer of the towing vehicle that pulled the impacting vehicle through the wire and pulley system to reach required impact velocity. As is generally known, tachometers installed in passenger vehicles show slightly higher velocity than actual speed for safety reasons.

The graphs showing movement (Figure 2.13) and velocity (Figure 2.14) time histories for vehicular impact were based on the data obtained from the high-speed camera recordings. The recording tracked the fiducial point at the bottom of the driver's side front pillar. By examining these graphs, it can be concluded that—in contrast to the collision with the non-deformable specimen—impact with the deformable specimen allowed intact parts of the vehicle to decelerate to zero for more than a three times as large area, for a more than four times as long time. For the collision with the non-deformable specimen, the vehicle was bounced back 0.071 s after first contact, when the energy absorption capacity of vehicle construction was reached. Time evolution of energy absorption (Figure 2.15) during the collisions was determined with data measured by an accelerometer located near the airbag control. Measured deceleration was multiplied with the mass of the vehicle and integrated from its travelled distance. During collision with the non-deformable specimen, impact energy was absorbed almost entirely by the crumple zones of the vehicle and the energy absorption capacity of the crumple zones was quickly reached. In contrast, for the deformable specimen, vehicular crumple zones were not even crumpled during collision; impact energy was absorbed by gradual brittle fracture of the ceramic bricks and the vehicle decelerated slowly and smoothly.

This controlled deceleration also had a positive influence on the driver dummy. The dummy hit the steering wheel during collision with the non-deformable specimen but did not even touch it during collision with the deformable specimen. As a downside, however, upward vehicular movement was observed for the deformable specimen. During the collision, the vehicle was pushed up by brittle block which accumulated beneath the tires. Despite this, the vehicle decelerated because of the brittle fracture of cellular structures and did not leave the ditch. Attention should be paid to this phenomenon for future experiments conducted at higher impact velocities. Time evolution for vehicular collision with non-deformable and deformable specimens is depicted at 60 ms intervals in Figure 2.16 and Figure 2.17.

Compared to the metallic thin-walled structures [31, 32, 40, 42, 44–48, 50, 79], the presented ceramic blocks exhibit higher dust production during impact and occupy a larger area. However, intended applications for these blocks are exterior cross drainage culverts where higher dust or uneasy clean-up are not the primary concerns. In addition,

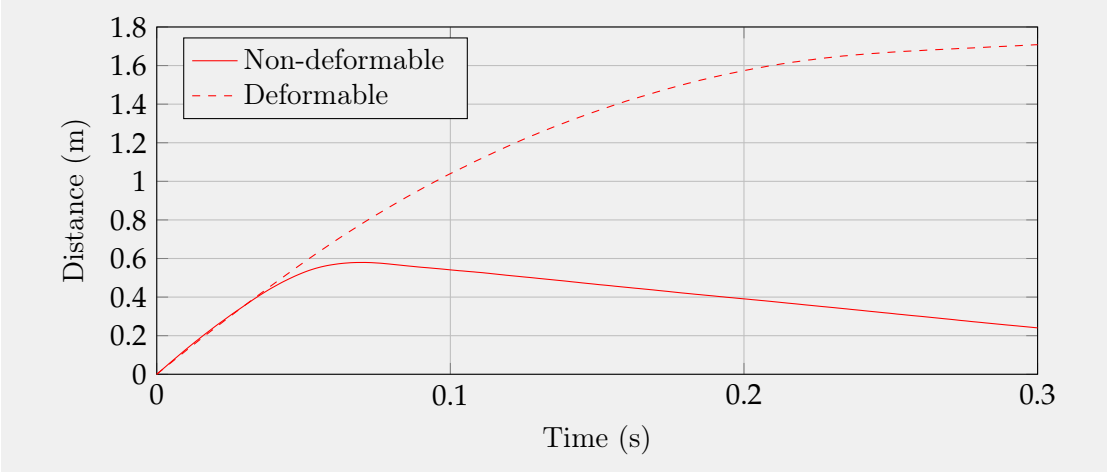

Figure 2.13: Time evolution of distance travelled by vehicle after crashing into a non-deformable reinforced concrete specimen and a deformable specimen of trimmed bricks with cellular structures.

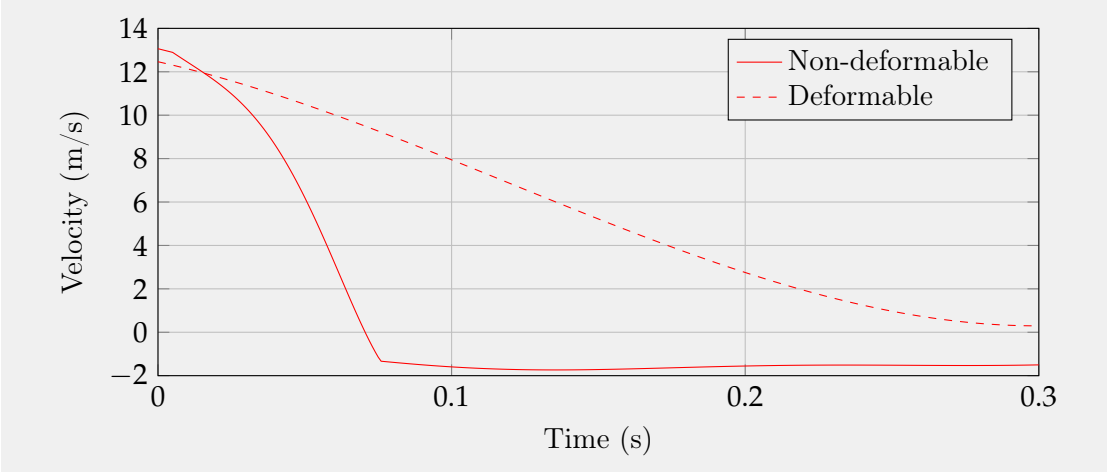

Figure 2.14: Time evolution of vehicle velocity in the direction of impact after crashing into a non-deformable reinforced concrete specimen and a deformable specimen made of trimmed bricks with cellular structures.

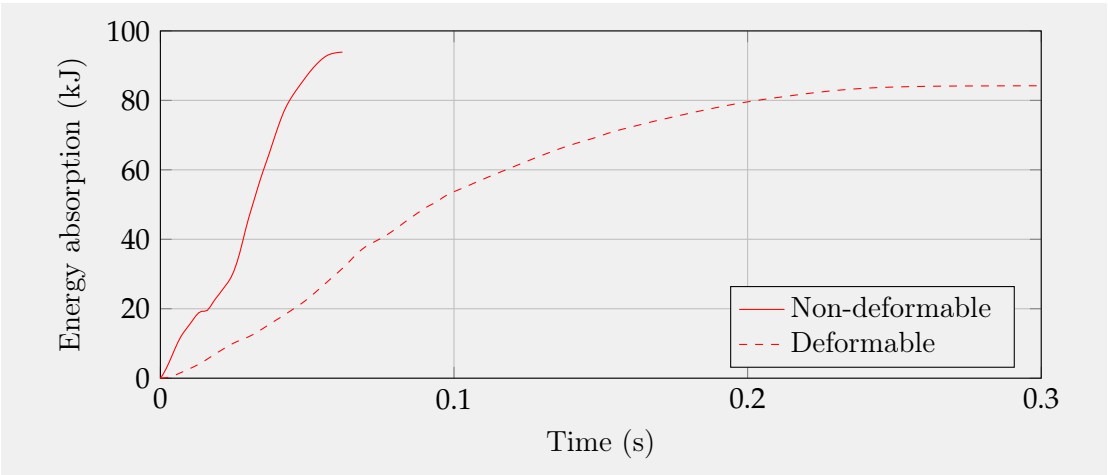

Figure 2.15: Time evolution of energy absorption in the direction of impact after crashing into a non-deformable reinforced concrete specimen and deformable specimen made of trimmed bricks with cellular structures.

Figure 2.16: Collision of Skoda Fabia vehicle with non-deformable reinforced concrete specimen.

Figure 2.17: Collision of Skoda Fabia vehicle with deformable specimen of trimmed bricks with cellular structures.

such exterior application in cross drainage culverts requires certain area to be occupied and such block were ideal for the interest of this study.

2.4 Conclusions

In this chapter, responses of ceramic blocks made with bricks with thin-walled cellular structures to impacts with a non-deformable flat-nosed cart and two passenger vehicles with crumple zones were observed. The following inferences can be drawn from the study:

1. Load-bearing ceramic blocks tested here were able to absorb impact energy because of the gradual brittle fracture process in their cellular structures.
2. It is possible to design a specimen composed of brittle bricks with cellular structures able to gradually absorb different levels of impact energy by combining soft (trimmed bricks) and semi-stiff (bricks filled with polystyrene) elements.
3. Passenger vehicle crumple zones were not crumpled during the collision with brittle blocks.
4. The damaging consequences of passenger vehicle collisions with cross drainage culverts could be significantly reduced by building culverts using blocks that have brittle cellular structures.
5. Future studies should investigate the upward movement of a passenger vehicle when it collides with brittle blocks. In this study, the authors found this was due to the accumulation of debris beneath tires.
6. Development of a new energy absorption system consisting of blocks with brittle cellular structures might lead to an increase in transportation safety; however, the blocks tested here have a limited lifetime in harsh environmental conditions and may therefore fail during the service life of a structure. Future studies should be devoted to finding applicable materials suitable for use in harsh environments while still keying an eye towards reasonable production costs and ability to be mass produced.

Chapter 3

Comparative study on the crashworthiness of brittle blocks

Abstract

Even though the number of deadly traffic incidents is decreasing, the proportion of motor vehicle crash deaths involving a collision with fixed objects is not. To address this issue, a novel load-bearing energy-absorbing system comprised of brittle blocks with thin-walled cellular structures is presented here[1], laying the foundation for the assessment of the system's crashworthiness. Six brittle hexagonal cellular structures were subjected to quasi-static and impact tests. The crushing process, force-displacement curves, and a wide range of indicators of crashworthiness were examined. Samples with different levels of crashworthiness were identified and several observations that could guide future crashworthiness design are given. The findings show that relatively small changes in the design can lead to production of blocks with distinguishable levels of crashworthiness.

Highlights

- The foundation for the assessment of the crashworthiness of brittle blocks is laid.
- Quasi-static and impact testing of brittle cellular structures is presented.
- The gradual brittle fracture process occurring in a cellular structure is examined.
- Several observations that could guide future crashworthiness design are given.
- The manufactured blocks with different levels of crashworthiness are identified.

[1] reproduced from Petr Hála et al. "Comparative study on the crashworthiness of brittle blocks with thin-walled cellular structures". In: Thin-Walled Structures 148. December 2019 (2020). issn: 02638231. doi: 10.1016/j.tws.2019.106578.

3.1 Introduction

The proposed energy absorbing system is comprised of blocks with thin-walled cellular structures and is able to absorb impact energy because of the gradual brittle fracture which occurred in the cellular structure of the blocks (Figure 3.1). The preceding chapter [1] examined the applicability of using such blocks in the design of cross-drainage culverts and showed that it is possible to design a specimen composed of brittle blocks with cellular structures able to gradually absorb different levels of impact energy by combining elements of different stiffness. It was also demonstrated that the consequences of a collision can be significantly reduced by using brittle blocks with cellular structures in culverts. In fact, the crumple zone of the passenger vehicle which collided with a brittle block culvert was not crumpled; vehicle bounce off was eliminated and gradual deceleration of the vehicle was recorded.

In this chapter, the quasi-static and impact testing of such brittle cellular structures is presented together with an assessment of their crashworthiness. Blocks with different levels of crashworthiness are identified and several observations that could guide crashworthiness design are given. This is essential for a deeper understanding of the energy absorbing process of the novel EAS. It will be beneficial in setting a direction for future studies devoted to the examination of the combination of samples with different levels of crashworthiness and for the design of new brittle cellular structures.

Figure 3.1: A passenger vehicle after impacting the novel energy absorbing system comprised of brittle blocks with thin-walled cellular structures.

3.2 Methodology

3.2.1 Assessment methodology

To determine the crashworthiness of the EAS and to compare different EAS designs, ten indicators of crashworthiness and two multiple-criteria decision-making methods are used.

3.2.1.1 Indicators of crashworthiness

Energy absorption [15, 16, 18, 19, 21, 22, 24, 25, 29, 32, 42, 43, 50, 65, 67, 80, 81] is determined by integrating the area below the force-displacement curve:

$$EA = \int_0^{u_{\text{eff}}} F(u)\mathrm{d}u \tag{3.1}$$

where F and u are instantaneous crushing force and crushing displacement, respectively, and where u_{eff} is the effective crush stroke.

The effective crush stroke u_{eff} is a very important parameter that affects all indicators of crashworthiness. As such, it should be clearly defined. Some authors [51] substitute it with the maximum crush stroke $u_{\max}$, some [31, 32, 42, 43, 50] use only 70% of $u_{\max}$, and some [16] read the value when the crushing force reaches a local minimum after which the load increases monotonously. Another definition ([82], which is also the definition used in this work) says that u_{eff} is the corresponding crush stroke when energy absorption efficiency renders its global maximum:

$$EAE(u_{\text{eff}}) = \max_u EAE \tag{3.2}$$

It was reported in [43] that EAE is a useful indicator to demonstrate the ability of a sample to absorb a certain amount of energy and also to control the force response within the desired range. EAE is defined as a ratio of EA and PCF:

$$EAE = \frac{EA}{PCF} \tag{3.3}$$

where PCF is the peak crush force [15–19, 21–25, 43, 65, 80, 81]. PCF is considered to be a safety indicator and should be minimised [16, 19] to avoid high deceleration felt by the occupants of a vehicle and to preclude severe injury or death. It is defined as the maximum force recorded up to u_{eff}:

$$PCF = \max(\{F(u) : 0 \leq u \leq u_{eff}\}) \tag{3.4}$$

Together with PCF, the specific energy absorption (SEA) is one of the most examined parameters in the literature and is considered in many crashworthiness optimisations of EAS [26]. Many authors [15, 16, 18, 19, 21, 22, 25, 29, 31, 32, 34, 42, 43, 50, 51, 67, 81, 83] use SEA to compare the energy absorption ability of different EAS. SEA can be determined by dividing EA by the mass (m) of EAS:

$$SEA = \frac{EA}{m} \tag{3.5}$$

It was reported in [19] that SEA is an important parameter in designing a system where weight is a limiting factor.

Analogically, the volume specific energy absorption [43] and the energy absorbed per unit crush [50, 51] can be determined by dividing EA by the volume of EAS (V) and u_{eff} respectively:

$$VSEA = \frac{EA}{V} \tag{3.6}$$

$$EAc = \frac{EA}{u_{\text{eff}}} \tag{3.7}$$

It was reported in [50] that EAc is a very important indicator in applications that have a limited crush zone.

Equation (3.7) is more commonly [17, 19, 22–25, 67, 80, 81, 84–86] used to determine the mean crush force:

$$MCF = \frac{EA}{u_{eff}} \tag{3.8}$$

MCF is the average force from initial deformation of an EAS until u_{eff}. The optimal level of MCF is relative regarding the intended application of an EAS. Some researchers (e.g. [86]) maintain high MCF to increase the energy absorbing capacity of EAS; others [84, 85] suggest low levels to reduce the risk of injuries.

Dividing MCF by PCF, the crush force efficiency factor [15, 18, 19, 22–25, 65, 67, 80, 81] can be obtained:

$$CFE = \frac{MCF}{PCF} \tag{3.9}$$

Most EAS are purposefully designed to have CFE as close to 1 as possible to maintain a low difference between MCF and PCF and to provide a fairly stable reaction force through the entire crushing process [16]. CFE is sometimes also denoted as structural efficiency [22] or shape factor [24, 25].

Crush efficiency [32], sometimes referred to as stroke efficiency [50, 84], describes the amount of material that can be used during a collapse:

$$CE = \frac{u_{eff}}{L} \tag{3.10}$$

where L is the total length of an EAS. High levels of CE are suggested [16, 67] to allow for complete utilisation of the EAS.

CE can be multiplied by CFE to determine energy efficiency [32, 50], sometimes also referred to as total efficiency [67]:

$$EE = CE \times CFE = \frac{EA}{PCF \times L} = \frac{EAE}{L} \tag{3.11}$$

It is recommended in [32, 50] to maximize EE in order to achieve a stable reaction force throughout the long deformation process.

CE can be also multiplied by SEA to determine work effectiveness [32, 50]:

$$WE = CE \times SEA \tag{3.12}$$

WE was reported in [32, 50] to be a very useful indicator of crashworthiness in structures that are restricted in terms of both weight and space.

3.2.1.2 Multiple-Criteria Decision Method

When evaluating the overall crushing performance of an EAS, several design criteria should be evaluated. To choose the best option when a large variety of factors will be considered, multiple-criteria decision-making methods can be adopted [87]. Examples of these methods include AHP [88–102], DEA [103–105], ANP [106, 107], GST [108, 109], ELECTRE [110–113], TOPSIS [18, 114–116], and COPRAS [65, 80, 81, 117–119]. The TOPSIS and COPRAS methods have been employed by other researchers to compare the crashworthiness of different thin-walled energy absorbing systems and will be therefore considered in this study.

Nikkhah et al. [18] employed the TOPSIS method to compare the overall crushing performances of circular, rectangular, square, hexagonal, convex, and elliptical windowed and simple tubes under dynamic axial loading. Qiu et al. [80] used the COPRAS method to select the best possible sectional configuration for multi-cell hexagonal columns under multiple loading angles. Tarlochan et al. [81] used the COPRAS method to select the thin-walled structure with the best performance under direct and oblique loads among tubes with circular, rectangular, square, hexagonal, octoginal, and elliptical cross-sections. Fang et al. [65] applied the COPRAS method to select the ideal number of cells in multi-cell tubes subjected to axial and oblique impact loads. In the aforementioned studies, EA [18, 65, 80, 81], PCF [18, 65, 80], and CFE [65, 80, 81] were taken as design criteria.

Both methods compare different options through the evaluation of multiple criteria and rank the options based on their scores. Although the principles and procedures of assessment are similar in both methods, each of them employs different equations. The input of both methods is a so-called evaluation matrix X, where the design criterion of a single EAS are arranged side-by-side in one row (i) and values of a single design criterion for each type of EAS are ordered in column (j). Each entry x_{ij} of matrix X can be normalised using the following equation:

$$\text{COPRAS:} \qquad r_{ij} = \frac{x_{ij}}{\sum_{k=1}^{m} x_{kj}} \tag{3.13}$$

$$\text{TOPSIS:} \qquad r_{ij} = \frac{x_{ij}}{\sqrt{\sum_{k=1}^{m} x_{kj}^2}} \tag{3.14}$$

where r_{ij} is an entry of normalised evaluation matrix R and m is a number of compared variants. Considered design criteria can be divided into beneficial and non-beneficial. As the next step of the COPRAS method, the beneficial r_{ij}^{+} and the non-beneficial r_{ij}^{-} design criteria for each variant i are summarised. In the TOPIS method, an ideal alternative A_j^{+} and a negative ideal alternative A_j^{-} of each design criteria are determined and the sums of distances from these alternatives are evaluated for each variant i:

$$\text{COPRAS:} \qquad D_i^{+/-} = \sum_{j=1}^{n} r_{ij}^{+/-} \tag{3.15}$$

$$\text{TOPSIS:} \qquad D_i^{+/-} = \sqrt{\sum_{j=1}^{n} \left(r_{ij} - A_j^{+/-} \right)^2} \tag{3.16}$$

where n is the number of design criteria. The obtained sums can be used to determine the relative significance S:

$$\text{COPRAS:} \qquad S_i = D_i^+ + \frac{D_{\min}^- \sum_{i=1}^{m} D_i^-}{D_i^- \sum_{i=1}^{m} \frac{D_{\min}^-}{D_i^-}} \tag{3.17}$$

$$\text{TOPSIS:} \qquad S_i = \frac{D_i^-}{D_i^- + D_i^+} \tag{3.18}$$

where $D_{\min}^-$ is the minimum value of summarised non-beneficial design criteria.

As the last step, quantitative utility U_i can be determined for both methods using a simple formula:

$$U_i = \frac{S_i}{S_{\max}} \times 100\% \tag{3.19}$$

where $S_{\max}$ is the maximum value of the relative significance among all alternatives.

Both methods enable a certain weight to be assigned to each design criteria by modifying the normalised evaluation matrix R. In this study, the selected design criteria are considered equal and therefore the process of the weightage determination has not been presented. For a description of this procedure, the reader is referred to [65, 80, 81].

3.2.2 Experimental methodology

From the definitions of the indicators of crashworthiness, it is apparent that the desired output of experiments is a force-displacement curve. EA can be derived as the area under this curve; PCF can be expressed as its maximum. Knowing these two indicators as well as sample parameters such as mass, volume, and length, the rest of the indicators of crashworthiness can be easily derived. In this work, the response of brittle blocks with thin-walled cellular structures to quasi-static and impact loading was investigated. Both experiments were specifically designed to record the data needed to plot the force-displacement curve.

3.2.2.1 Specimens

The specimens investigated were fired clay blocks with thin-walled cellular structures; all were made primarily of clay mixed with sawdust and papermaking sludge as aeration agents. As in the previous chapter [1], commercially available blocks manufactured by HELUZ [120] were used. The company processes blocks in two different manufacturing plants and the same origin of all samples was not guaranteed. Occasionally, pre-cracks were present in the internal structures, likely due to the brick burning. To overcome these imperfections, the recorded data were carefully evaluated and experiments were repeated until acceptable standard deviations were achieved.

In total six different blocks were tested. Specimens +40, +44, F30, F44, F50, and STI44 (Figure 3.2) were obtained by trimming the commercially available blocks (HELUZ Plus 40, HELUZ Plus 44, HELUZ Family 30, HELUZ Family 44, HELUZ Family 50, and HELUZ STI 44). The blocks have thermal-insulating structural elements containing hollow cells to ensure thermal insulation properties but still provide sufficient load-bearing capacity. These cells are hexagonal with very short parallel sides, which makes them almost diamond-shaped. They are distributed regularly; each row is offset by half the cell

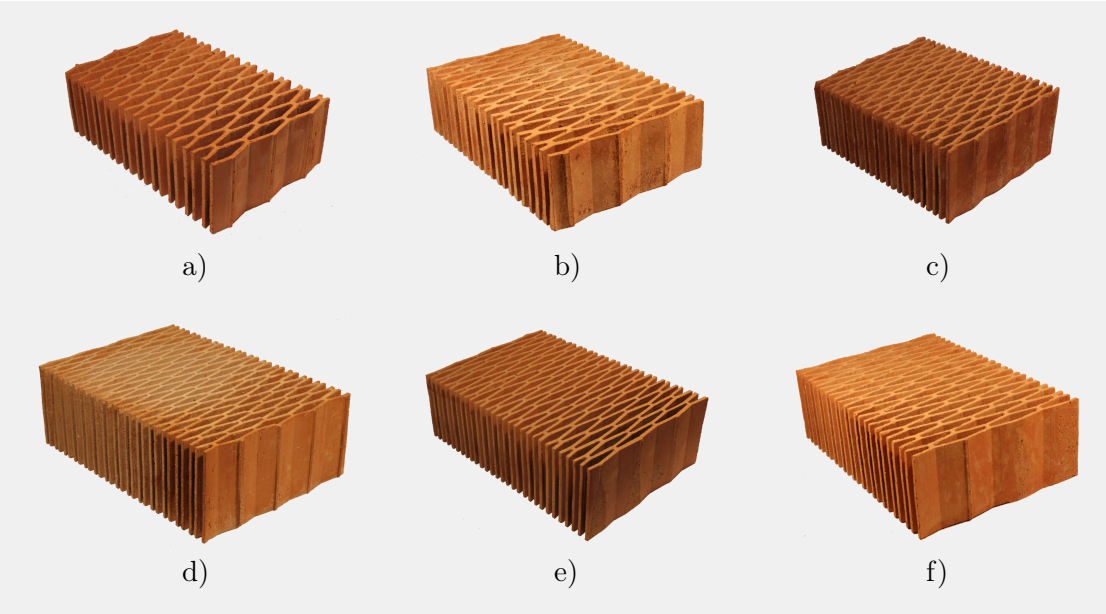

Figure 3.2: Tested ceramic specimens cut out of fired clay blocks: a) +40; b) +44; c) F30; d) F44; e) F50; f) STI44.

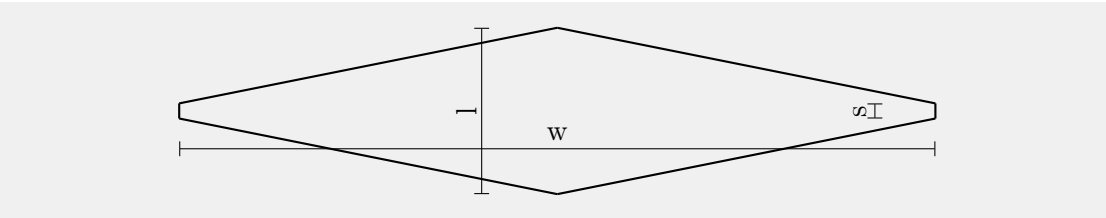

Figure 3.3: Sketch of the hexagonal cell with dimension lines.

spacing. The transverse sides were trimmed to obtain regular cellular structure; longitudinal sides were trimmed to eliminate tongue and groove joints. After trimming, none of the examined cellular structures contained any walls which could brace during loading. The shape of a cell is depicted in Figure 3.3. The internal structure of the blocks was slightly irregular by design. Therefore, the cells were carefully measured and the averaged dimensions are listed in Table 3.1 together with the standard deviations. Thickness and width of all samples were approximately 100 mm and 210 mm, respectively.

3.2.2.2 Load testing

3.2.2.2.1 Quasi-static loading

The specimens were tested in a hydro-static loading machine equipped with two parallel steel plates both represented by a block with a 400 mm base side length. One of the plates was stationary and the other was movable. Each specimen was placed in between the plates in the centre of the rectangular base (Figure 3.5a) and was subjected to monotonic increments of compression (speed: 10 mm/min.). This loading rate was selected to keep the duration of experiments acceptable and to concurrently maintain conditions similar to the quasi-static tests performed by other researchers [28, 31–34, 36, 50, 121]. Force produced by the loading machine and the displacement of the machine cross-head was monitored.

Table 3.1: Weight and dimensions of specimens tested. Values in parentheses give the standard deviation.

Type	Block			Cell			Wall
	Mass	Volume	Length	Length	Width	Short side	Thickness
	m (kg)	V (dm^3)	L (mm)	l (mm)	w (mm)	s (mm)	t (mm)
+40	3.656	6.296	310.7	15.3	59.8	3.6	5.8
	(0.272)	(0.079)	(2.8)	(0.9)	(0.8)	(0.6)	(0.4)
+44	4.134	6.338	310.6	13.3	59.1	2.3	6.1
	(0.329)	(0.036)	(1.4)	(0.7)	(1.3)	(0.5)	(0.4)
F30	3.662	5.597	260.8	10.4	46.9	2.2	4.2
	(0.216)	(0.049)	(1.6)	(0.6)	(0.7)	(0.4)	(0.3)
F44	4.228	6.548	308.7	9.5	47.7	2.4	4.1
	(0.229)	(0.062)	(1.1)	(0.4)	(0.9)	(0.4)	(0.2)
F50	3.958	6.310	306.4	10.2	63.4	2.9	3.7
	(0.209)	(0.104)	(1.3)	(1.0)	(0.9)	(0.7)	(0.3)
STI44	3.225	6.361	310.3	12.4	63.0	4.0	4.0
	(0.057)	(0.056)	(1.4)	(0.7)	(0.8)	(0.7)	(0.3)

3.2.2.2.2 Impact loading

The impact test used here was a modified version of the horizontal impact device [78, 122]. Unlike many other drop towers and impact machines with a vertical arrangement [123], where a falling weight is driven by gravity even after all of its impact energy has been absorbed by a sample, the impact device used utilises a horizontal impact direction with a stationary specimen. The impactor follows a circular trajectory using wire rope slings that guide the impactor towards the specimen. The energy of an impact can be changed by placing the hoist of the impactor in different positions or by replacing the impactor with a different weight. Even though this machine has been constructed specially for dynamic testing of prismatic concrete specimens, with slight modifications it was easily transformed into the EAS testing setup. Several impact machines based on the pendulum principle already exist. For example, Al-Oraimi and Seibi [124] used a modified Charpy impact test to study the behaviour of plain and reinforced concrete beams under impact stress; Yu at al. [125] constructed a Modified Pendulum Impact Device with a specimen hung freely on the frame to examine the impact resistance of ultra-high performance fibre reinforced concrete and to compare the results with those obtained from the Charpy Impact Device with fixed smaller specimen.

The schematic diagram of the machine is shown in Figure 3.4. To avoid friction at the vertical support, the specimen was placed on two small diameter steel tubes suspended from the pendulum structure (Figure 3.5b). The length of the suspended wire rope slings was adapted to locate the specimen at the bottom return point of the impactor trajectory. The weight of the impactor was 50 kg and the impact velocity was 2 m/s, which set impact energy at 100 J. The impactor had a steel flat rectangular nose with dimensions 400 mm × 120 mm × 30 mm (width × height × thickness).

The deceleration of the impactor was recorded by two accelerometers attached to the right and the left sides of the impactor. The recording frequency of both accelerometers was 500 kHz and their range was 5,000g. Some of the experiments were also recorded by accelerometers with a 500g range. However, using the accelerometer with a lower range did not influence the data recorded. Data obtained for accelerometers attached

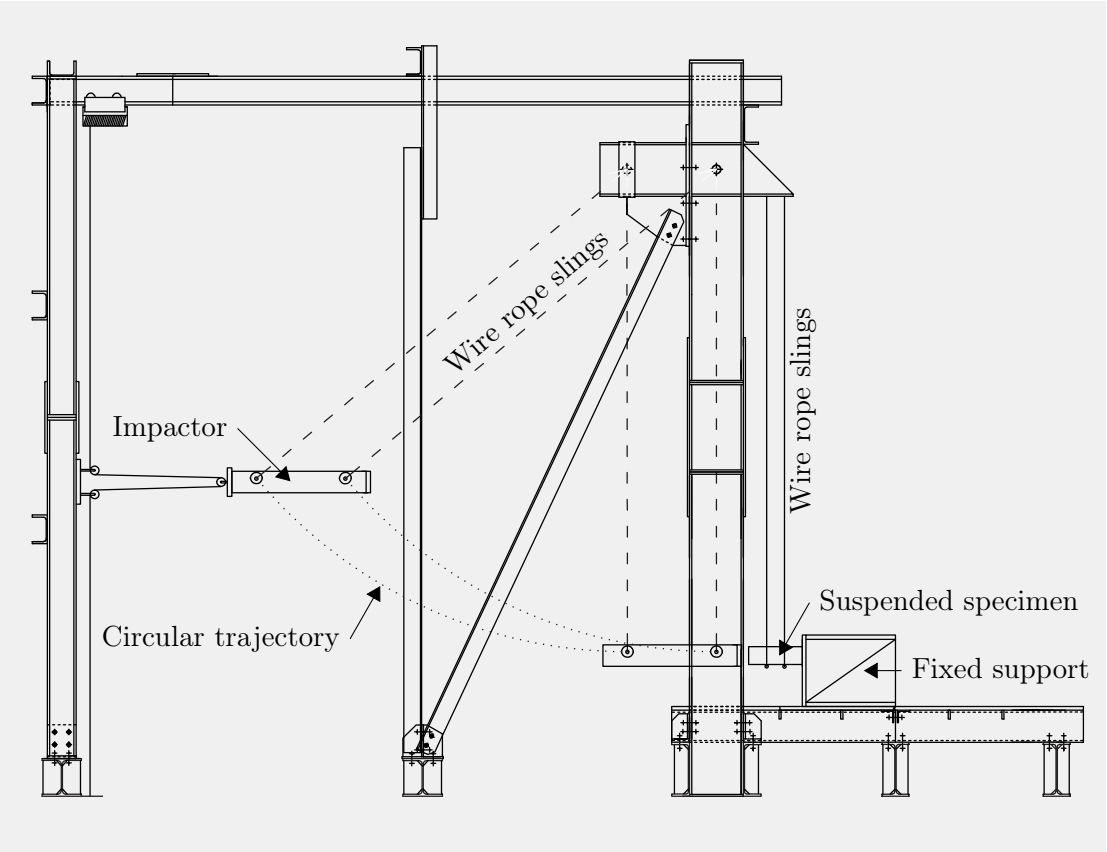

Figure 3.4: Sketch of the horizontal impact machine.

to the sides of the impactor were averaged. A constant value, equal to the deviation from a zero value at the beginning of the impact, was then subtracted from the raw measured data in order to achieve zero initial conditions. The tared data were then filtered using the channel frequency class (CFC) of the low-pass filter [126–129] to remove high-frequency noise recorded during measurements. Filtering is the most critical phase in the processing of impact signals [126]: it reduces the peaks in the signal [129] that are used for determining peak force. The CFC filters were derived from analog Butterworth filters that had a corner frequency equal to the CFC designation divided by 0.6 [129]. To correctly choose the designation, numerical modal analysis of the impactor and Fast Fourier Transform (FFT) analysis of the measured data was conducted. The fundamental frequency of the impactor was 258 Hz and the significant frequencies of the cellular structure fracturing did not exceed 200 Hz. Therefore, CFC 120 was used to filter the measured data. Filtered high-frequency components had a negligible effect on the overall shape of the force-displacement curve and the resulting filtered curve was much smoother and easier to analyse.

Using Newton's second law, a vector sum of the forces (F) of the impactor was determined as the mass (m_0) of the impactor multiplied by its deceleration vector (a).

$$\mathrm{F} = m_0 \mathrm{a} \tag{3.20}$$

The time evolution of the impactor velocity (v) and its crush stroke (u) after crushing into the specimen was determined as the first and the second integral of the measured

deceleration (a):

$$v = \int a \mathrm{d}t \tag{3.21}$$

$$u = \int \int a \mathrm{d}t^2 \tag{3.22}$$

The initial impact velocity was verified using a high-speed camera recording and was in 99% agreement with the estimated value based on the drop height of the impactor. The high-speed camera was placed above the specimen and attached to a separate structure to eliminate vibration transmitted from the structure of the test device during the impact. The high-speed recordings were also used to observe progressive deformation of the specimens and the impactor deceleration. The specific point on the rigid impactor was tracked using fiducials which enabled tracking of the selected point during the impact. High-speed videos were used to determine the change in the movement (u) of the impactor. The time evolution of the impactor velocity (v) and the deceleration (a) were then determined as its first and second derivative:

$$v = \frac{\mathrm{d}u}{\mathrm{d}t} \tag{3.23}$$

$$a = \frac{\mathrm{d}^2u}{\mathrm{d}t^2} \tag{3.24}$$

The data were processed by multiple application of a smooth function, which eliminated the extreme values and smoothed the measured data. The obtained data were then compared with the data measured by the accelerometers and good agreement was achieved. The collapse of ceramic specimens was recorded with a frequency of 5000 fps. Fiducial points at high-speed videos were tracked using IDT MotionStudio software [130]. The data obtained from the tracking and accelerometers were processed using the graphical development environment LabView [131] included in the National Instruments Diadem software package.

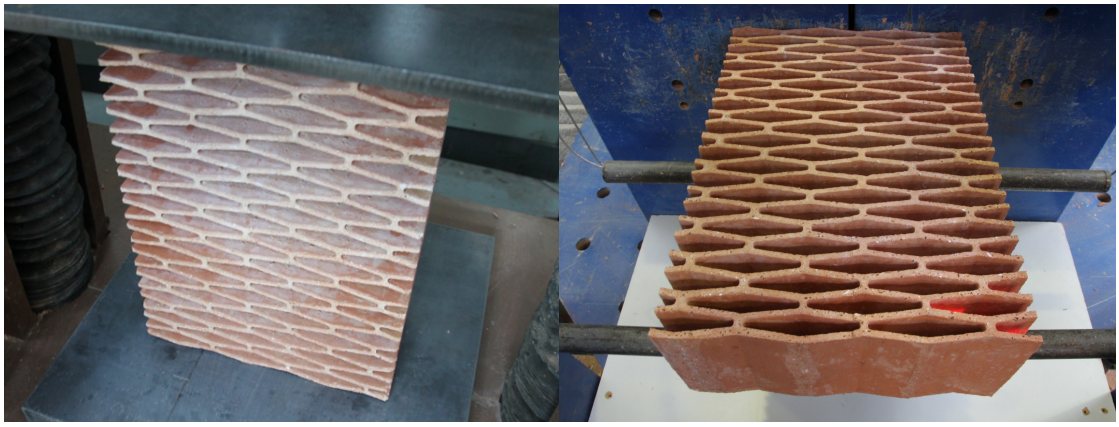

(a) Quasi-static test (b) Impact test

Figure 3.5: Sample STI44 to be tested under quasi-static (a) and impact (b) loading conditions.

3.3 Results and discussion

As outlined in the introduction, the main purpose of the tests was to identify blocks with different levels of crashworthiness. To investigate this, collapse modes, force-displacement curves, and indicators of crashworthiness were closely examined. Tests were conducted at least five times, each under identical test conditions to determine mean values of indicators of crashworthiness with acceptable standard deviations. The exact number of tests conducted is listed in Table 3.2.

3.3.1 Crushing process

As reported by Zheng et al. [57], the collapse of cellular structures subjected to quasi-static loading progresses from their weakest part. Due to the imperfections of the cellular structures mentioned in Section 3.2.2.1, the location of the weakest part was different for different samples tested and this resulted in a varying crushing process. Increasing the impact velocity, the inertia effect plays a more important role than the effect of an irregularity [57] and deformation starts from the impact face and then propagates from here [29]. Even though some irregularities were observed in the crushing process of the cellular structure under the impact loading—most likely due to the impact velocity not exceeding the limit level to suppress all the aforementioned imperfections—the following stages could be distinguished:

1. The impactor comes into contact with a sample; adjacent cells at the stricken end fracture.
2. Collapse progresses from the stricken end; the crushing band $\wedge$ is formed.
3. The crushing band $\vee$ is formed at the supported end; in the majority of cases, fractures of $\wedge$ and $\vee$ bands are combined, which causes a noticeable peak of the crushing force. Progress of the crushing band $\wedge$ stops and the collapse progresses from the supported end; in some cases, cell fracture at the stricken end can still be observed—most likely due to the cellular structure imperfections.
4. The crushing bands $\wedge$ and $\vee$ touch; the $\Diamond$ shape is formed for cells which do not fracture. The remaining cells in the $\Diamond$ are crushed; a more pronounced increase in the crushing force can be observed.
5. The crushing bands are flattened (=); pieces of debris are compacted and the crushing force increases rapidly with a relatively small increase in crushing displacement.
6. The pieces of debris are fully compacted (—); the maximum crush stroke is reached.

Crushing modes at different stages of compression for samples +40, +44, F30, F44, F50, and STI44 under impact loading are shown in Figure 3.6.

Table 3.2: The number of tests conducted.

Loading	+40	+44	F30	F44	F50	STI44
Quasi-static	6	8	9	8	9	8
Impact	11	10	15	14	11	5

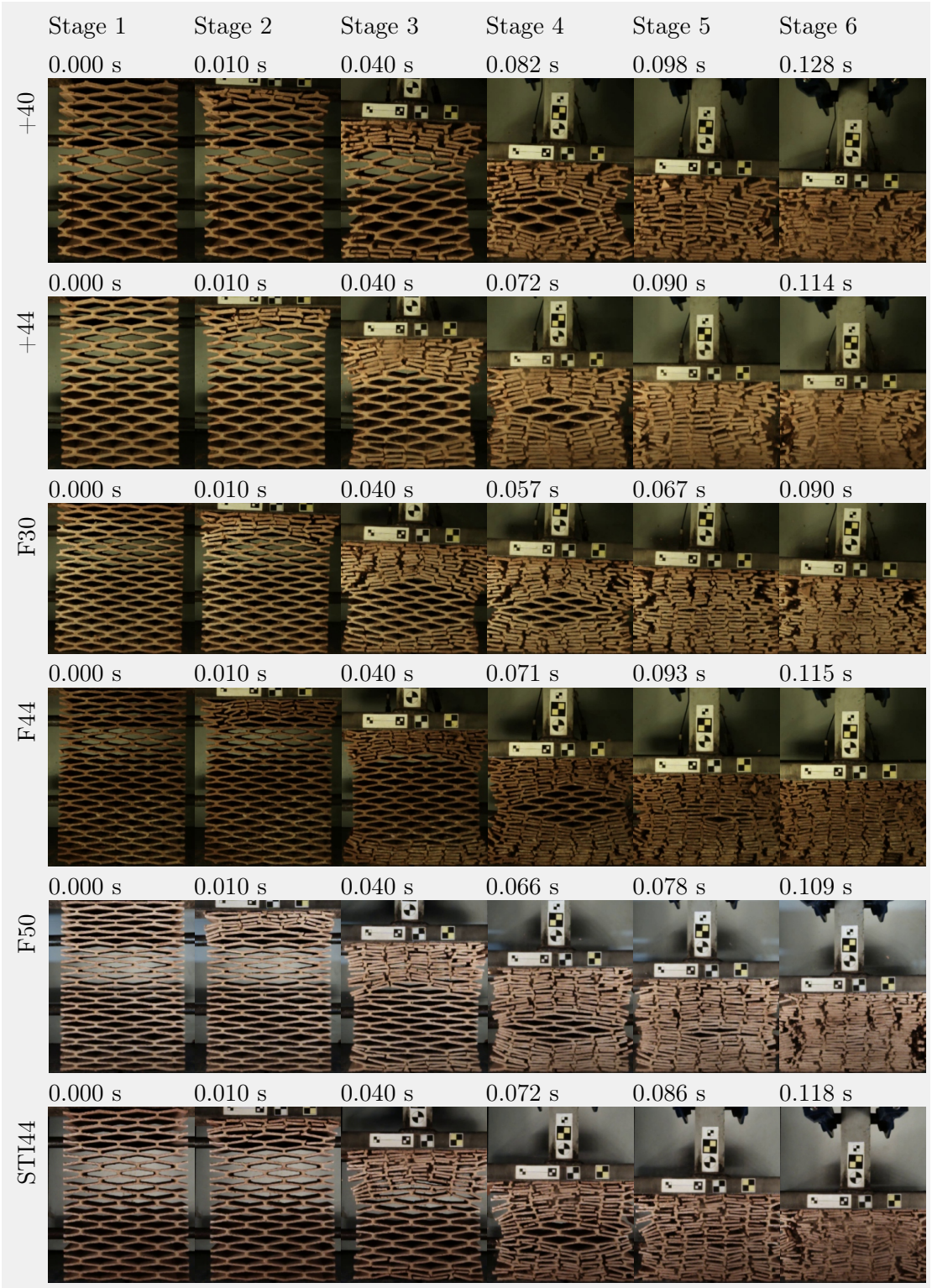

Figure 3.6: Different stages of the collapse of the tested specimens under impact loading. Timestamps in seconds.

3.3.2 Load response

Figures 3.7, 3.8, 3.9, 3.10, 3.11, and 3.12 illustrate the force-displacement curves for the selected samples from the series +40, +44, F30, F44, F50, and STI44, respectively. Curves of specimens with results closest to the mean values are shown.

It is apparent that the stroke under quasi-static loading is prolonged. This elongation is likely linked to debris fallout. During quasi-static loading, some parts broken off of the cellular structure fell down and did not accumulate between the movable and the stationary plate of the loading machine. Therefore, a longer crushing stroke was recorded than during impact loading during which the resulting pieces of debris were pushed in front of the impactor and subsequently accumulated between the impactor and the fixed support.

The average forces were significantly enhanced under impact loading. These enhancements are most likely linked to the inertia effect. The collapse mode changed as discussed in Section 3.3.1 and the area under the force-displacement curve also included work needed to accelerate the pieces of debris broken off of the cellular structure.

The peak forces are slightly enhanced under impact loading. This might be due to inertia and strain rate effects.

3.3.3 Indicators of crashworthiness

Due to the small variations in design and not negligible standard deviations of indicators of crashworthiness, the individual samples were mostly not compared among themselves. However, the samples could be divided into three groups with distinguishable design characteristics and crashworthiness: samples +40 and +44 with thick walls and wide cells (reduced number of cells in the direction perpendicular to the impact), samples F30 and F44 with thin walls and narrow cells, and samples F50 and STI44 with thin walls and wide cells.

The final comparison of individual samples is based on all indicators of crashworthiness as well as on multiple-criteria decision making methods and can be found in Section 3.4.

3.3.3.1 Energy absorption

The values of EA are listed in Table 3.3. The dynamic EA was significantly larger than the static EA. This is most likely linked to the inertia effect as discussed in Section 3.3.2. The mode of deformation changed and the collapse started from the stricken face; the formation of the $\Diamond$ shape led to the enhancement of structure stiffness; part of the impact energy was used to accelerate the pieces of debris broken off of the cellular structures.

The lowest amount of energy was absorbed by the samples with thin walls and wide cells. This indicates—regardless of the variation in the sample weight—that by narrowing cells and adding columns or by designing thicker walls, the EA could be significantly improved.

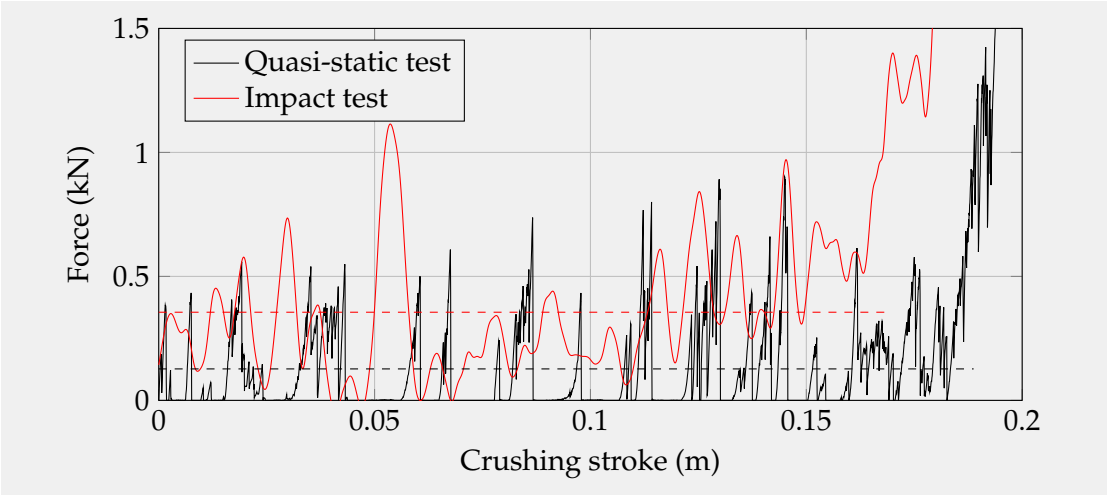

Figure 3.7: Force-crushing stroke curves of the tested specimen +40. Dashed lines represent the average forces.

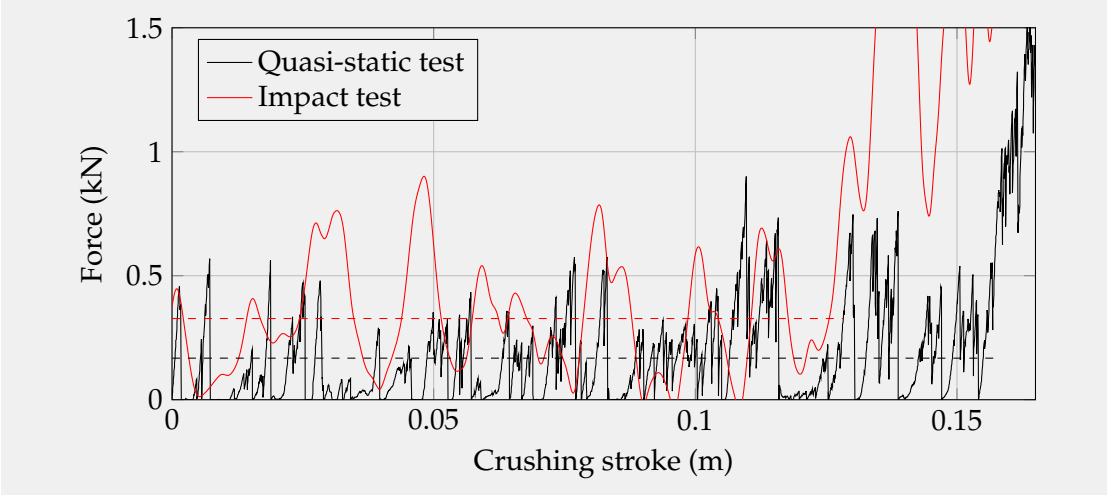

Figure 3.8: Force-crushing stroke curves of the tested specimen +44. Dashed lines represent the average forces.

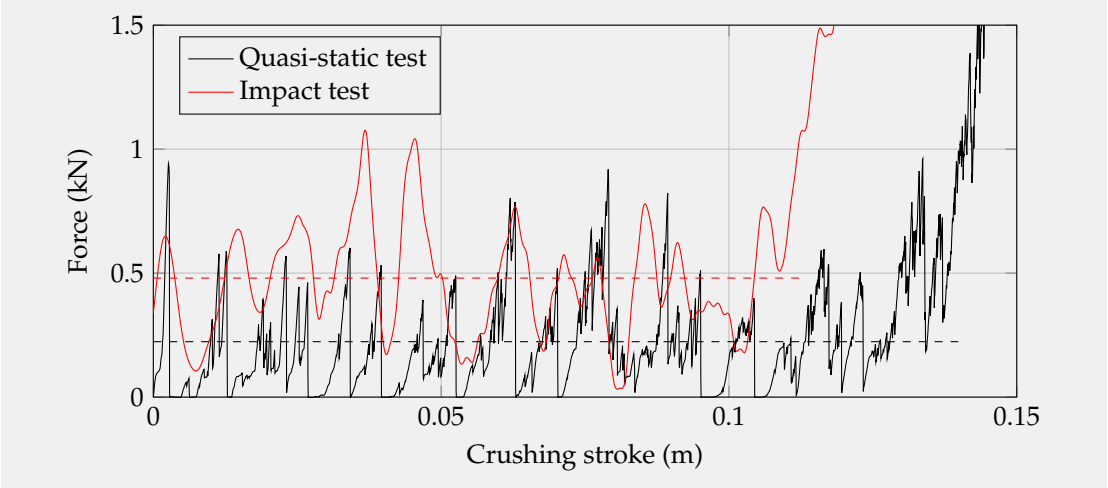

Figure 3.9: Force-crushing stroke curves of the tested specimen F30. Dashed lines represent the average forces.

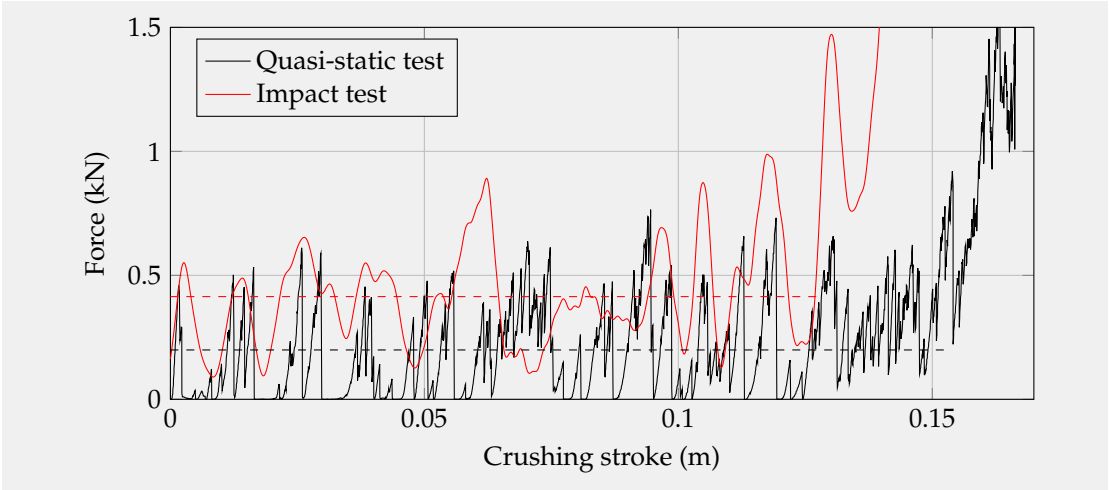

Figure 3.10: Force-crushing stroke curves of the tested specimen F44. Dashed lines represent the average forces.

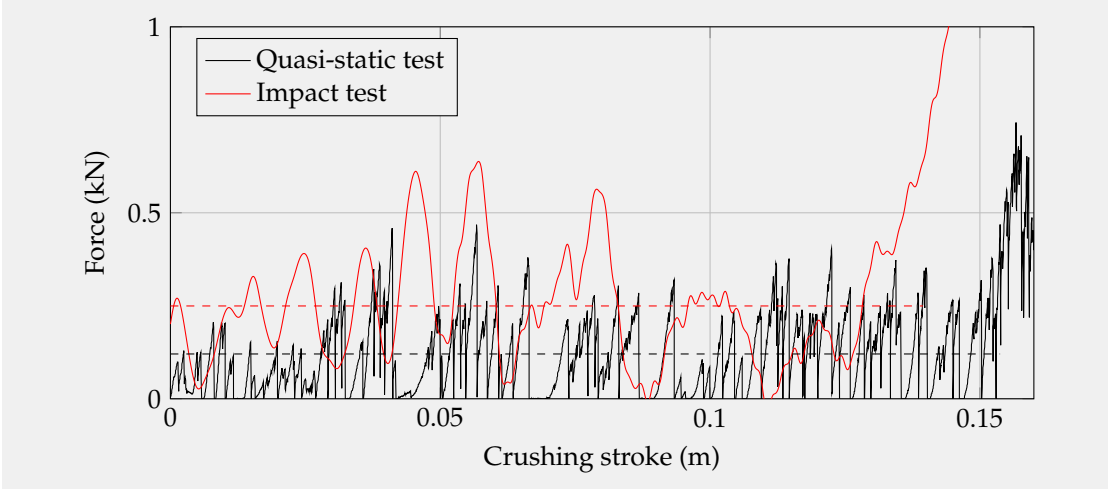

Figure 3.11: Force-crushing stroke curves of the tested specimen F50. Dashed lines represent the average forces.

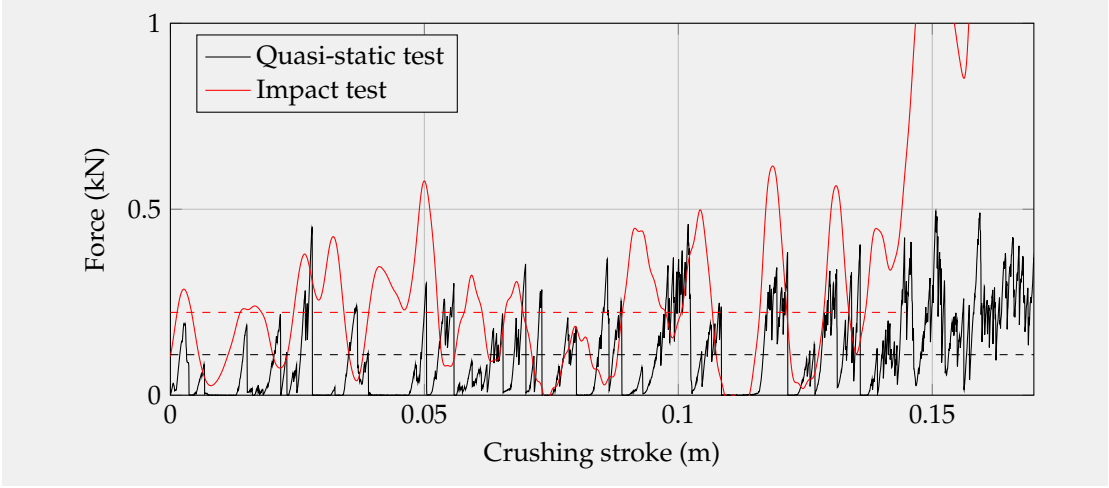

Figure 3.12: Force-crushing stroke curves of the tested specimen STI44. Dashed lines represent the average forces.

Table 3.3: Energy absorption. Values in parentheses give the standard deviation. Values obtained for smaller specimen F30 are written in italics. Values in J.

Loading	+40	+44	F30	F44	F50	STI44
Quasi-	32.2	31.4	28.5	29.7	17.3	14.5
static	(5.8)	(4.7)	(3.2)	(3.6)	(2.8)	(3.2)
Impact	58.3	48.6	50.8	53.5	32.8	31.4
	(4.7)	(8.1)	(7.9)	(6.7)	(2.9)	(1.6)

Table 3.4: Peak crush force. Values in parentheses give the standard deviation. Values obtained for smaller specimen F30 are written in italics. Values in N.

Loading	+40	+44	F30	F44	F50	STI44
Quasi-	1015	978	944	803	456	420
static	(121)	(118)	(115)	(138)	(77)	(101)
Impact	1134	988	1063	981	631	576
	(141)	(224)	(200)	(187)	(65)	(31)

3.3.3.2 Peak crush force

The values of PCF are listed in Table 3.4. The dynamic PCF was slightly larger than the static PCF. Possible reasons for this are mentioned in Section 3.3.2.

In contrast to EA, the most desired response in terms of PCF shows samples with wide cells and thin walls. This indicates that in order to avoid high deceleration felt by the occupants of a vehicle being impacted, wider cells with thinner walls should be designed. The contrast to EA was expected since an increase in EA is usually associated with an increase in PCF. Therefore, other indicators are needed to compare the overall crashworthiness of samples.

3.3.3.3 Energy absorption efficiency

The values of EAE are listed in Table 3.5. The dynamic EAE was significantly larger than the static EAE, because the EA was enhanced more significantly under the impact loading than the PCF.

To decide if a sample with a lower PCF or a larger EA is desired, EAE is useful indicator. However, its value in our study did not vary significantly among the samples and it can be concluded that the samples tested had a very similar ability to absorb a certain amount of energy and to control the force response within the desired range.

Table 3.5: Energy absorption efficiency. Values in parentheses give the standard deviation. Values obtained for smaller specimen F30 are written in italics. Values in J/kN.

Loading	+40	+44	F30	F44	F50	STI44
Quasi-	31.7	32.1	30.4	37.4	38.1	34.7
static	(5.8)	(3.1)	(3.3)	(3.3)	(4.6)	(3.3)
Impact	52.4	49.9	48.2	55.3	52.3	54.6
	(4.8)	(5.1)	(4.4)	(5.1)	(5.6)	(1.9)

Table 3.6: Specific energy absorption. Values in parentheses give the standard deviation. Values obtained for smaller specimen F30 are written in italics. Values in J/kg.

Loading	+40	+44	F30	F44	F50	STI44
Quasi-static	8.33 (1.44)	7.30 (1.05)	8.27 (0.93)	7.46 (0.91)	4.47 (0.70)	4.53 (1.00)
Impact	16.8 (1.8)	12.3 (2.3)	13.3 (1.8)	12.2 (1.3)	8.17 (0.56)	9.61 (0.56)

Table 3.7: Volume specific energy absorption. Values in parentheses give the standard deviation. Values obtained for smaller specimen F30 are written in italics. Values in J/dm^3.

Loading	+40	+44	F30	F44	F50	STI44
Quasi-static	5.11 (0.92)	4.96 (0.75)	5.10 (0.57)	4.54 (0.55)	2.74 (0.45)	2.27 (0.50)
Impact	9.27 (0.75)	7.67 (1.28)	9.08 (1.42)	8.17 (1.03)	5.20 (0.48)	4.94 (0.26)

3.3.3.4 Specific energy absorption and volume specific energy absorption

The values of SEA and $VSEA$ are listed in Table 3.6 and Table 3.7 respectively. The SEA and $VSEA$ were significantly enhanced under dynamic loading for the reason mentioned in Section 3.3.3.1.

Analogous to EA, the samples with thin walls and wide cells exhibited the lowest SEA and $VSEA$ values. It could be inferred that to maximise material utilisation for energy absorption, mass should be concentrated on the walls, or cells could be narrowed and a column added.

3.3.3.5 Mean crush force

The values of MCF are listed in Table 3.8. The dynamic MCF was significantly larger than the static MCF for the reasons mentioned in Section 3.3.2.

The lowest MCF was recorded for the samples with thin walls and wider cells, especially sample STI44. It can be inferred that STI44 would be the most suitable block for use in mitigating vehicle collision injuries. The highest MCF was recorded for the samples with thin walls and narrow cells. This suggests that the considered variation in cell width has a more significant effect on MCF than the considered variation in cell wall thickness. It can be derived that by reducing the number of cells in the direction perpendicular to the expected impact, the risk of injury during vehicle collisions could be reduced.

Table 3.8: Mean crush force. Values in parentheses give the standard deviation. Values obtained for smaller specimen F30 are written in italics. Values in N.

Loading	+40	+44	F30	F44	F50	STI44
Quasi-static	176 (32)	193 (27)	212 (21)	192 (16)	118 (18)	84 (18)
Impact	357 (25)	352 (48)	446 (55)	410 (37)	248 (23)	211 (13)

Table 3.9: Crush force efficiency. Values in parentheses give the standard deviation. Values obtained for smaller specimen F30 are written in italics. Dimensionless.

Loading	+40	+44	F30	F44	F50	STI44
Quasi-static	0.172 (0.032)	0.197 (0.011)	0.226 (0.025)	0.243 (0.025)	0.261 (0.025)	0.201 (0.016)
Impact	0.318 (0.028)	0.365 (0.050)	0.426 (0.046)	0.427 (0.055)	0.395 (0.044)	0.367 (0.007)

Table 3.10: Crush efficiency. Values in parentheses give the standard deviation. Values obtained for smaller specimen F30 are written in italics. Dimensionless.

Loading	+40	+44	F30	F44	F50	STI44
Quasi-static	0.592 (0.044)	0.525 (0.036)	0.516 (0.022)	0.500 (0.024)	0.477 (0.036)	0.557 (0.039)
Impact	0.526 (0.025)	0.443 (0.032)	0.435 (0.027)	0.422 (0.024)	0.433 (0.021)	0.479 (0.011)

3.3.3.6 Crush force efficiency

The values of CFE are listed in Table 3.9. The dynamic CFE was larger than the static CFE because MCF was enhanced more significantly under impact loading than PCF.

The highest CFE was recorded for the samples with narrow cells, likely because of their enhanced MCF. This suggests that the increased number of cells in the direction perpendicular to an expected impact might be preferred to achieve a more stable reaction force through the crushing process. However, the difference in the results was too small to draw any substantive conclusions.

3.3.3.7 Crush efficiency

The values of CE are listed in Table 3.10. The static CE was larger than the dynamic CE. This was most likely linked to the accumulation of the pieces of debris broken off of the cellular structure as discussed in Section 3.3.2.

CE was similar among samples and therefore it was not possible to identify a design with the highest amount of material utilised during the collapse.

3.3.3.8 Energy efficiency

The values of EE are listed in Table 3.11. The comparison based on EE was analogous to EAE with the exception of the shorter sample F30. However, not even when the length of the sample was taken into account, a clear difference in the response of samples was not observed.

3.3.3.9 Work efficiency

The values of WE are listed in Table 3.12. Dynamic WE was much larger than static WE because the reduction of CE was less significant than the increase of SEA.

Sample +40 exhibited significantly larger WE than the rest of the samples. This indicates that it is capable of absorbing a significant amount of impact energy and allows for the deceleration of the impacting body on a large stroke. This sample could be used when

Table 3.11: Energy efficiency. Values in parentheses give the standard deviation. Values obtained for smaller specimen F30 are written in italics. Dimensionless.

Loading	+40	+44	F30	F44	F50	STI44
Quasi-static	0.102 (0.014)	0.104 (0.010)	0.117 (0.013)	0.121 (0.011)	0.124 (0.015)	0.112 (0.011)
Impact	0.167 (0.016)	0.161 (0.016)	0.185 (0.017)	0.179 (0.016)	0.171 (0.018)	0.176 (0.006)

Table 3.12: Work efficiency. Values in parentheses give the standard deviation. Values obtained for smaller specimen F30 are written in italics. Values in J/kg.

Loading	+40	+44	F30	F44	F50	STI44
Quasi-static	4.93 (0.97)	3.84 (0.70)	4.28 (0.60)	3.75 (0.62)	2.14 (0.42)	2.53 (0.61)
Impact	8.88 (1.32)	5.51 (1.40)	5.80 (1.05)	5.18 (0.80)	3.54 (0.36)	4.60 (0.25)

a culvert with limited space and cost and high energy absorbing requirements would be desired. Sample F50 exhibited the lowest amount of WE.

3.3.4 Multiple-Criteria Decision Making Method

EA, PCF and CFE were taken as design criteria as discussed in 3.2.1.2. Because EA and CFE are not independent of sample dimensions, the shorter sample F30 was excluded from the comparison. The score and ranking of samples tested are shown in Table 3.13. It should be mentioned that the ranking of samples would change when different design criteria would be considered. Those should always be chosen with respect to the intended application of an EAS.

Samples with thick walls and wide cells were ranked as last because large peaks of unstable crushing force were recorded during the experiments.

Samples with thin walls and wide cells exhibited were less able to absorb energy and their crushing force was almost as unstable as that of the samples with thick walls and wide cells. However, their PCF and the corresponding deceleration acting on the impacting body were lower than those of the rest of samples. According to both TOPSIS and COPRAS methods, this reduction of the parameter indicating the likelihood of injury is numerically more significant than the reduction of energy absorption ability.

Table 3.13: Score and ranking of tested samples according to TOPSIS and COPRAS methods.

	TOPSIS		COPRAS	
	U_i	Rank	U_i	Rank
+40	82.2%	4	90.6%	5
+44	79.7%	5	91.1%	4
F44	100%	1	100%	1
F50	93.1%	2	97.1%	3
STI44	92.6%	3	97.5%	2

Sample F44—the only sample with narrow cells—was identified as the block with the best compromise between low deceleration felt by imagined vehicle occupants, large energy absorption, and fairly stable reaction force throughout the crushing process.

3.4 Conclusions

This study investigated the responses of brittle blocks with thin-walled cellular structures to quasi-static and impact loading. To the knowledge of the author, the presented data is the first of its kind. The following inferences can be drawn from the study:

1. Brittle blocks tested here were able to absorb impact energy because of the gradual brittle fracture process in their cellular structures.
2. It was shown that relatively small changes in the design can lead to production of blocks with distinguishable levels of crashworthiness.
3. The blocks exhibited different levels of crashworthiness at different loading rates.
4. Even though the crushing process under quasi-static loading is relatively random, the crushing process under impact loading can be divided into four main stages: collapse progressing from the stricken end; collapse progressing from the support end; a touch of the crushing bands and a collapse of cells in between; and compaction of the pieces of debris.
5. The maximum crush stroke was enlarged under quasi-static loading. This was most likely linked to debris fallout. During quasi-static loading, some parts broken off of the cellular structure fell down and did not accumulate between the movable and the stationary plate of the loading machine. Therefore, a longer crushing stroke was recorded than during impact loading, when the resulting pieces of debris were pushed in front of the impactor and subsequently accumulated between the impactor and the fixed support.
6. A significant increase in average crush force and associated energy absorption under impact loading were observed. This is most likely linked to the inertia effect. The mode of deformation changed and the collapse first progressed from the impact face and later from the support end. As the collapse progressed, the crushing bands touched, which led to the stiffening of cellular structure and enhancement of crushing force. Part of the impact energy was also used to accelerate the pieces of debris broken off of the cellular structure, which also enhanced the average crush force.
7. Enhancement of the peak crush force was also observed. This might be linked to inertia and strain rate effects.
8. Indicators of crashworthiness EA, SEA, $VSEA$, PCF, MCF, and WE, as well as both multiple-criteria decision making methods TOPIS and COPRAS were found to be very useful in this comparative study. On the contrary, the ranges of values obtained for indicators of crashworthiness EAE, CE, CFE, and EE were too small to draw any substantive conclusions.
9. The sample cut out of manufactured block HELUZ Plus 40 was able to absorb a significant amount of impact energy and allowed for the deceleration of the impacting body on a large stroke. Its design was the best when restricted in terms of both weight and space. On the other hand, a large and unstable crushing force was recorded during the sample's crushing process. It could be used when a culvert

with limited space and cost and high energy absorbing requirements would be desired. It will be considered as a semi-soft element in subsequent studies devoted to the study of the combination of samples with different crashworthiness measures.

10. The sample cut out of manufactured block HELUZ STI 44 was found to be the most suitable sample for reducing the risk of injury and to avoid high deceleration felt by occupants in a vehicle collision. Unfortunately, it was also characterised by the lowest energy absorption. It could be used as a cushioning element in culverts where the injury risk should be minimised and sufficient space would be available. It will be considered as a soft element in subsequent studies devoted to the study of the combination of samples with different crashworthiness measures.

11. The sample cut out of manufactured block HELUZ Family 44 was identified as the sample with the best compromise between low deceleration felt by occupants, large energy absorption, and fairly stable reaction force through the crushing process.

Chapter 4

Energy-absorbing system made of high-performance concrete

Abstract

This chapter[1] is devoted to the experimental development of a high-load-bearing energy-absorbing system (EAS) made of high-performance concrete (HPC). The HPC employed in this study is a self-consolidating concrete with fast strength development that does not require heat curing or special mixing techniques. All of its components are commonly available in large volumes for a reasonable price, and the resulting material is characterised by reasonable volume stability and very low porosity, which makes it highly durable. The production process is described in detail and the resulting EAS is subjected to a complete testing program, including impact and quasi-static tests. The numerical analyses are also conducted and their outputs validated against experimental measurements. It is demonstrated that it is possible to develop an energy-absorbing system made of high-performance concrete with controlled impact force and deceleration. This specification, coupled with load-carrying capacity and long term durability, will allow for a wide range of applicability even in places where currently produced energy-absorbing systems cannot be installed.

Highlights

- An energy absorbing system (EAS) made of HPC is introduced.
- Full-scale and reduced-scale impact tests as well as quasi-static tests are conducted.
- Numerical models are developed to reproduce the tests.
- Numerical results are validated against experimental measurements.
- Reasonable deceleration of a cart impacting an HPC-EAS is recorded.

[1] reproduced from Petr Hála et al. "Energy absorbing system made of high performance concrete". In: Construction and Building Materials 139 (2017), pp. 64–80. issn: 09500618. doi: 10.1016/j.conbuildmat.2017.02.048.

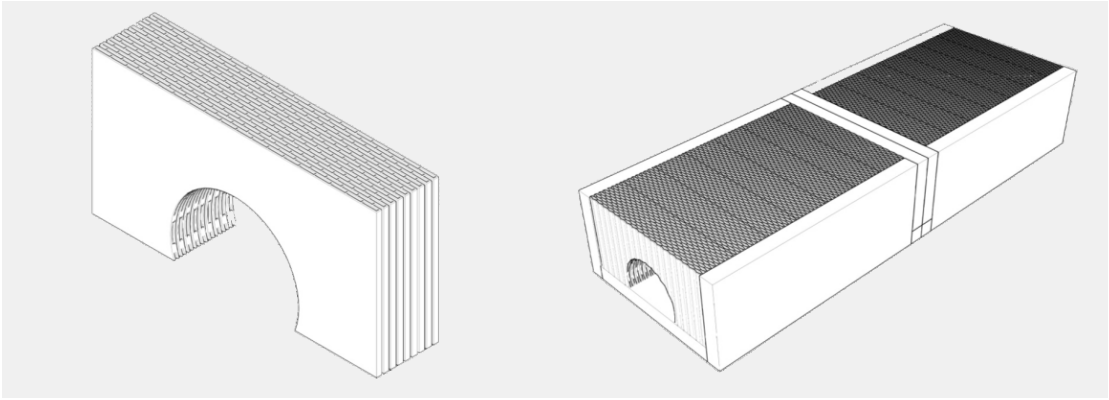

Figure 4.1: The proposed energy absorbing system and its possible use as a cushioning element in a cross-drainage culvert.

4.1 Introduction

There has been an increase in the number of vehicles due to advances in transport technology, which inevitably led to an increase in the number of traffic accidents. Over the years, safety features such as restraint systems, airbags or crumple zones have been introduced and become an integral part of vehicles. Another important strategy for increasing road safety is to prevent the vehicle from colliding with fixed objects by protecting or replacing the object with an energy-absorbing system (EAS) [132]. Many EAS are made of aluminium [132] or aluminium foam [133], high-strength carbon fibres embedded in an epoxy resin [134], glass fibre/epoxy laminated composites [79], bamboo [135], metallic materials such as thin-walled round tubes [42] or fired clay [1, 2]. Most of these EAS have a limited lifetime in harsh environmental conditions and may, therefore, fail during the service life of a structure, e.g. bridge column, culvert, etc. This chapter proposes a novel energy-absorbing system made of high-performance concrete (Figure 4.1) with suitable energy-absorbing properties and service life of over 75 years in accordance with the expected service life of the structure [136].

The latest energy absorbing system made of concrete was introduced by Shen et al. [13]. They designed a block with a developed network of micro-cracks throughout its volume. During the impact, the micro-cracks propagated, connected, and disintegrated the safety block into fragments smaller than 4.7 mm. It was reported that a highway crash barrier made of such concrete could reduce the velocity of an impacting vehicle and thus protect vehicle passengers.

4.2 Material

4.2.1 General remarks

Several researchers have reported that HPC has the potential to address the poor condition of ageing infrastructure [137]. It is a composite material containing a large volume of cement paste with a low water-binder ratio, high microsilica content, and only fine aggregates, i.e., smaller than 4 mm [138]. The use of cementitious admixtures, such as microsilica, has become common practice in modern concrete construction for economic, technical and environmental reasons [139]. HPC has outstanding material characteristics such as self-consolidating workability, very high strength and modulus of elasticity [140], and very low permeability preventing any of the physio-chemical deterioration processes

Table 4.1: Mix proportion of high-performance concrete.

Lafarge cement 42.5R	1
Silica fume	0.1
Silica flour	0.25
Silica sand with max. aggregate size 1.2mm	1.6
Plasticising additive	0.01
Anti-foaming additive	0.001
Water	0.3

[141] and resulting in excellent environmental resistance [142–145]. With increased resistance to de-icing chemicals and freeze-thaw cycles, HPC is suitable for use in harsh environmental conditions. Hypothetically, it can also be used in underwater protection of bridge piers. All of its components are commonly available in large volumes at a reasonable cost and the resulting material can be moulded into various shapes making it easily adjustable to any possible impacting mass or velocity in order to control impact force and deceleration.

4.2.2 Mix design

Material composition of HPC used in this study was taken from the design of a multifunctional dry prefabricated cementitious composite material with rapid strength development originally developed at Czech Technical University in Prague [146–148] and its mix proportion is listen in Table 4.1. The focus was on the material durability including microstructural densification by deliberate gradation of aggregates. No heat curing or special mixing techniques were required during the production process. All HPC components excluding water were initially mixed in a 750 kg capacity mixer for 90 seconds. This included cement, fine sand with a maximum grain size of 1.2 mm, silica powder, silica fume (microsilica), and high range powder water reducers. The dry prefabricated composite was then packed in 12 kg bags. Afterwards, the bags were transported to a laboratory where the dry mixture was mixed in vertical laboratory mixers with water for 5 minutes in required volumes. The resulting mixture had flowable and self-consolidating characteristics and the deformation blocks of EAS were made by pouring the fresh mixture to a single point of the mould and allowing it to flow and gradually fill the entire mould. The mixture offered a good compromise between an easy manipulation, controlled hydration process, and reasonable speed of solidification, which was ideal for the proposed application. The HPC was characterised by reasonable volume stability and very low porosity, which made it highly durable [141]. Specimens made for determination of mechanical properties were demoulded after 24 hours and cured at an ambient temperature of 21 ℃ and relative humidity of 50%.

4.2.3 Mechanical properties

Mechanical properties of the HPC were determined from the conventional procedures and the results are summarised in Table 4.2. Compressive strength, secant modulus of elasticity and Poisson's ratio of HPC were measured in a hydraulic loading machine on cylinders with a diameter of 100 mm and a height of 200 mm. Prior to testing, the top and bottom surfaces of the cylinders were cut off. In the first step of compressive strength measurement, the cylinders were subjected to monotonic increments of load at speed 36 MPa/min up to 70% of expected maximal compressive strength. Following this, the loading was switched to displacement control at speed 0.36 mm/min for about 2 minutes

Table 4.2: Measured mechanical properties of HPC. Values in parentheses give the standard deviation.

Compressive cylinder strength (MPa)	85.46 (4.76)
Compressive cubic strength (MPa)	122.8 (8.2)
Tensile strength (MPa)	3.884 (0.329)
Modulus of elasticity (GPa)	49.57 (1.25)
Poisson's ratio (-)	0.203 (0.012)
Modulus of rupture from 3-point bending test (MPa)	7.705 (0.836)
Modulus of rupture from 4-point bending test (MPa)	6.302 (0.705)
Bulk density (kg/m3)	2245 (4)

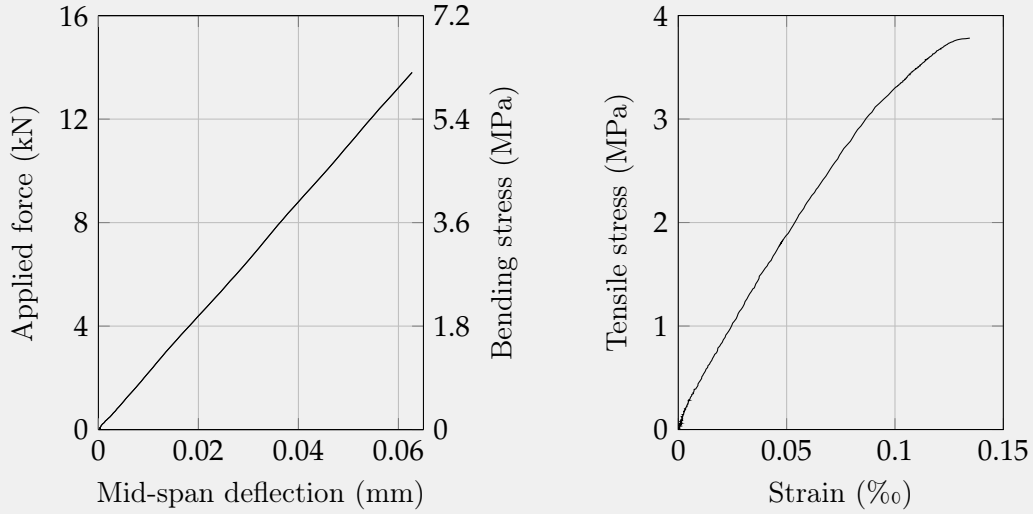

(a) A four-point bending test.

(b) A direct tensile test.

Figure 4.2: Results of tests conducted to determine mechanical properties of HPC.

in order to accurately measure peak strength and post-peak behaviour. The modulus of elasticity and Poisson's ratio were measured using two strain gauges with a 50 mm base, attached vertically to the sides of the cylinder specimen and another strain gauges glued around the circumference of the cylinder in the middle of its height. The tests were stress controlled. In the first step, specimens were loaded to 1/3 of expected maximal compressive strength—in this case 30 MPa—for 60 seconds. Afterwards, specimens were unloaded to 5 MPa. This procedure was repeated three times. The secant modulus of elasticity and Poisson's ratio were calculated during the third unloading cycle. Modulus of rupture in three-point bending test was measured on prismatic specimens with dimensions of 100 mm × 100 mm × 400 mm and a clear span of 300 mm. The loading speed was 0.1 mm/min. Modulus of rupture (Figure 4.2a) in four-point bending test was measured on prismatic specimens with dimensions of 100 mm × 100 mm × 550 mm and a clear span of 450 mm. The constant moment region was 150 mm long and the loading speed was 0.05 mm/min. The deflection was measured at the mid-span of the prism. A direct tensile test (Figure 4.2b) was carried out on dog-bone specimens without a notch. The narrow part of the specimen was 200 mm long and had a cross-section of 50 mm × 100 mm. The total length of the specimen was 750 mm. The specimens were mounted in specially developed grips and the loading speed was 0.1 mm/min.

4.3 Prototype development of EAS

4.3.1 General remarks

EAS presented in this study was designed to dissipate impact energy during a car crash because of the gradual brittle fracture process in its cellular structure. Several studies have shown that the fracture energy of HPC is very low, e.g. [140]. This was also confirmed during the determination of the mechanical properties when a brittle failure was observed almost immediately after reaching the peak strength. The main idea behind the development of EAS is to exploit this fragility by providing a very high number of fracture elements with reasonably low fracture work per single element. The design was based on the assumption that the crumple zones of the vehicle would not be crumpled prior to the end of the EAS collapse. This means that the energy absorption process must be as follows:

1. The vehicle comes into contact with an EAS that protects a structure or forms a cross-drainage culvert.
2. The vehicle crushes the EAS; the vehicular crumple zones are not crumpled.
3. The impact energy is dissipated only by the deformation process of the EAS, which can be divided into two fundamental modes:

   mode 1: brittle fracture of cells,

   mode 2: material accumulation.
4. The vehicle stops or reaches the end of the EAS (i.e. the protected structure) at reduced velocity. Only at this point can the vehicular crumple zone be crumpled.

A large number of cells in EAS is desired in order to dissipate impact energy gradually and to control the impact force and vehicle deceleration within the desired range. The flowability of the HPC made it possible to design a cell wall with a thickness of 10 mm. The cell area was 100 mm x 15 mm to keep the volume fraction of the HPC in the block below 50%. The dimensions of the entire block were 125 mm $\times$ 1000 mm $\times$ 250 mm (height $\times$ width $\times$ length). The exact volume fraction of HPC in the block was 45.7% and the corresponding cell volume fraction was 54.3%.

4.3.2 Production process

The deformation blocks made of HPC were produced in the lab using a special mould developed for the purpose of this study. The mould consisted of stationary and movable parts. The stationary part was represented by a hollow rectangular steel block with a height of 250 mm and inner dimensions of 250 mm $\times$ 1000 mm. Its bottom was perforated as shown in Figure 4.3a and the dimensions of the openings were 16 mm $\times$ 102 mm. The movable part consisted of 100 rectangular steel rods (Figure 4.3b) with a cross-section of 15 mm $\times$ 100 mm and a height of 200 mm.

Steel rods were inserted through the openings in the bottom part and the fresh mixture was poured into the mould. The rods were removed (Figure 4.3c) after a few hours using a pair of manual jacks, leaving the HPC in the desired position to fully develop its properties (Figure 4.3d). The block was demoulded the next day. During the demoulding, the frictional force was developed between the mould and HPC and in consequence, the upper side of the specimen decline unevenly. Therefore, it was necessary to grind it after 28 days to allow block stacking.

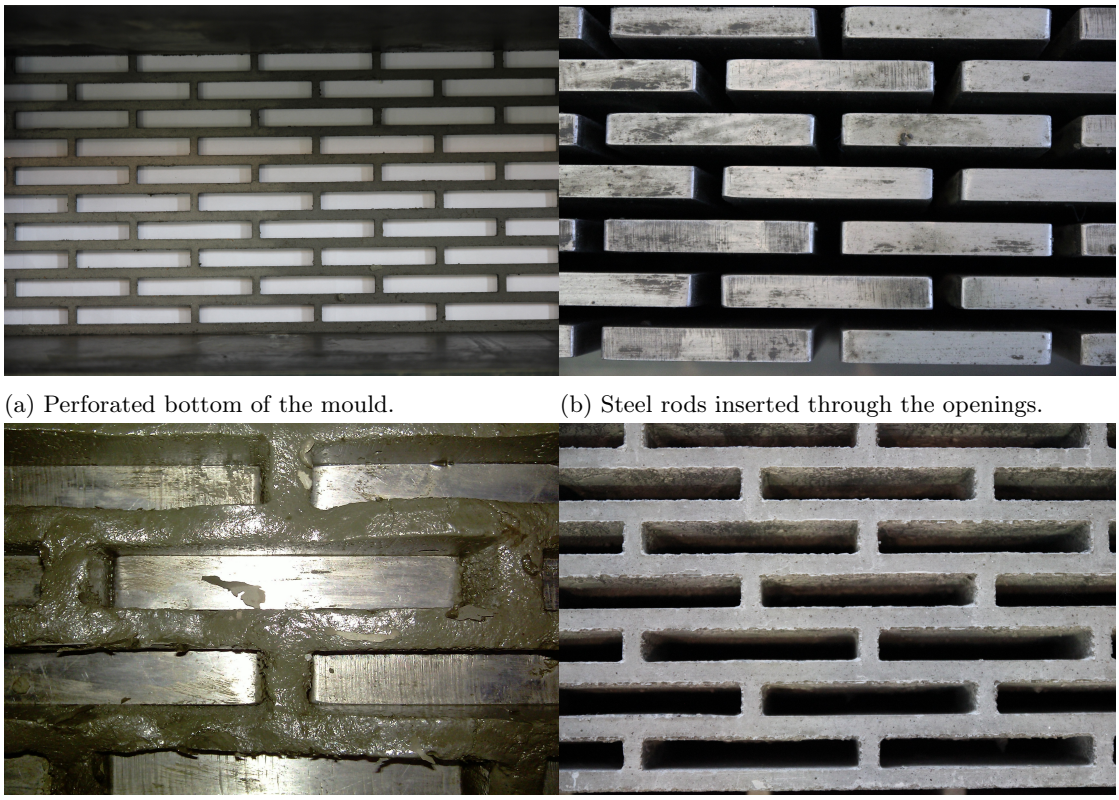

(a) Perforated bottom of the mould.

(b) Steel rods inserted through the openings.

(c) Removing the steel rods from the HPC.

(d) Detail of the hardened deformation block.

Figure 4.3: The production process of a deformation block.

4.3.3 Testing procedure

The produced block was subjected to full-scale and reduced-scale impact tests as well as a quasi-static test.

4.3.3.1 Full-scale impact test

Full-scale impact test was performed using 1000 kg non-deformable flat-nosed impact cart (Figure 4.4a) with an impact velocity of 30 km/h (8.33 m/s), which set impact energy at 34.7 kJ. The full-scale specimen was comprised of 24 deformation blocks, 4 tall and 6 long (Figure 4.4b). The length of the specimen was 1500 mm and the dimensions of the front face of the specimen were 500 mm × 1000 mm (height × width). The crash test was monitored with several high-speed cameras operating at frequency 3000 frames per second and with an accelerometer attached to the nose of the impact cart. There was no lateral boundary constraint at the sides of the specimen and its movement in the direction of the impact was restricted by the rigid support behind it (Figure 4.4c).

4.3.3.2 Reduced-scale impact test

The experimental setup for the reduced-scale impact test utilises a horizontal impact direction with a stationary specimen. The pendulum machine is shown in Figure 4.5a. During the tests, the impactor travels in a circular trajectory, guided by the wire rope slings. The impact energy can be varied by hoisting the impactor to different positions. The impactor had a steel flat rectangular nose with dimensions 120 mm × 400 mm (height × width) and a thickness of 30 mm to prevent its deformation during impact (Figure 4.5c). The impact velocity of the 50 kg impactor was 2 m/s which set impact

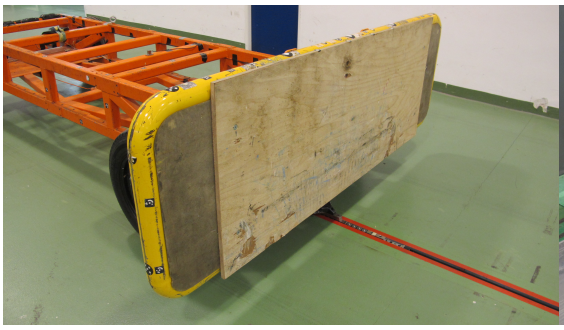

(a) Non-deformable flat-nosed impact cart.

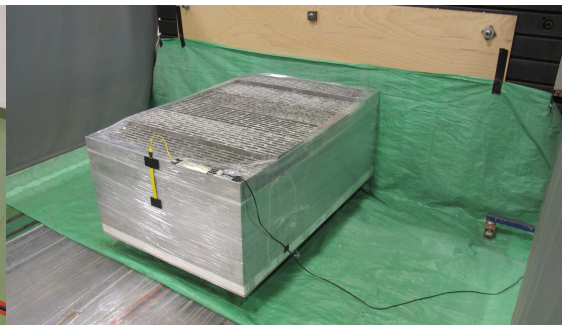

(b) Full-scale specimen.

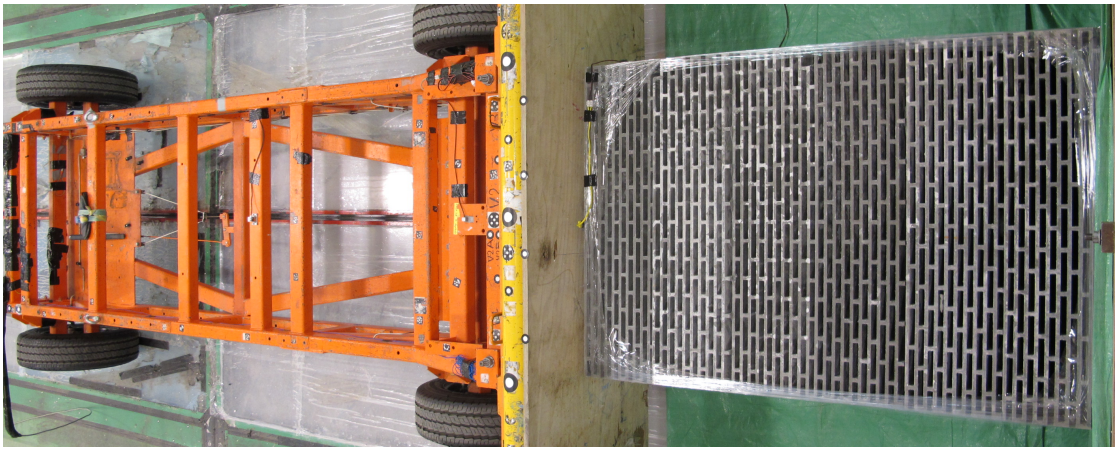

(c) The specimen between the impact cart and a rigid wall.

Figure 4.4: Full-scale impact test setup.

energy at 0.1 kJ. The reduced-scale specimen was obtained by cutting off one-third of the deformation block and its dimensions were 100 mm × 340 mm × 250 mm (height × width × length). Five specimens were prepared to prove repeatability of the experiments. Each specimen was suspended from the pendulum structure to avoid friction at the vertical support and located at the bottom return point of the impactor trajectory (Figure 4.5b). The progressive collapse of the specimen was recorded with a high-speed camera operating at frequency 2500 fps.

4.3.3.3 Quasi-static test

The EAS was designed not only to dissipate the kinetic energy of an impacting vehicle in one direction but also to have sufficient load-bearing capacity in the other to withstand the load generated by crossing vehicles or to support the weight of the structure. Therefore, three specimens—with the same dimensions as considered in reduced-scale impact tests (Figure 4.6a)—were quasi-statically loaded in the direction perpendicular to the expected impact. The hydrostatic loading machine consisted of stationary and movable parts both represented by a cylinder with a base diameter of 400 mm. The specimen was placed in the centre of cylinder's base and was subjected to monotonic increments of compression at speed 0.36 mm/min (Figure 4.6b). Only force produced by the loading machine was monitored.

(a) Horizontal impact pendulum machine.

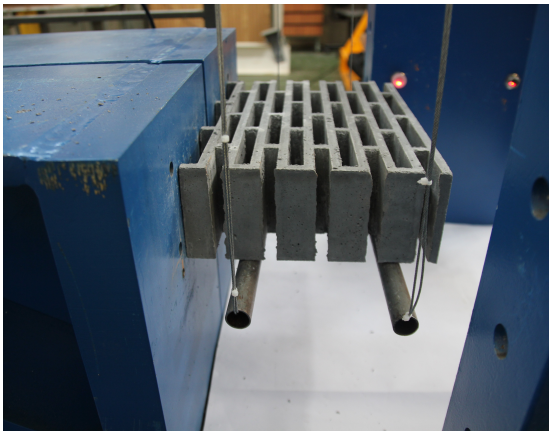

(b) Suspended reduced-scale specimen.

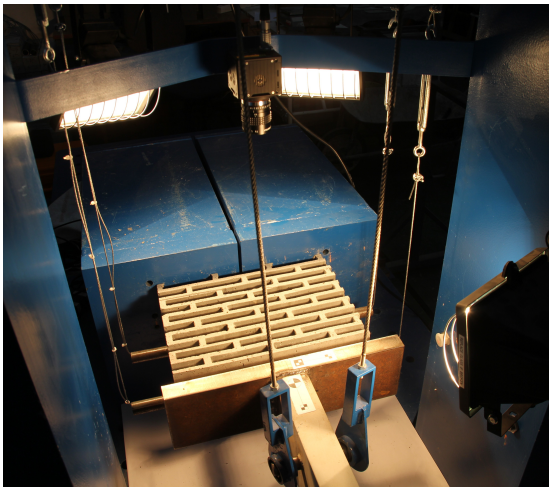

(c) Impactor in contact with the specimen.

Figure 4.5: Reduced-scale impact test setup.

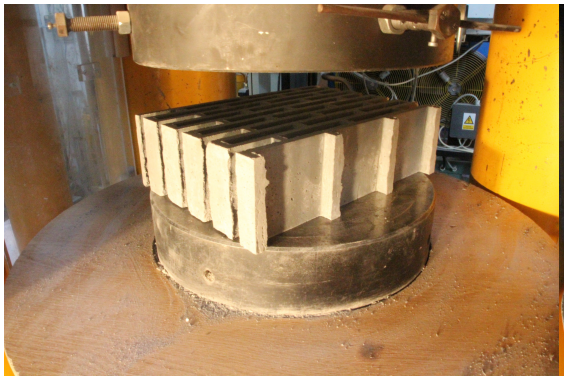

(a) Reduced-scale specimen.

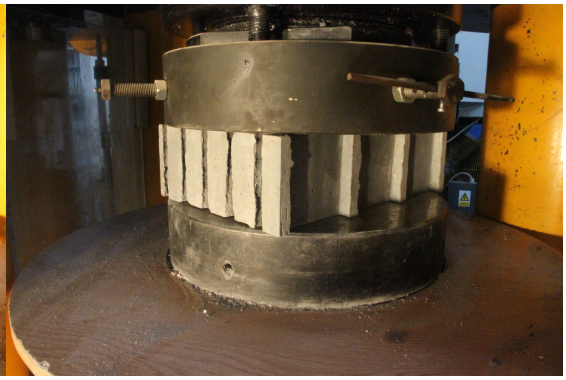

(b) Specimen subjected to quasi-static loading.

Figure 4.6: Quasi-static test setup.

4.4 Numerical analysis

4.4.1 General remarks

The numerical models were constructed with the finite element code LS-DYNA [149] and were validated by experiments. LS-DYNA is a general-purpose finite element code for analysing the dynamic response of structures and, although an implicit solver is also available, it was developed primarily to simulate the effect of a load applied for only a short time. It uses an explicit time integration procedure, where the motion equation is written in the form representing the current time point and the required solution for the next time step is based on the consideration of the current time step equilibrium.

4.4.2 Concrete material model

There are many material models in LS-DYNA developed to simulate the response of concrete under impact loads. However, some do not include automatic parameter generation and excessive experimental testing is required to obtain all input data. Of those that can generate most parameters from unconfined compressive cylinder strength and which are suitable for both 3D and 2D analyses, Pseudo Tensor, Karagozian & Case (K&C) Concrete Model, Continuous Surface Cap Model (CSCM), and Riedel, Hiermaier, Thoma (RHT) Model are worth mentioning. CSCM model was specifically developed by the U.S. Department of Transportation to predict the dynamic performance—elastic deformation, as well as failure—of concrete used in roadside safety structures when involved in a collision with a motor vehicle [150] and was therefore considered in this study. The name of the model is derived from a multiplicative formulation combining the shear failure surface with the hardening compaction surface cap smoothly and continuously. The intersection of these two surfaces provides a yield surface of the defined material. The cap is included to simulate plastic volume change due to pore collapse. The cap itself is movable and its initial location defines the onset of plasticity in isotropic compression and uniaxial strain. It expands to simulate the plastic volume compaction and contracts to simulate the plastic volume expansion. The kinematic hardening is modelled with an initial shear yield surface which hardens until it coincides with the ultimate shear yield surface. Its initial location and hardening rate can be modified. The damage accumulation does not initiate on the cap where the plastic volume is decreasing but rather at the peak strength on the shear surface where the plastic volume is increasing. The initial damage threshold is coincident with the shear plasticity surface and can be delayed when rate effects are considered via viscoplasticity. With damage accumulation the viscoplastic stress tensor without damage is transformed into the stress tensor with damage. Two types of damage are included in the model. Brittle damage which is accumulated when the pressure is tensile and is not accumulated when the pressure is compressive and the ductile damage which is accumulated when the pressure is compressive and not accumulated in tension. The strain-softening is affected by both brittle and ductile damage. During the tensile softening the stiffness of concrete also degrades besides the reduction of the residual tensile strength. Accumulated strain in the material is partially reduced when unloaded. The size of this reduction corresponds to the ratio of the degraded modulus and the undamaged modulus. This phenomenon is generally known and was successfully implemented into the many concrete material models. In addition, the Continuous Surface Cap Model introduces a partial or full recovery of the modulus while the loading is switched from tension to compression. The unloading process is still affected by the degraded modulus but the degree of its recovery can be modified during the following compressive loading. To speed-up the computation and to maintain its stability, element

erosion is implemented in the model. The erosion criteria are defined by the amount of the damage accumulated and by the limit value of the maximum principal strain.

4.4.3 Numerical simulation of the full-scale impact test

Energy-absorbing system was modelled using Design Modeller implemented in ANSYS Workbench, as six adjacent plates with the same outer and inner dimensions as they had during the experiment. The impact cart was modelled as a rectangular plate with dimensions 5 mm × 1600 mm × 500 mm (height × width × thickness). The entire model was meshed with quadrilateral elements with a side length of 5 mm and exported to LS-DYNA format using ANSYS Mechanical. Although the experiment was symmetric with the axis of symmetry parallel to the direction of impact, it could not be modelled using half-symmetry. If so, the undamaged pieces of debris on the symmetry axis were not dislocated, leading to unrealistic model behaviour. The rigid construction behind the energy-absorbing system was simplified as a planar rigid wall and the impact cart was modelled as a plate with restricted rotations and movement permitted only in one direction. Its initial velocity and mass corresponded to the real-life experiment. Shell element formulation was set to option 13 to simulate the plain strain conditions. The impact cart could not be modelled as a moving rigid wall because its interaction with shell elements did not produce accurate results. Rigid material was assigned to the impacting plate with a density adjusted to simulate a mass of 1000 kg real impact cart. Automatically generated parameters based on the unconfined compression strength of concrete were used and supplemented with the default parameters given in the manual [150]. However, in order to achieve good agreement with experimental measurements, the stiffness recovery had to be extended from recovery based on volumetric strain to recovery based on both volumetric strain as well as on pressure. Even if this setting had an insignificant influence when the strain rate effects were turned off, it was necessary for further modifications. The rate effects were turned on because the effect of high-speed loading was monitored. The cap of the model was retracted to better simulate the compression of the resulting pieces of debris at the end of the calculation process. To avoid the decrease of the mass of the sample, erosion limit criteria were set very high, such that only highly distorted elements were removed from the calculation. This setting allowed to authentically simulate the deceleration of the impact cart due to aggregation of pieces of debris after the complete collapse of the cells. However, it also had a negative influence on the model behaviour when friction was considered. When considering friction, a positive effect was achieved during the collapse of the cells, however with elongation of elements, the friction surface increased unrealistically, and followed by excessive deceleration of the impact cart. To avoid this, static and kinetic friction coefficients were left on their default zero values. The input parameters of the CSCM model are shown in Table 4.3. To ensure the good interaction among the blocks and between the blocks and the impacting cart, the 2D automatic single surface contact was defined throughout the entire model. Flanagan-Belytschko hourglass stiffness form with a coefficient of 0.05 was used because this setting is preferred by many LS-DYNA users to simulate the automotive crash [151].

4.4.4 Numerical simulation of the reduced-scale impact test

The simulation settings of reduced-scale impact test were similar to that of the full-scale impact test. Because the calculation was considerably less time consuming, the model could be extended to a third dimension and the block of the energy-absorbing system was discretised with constant stress solid elements. Elements with a side length of 5 mm were used. The impactor was modelled as a movable rigid wall because its

Table 4.3: Input parameters of the CSCM_CONCRETE model used in 2D simulation. The International System of Units is used (SI units).

Mass density	RO	2245
Plotting option	NPLOT	1
Maximum strain increment for subincrementation	INCRE	blank
Rate effects option	IRATE	1
Erosion limit criterion	ERODE	3
Modulus recovery	RECOV	10
Cap retraction option	IRETRC	1
Pre-existing damage	PRED	0
Unconfined compression strength	FPC	85.456E6
Maximum aggregate size	DAGG	0.0012
Units used	UNITS	4

interaction with solid elements gave identical results as the solid to solid element contact and was slightly less time-consuming. Friction could be defined between the impactor and the specimen as well as between the resulting pieces of debris since the number of elongated elements was kept low. However, this change did not significantly affect the results and was only used to simulate the experimental conditions as realistic as possible. The input of the material model was taken from the simulation of the full-scale impact test. However, to match numerical outputs to experimental results, it was necessary to reduce the automatically generated fracture energy. The need for this change was expected because the Continuous Surface Cap Model was developed for concrete with normal strength and its parameters are fit to data for unconfined compression strengths between 20 MPa and 58 MPa and aggregate sizes between 8 mm and 32 mm [152]. The material employed in this study can be categorised as high-performance concrete with compressive strength above the limit and aggregate with a significantly lower diameter and as a result, exhibits a brittle failure with very low fracture energy. Fracture energy of high-performance concrete without reinforcement is often considered negligible and the reduction of the corresponding CSCM parameters was associated with a significant improvement in the model behaviour. The input values of fracture energies were adjusted to match numerical outputs to the results of the reduced-scale impact test as well as the quasi-static test. Recommended [150] mutual relationship of fracture energies was maintained. The compressive fracture energy was set to 100 times the shear fracture energy, which was set equal to the tensile fracture energy. The input parameters of the CSCM model are shown in Table 4.4, where IRATE=1.

4.4.5 Numerical simulation of the quasi-static test

Because the block was loaded in the direction parallel to its cells, the quasi-static test had to be modelled in three dimensions. The parameters of the CSCM model were taken from the simulation of the reduced-scale impact test. The block was discretised with constant stress solid elements with a side length of 5 mm and pressed by two rigid walls of circular shape with 400 mm diameter. One of the rigid walls was stationary and the other moved in the prescribed constant motion. Friction between the rigid walls and solid elements was considered. Although an implicit solver has already been implemented in the LS-DYNA, an explicit solver was used instead. This decision was made based on the fact that the CSCM model was primarily developed for use with the explicit method, and this method was also considered when presenting the quasi-static model response in the official CSCM manual [150]. Based on this manual, the hourglass coefficient was reduced

Table 4.4: Input parameters of the CSCM model used in 3D simulations. The International System of Units is used (SI units).

Mass density	RO	2245
Plotting option	NPLOT	1
Maximum strain increment for subincrementation	INCRE	blank
Rate effects option	IRATE	1 or 0
Erosion limit criterion	ERODE	3
Modulus recovery	RECOV	10
Cap retraction option	IRETRC	1
Pre-existing damage	PRED	0
Shear modulus	G	16.24E9
Bulk modulus	K	17.79E9
Tri-axial compression surface constant term	ALPHA	1.279E7
Tri-axial compression surface linear term	THETA	0.5117
Tri-axial compression surface nonlinear term	LAMDA	1.051E7
Tri-axial compression surface exponent	BETA	1.929E-8
Hardening initiation	NH	1
Hardening rate	CH	0
Torsion surface constant term	ALPHA1	0.7473
Torsion surface linear term	THETA1	-1.487E-9
Torsion surface nonlinear term	LAMBDA1	0.17
Torsion surface exponent	BETA1	-4.474E-8
Tri-axial extension surface constant term	ALPHA2	0.66
Tri-axial extension surface linear term	THETA2	-1.835E-9
Tri-axial extension surface nonlinear term	LAMBDA2	0.16
Tri-axial extension surface exponent	BETA2	-4.474E-8
Cap aspect ratio	R	5
Cap initial location	X0	1.426E+8
Maximum plastic volume compaction	W	0.05
Linear shape parameter	D1	2.5E-10
Quadratic shape parameter	D2	3.492E-19
Ductile shape softening parameter	B	100
Fracture energy in uniaxial stress	GFC	250
Brittle shape softening parameter	D	0.1
Fracture energy in uniaxial tension	GFT	2.5
Fracture energy in pure shear stress	GFS	2.5
Shear-to-compression transition parameter	PWRC	5
Shear-to-tension transition parameter	PWRT	1
Modify moderate pressure softening parameter	PMOD	0
Rate effects parameter for uniaxial compressive stress	ETA0C	9.669E-4
Rate effects power for uniaxial compressive stress	NC	0.78
Rate effects parameter for uniaxial tensile stress	ETA0T	1.625E-4
Rate effects power for uniaxial tensile stress	NT	0.48
Maximum overstress allowed in compression	OVERC	8.352E7
Maximum overstress allowed in tension	OVERT	8.352E7
Ratio of eff. shear stress to tensile stress fluidity parameters	SRATE	1
Power which increases fracture energy with rate effects	REP0W	1

to 0.01 to avoid excessive model stiffness. To reduce the computational time, only half of the block with symmetry conditions was utilised. The rate effects were turned off in CSCM settings. The input parameters of the CSCM model are shown in Table 4.4, where IRATE=0.

4.5 Results and discussion

4.5.1 Full-scale impact test

The EAS fracture process is shown in Figure 4.7 that consists of several shots from the high-speed camera during the first 100 ms after impact and depicts the fracture of the EAS internal structure (dissipation mode 1) and subsequent material accumulation (dissipation mode 2). The continuation of the collapse process is shown in Figure 4.8. At this stage, the cellular structure is completely disintegrated and the impact energy is absorbed only by the material accumulation (dissipation mode 2). The post-test state is in Figure 4.9.

Cart movement time history was based on the data obtained from the high-speed camera recordings that tracked the fiducial point at the nose of the impact cart. The distance travelled after the impact was determined at 10 ms intervals (Figure 4.10) and its time history was established as a fifth-order polynomial regression fit to the obtained points. Velocity (Figure 4.11) and deceleration time histories (Figure 4.12) were obtained as the first and second derivative of the proposed fifth-order polynomial, respectively. Deceleration of the impact cart was also measured by an accelerometer attached to its nose. Both deceleration curves showed a third-order polynomial trend, and their excellent agreement validates the results. The end of dissipation mode 1—observed at camera recordings and discussed above—is easily recognisable in the aforementioned graphs.

Using Newton's second law, a vector sum of the forces of the cart was determined as the mass of the cart (1000 kg) multiplied by its deceleration vector (Figure 4.13). The forces acting on the cart during the impact were up to 111kN and kept below the threshold at which the crumple zone of the vehicle is crumpled (Figure 4.14). Figure 4.14 shows the correlation between the force acting on the front of a vehicle and the deformation of an ordinary passenger vehicle.

The energy absorption was obtained by integrating the impact force from the distance (Figure 4.15). The specific energy absorption is defined as the energy absorption divided by the mass of the specimen (770 kg). The resulting specific energy absorption is presented in Figure 4.16 with regard to normalised distance as proposed by Chen et al. [42]. Normalised distance is the distance over the total length of the EAS (1500 mm).

The developed numerical model was able to replicate the gradual fracture process as well as the compaction of the resulted pieces of debris, i.e. both dissipation modes. Figures 4.17 and 4.18 compare the the time evolution of the impact cart movement and velocity, respectively, obtained experimentally and through numerical simulation. Figure 4.19 compares the gradual fracture process of the cellular structure obtained from the FE model and the high-speed camera. In this figure, the colour of the material is an indication of its damage, with red areas indicating completely damaged concrete. As can be seen, a very good agreement between experimental response and the numerical prediction was obtained. Thus it was validated that the developed numerical model is able not only to replicate the impact cart motion but also the gradual fracture process of the cellular structure and can be employed in future studies to clarify in more detail the effect of the geometric design on the response of EAS subjected to a vehicle impact.

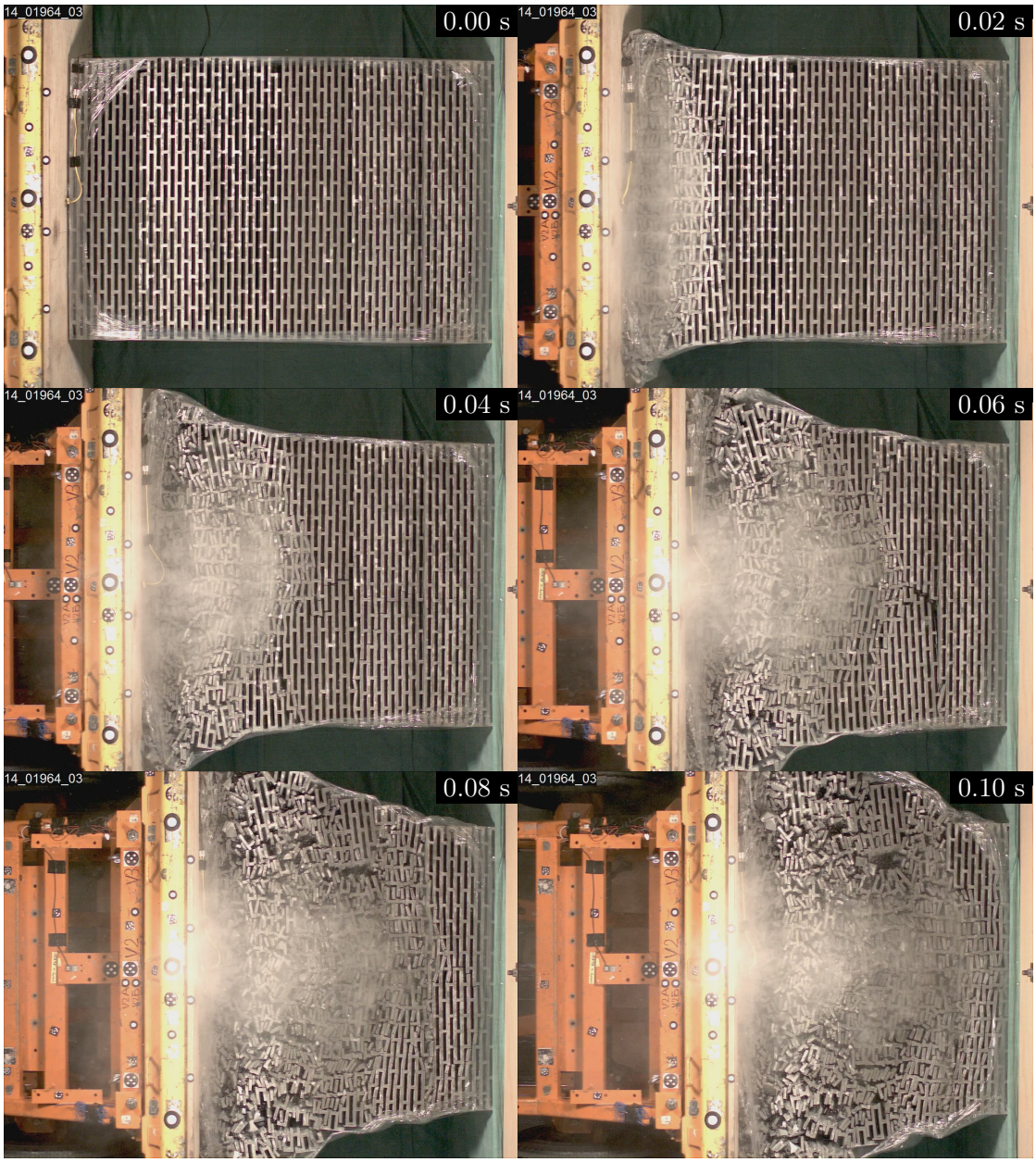

Figure 4.7: Time evolution of progressive collapse of the full-scale specimen in the time range 0-100 ms.

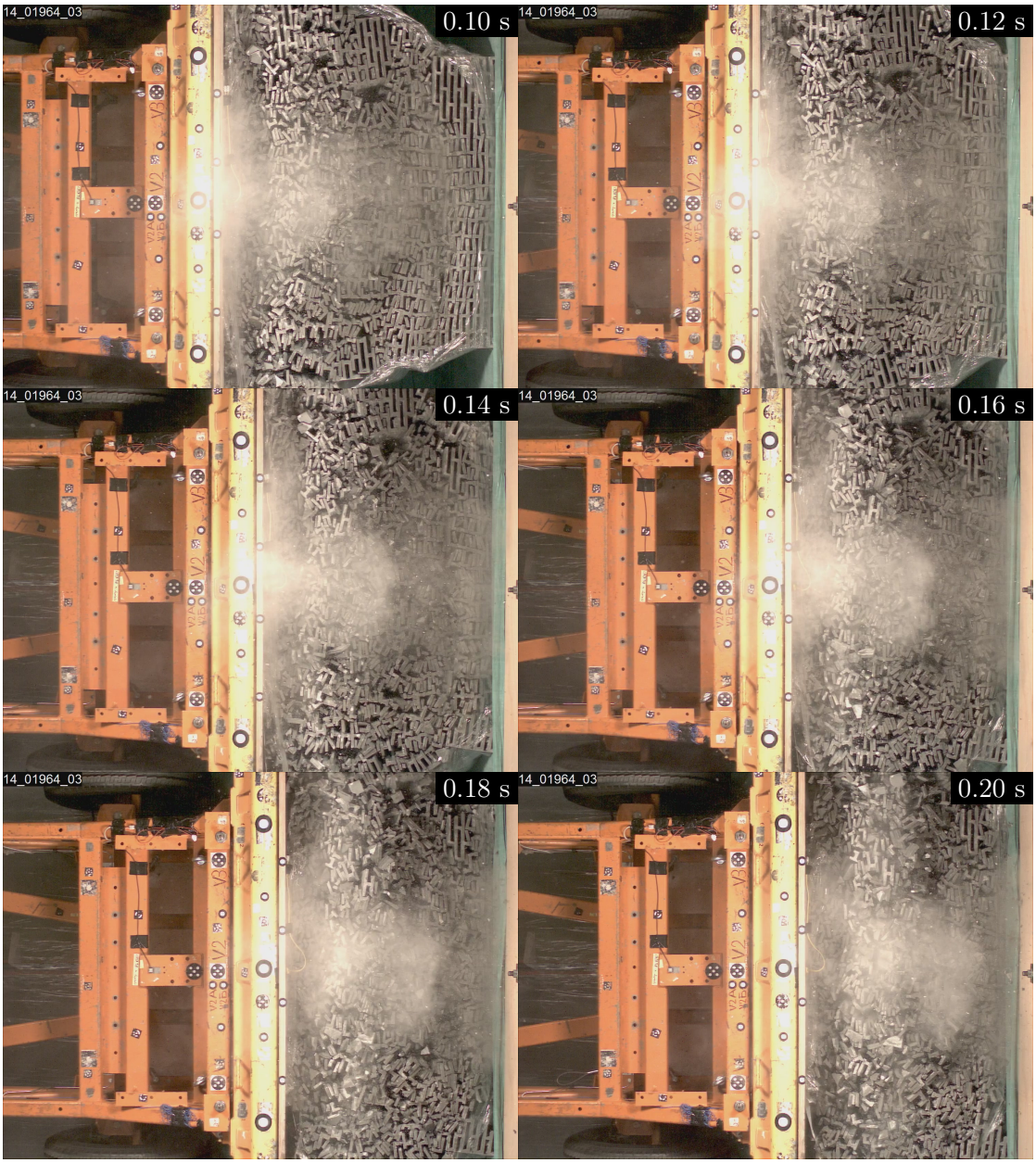

Figure 4.8: Time evolution of progressive collapse of the full-scale specimen in the time range 100-200 ms.

Figure 4.9: Post-test state of the full-scale specimen.

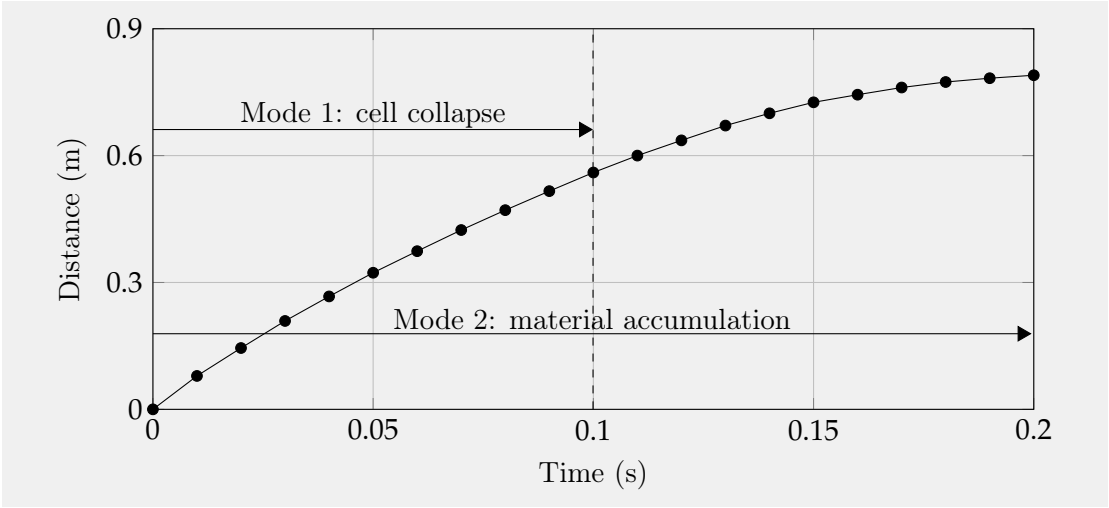

Figure 4.10: Time evolution of distance travelled by a non-deformable flat-nosed cart after crashing into a full-scale specimen.

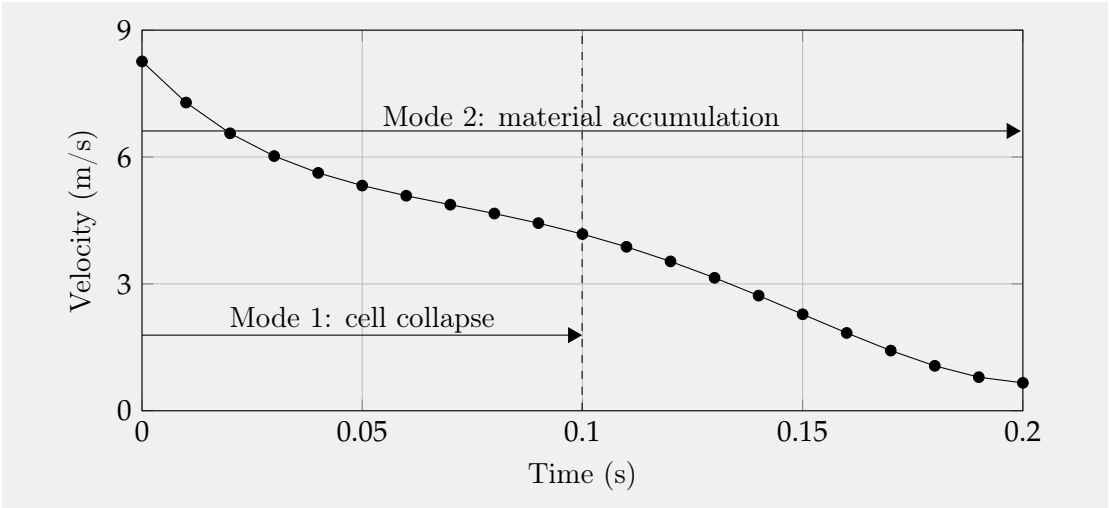

Figure 4.11: Time evolution of a non-deformable flat-nosed cart velocity after crashing into the full-scale specimen.

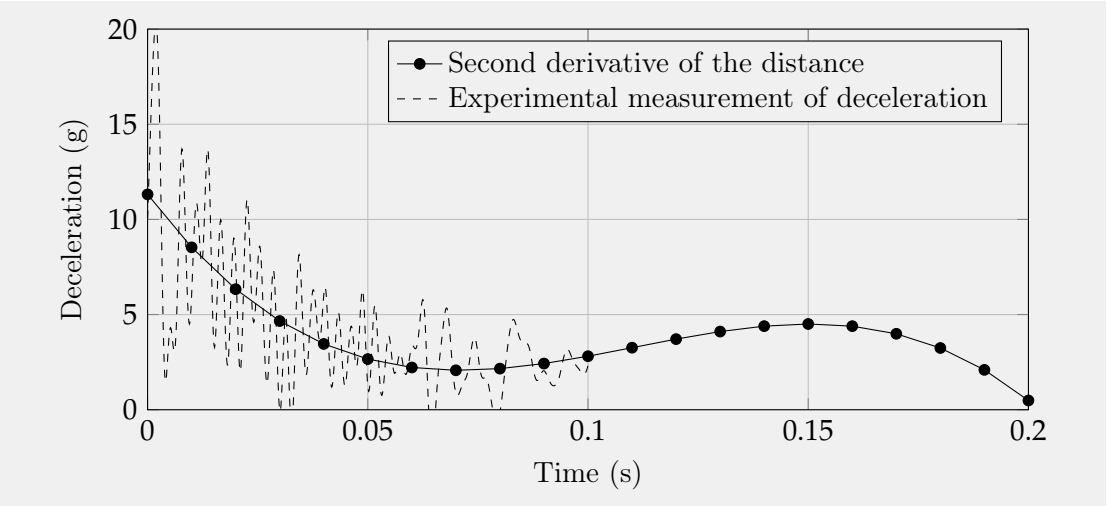

Figure 4.12: Time evolution of a non-deformable flat-nosed cart deceleration after crashing into the full-scale specimen.

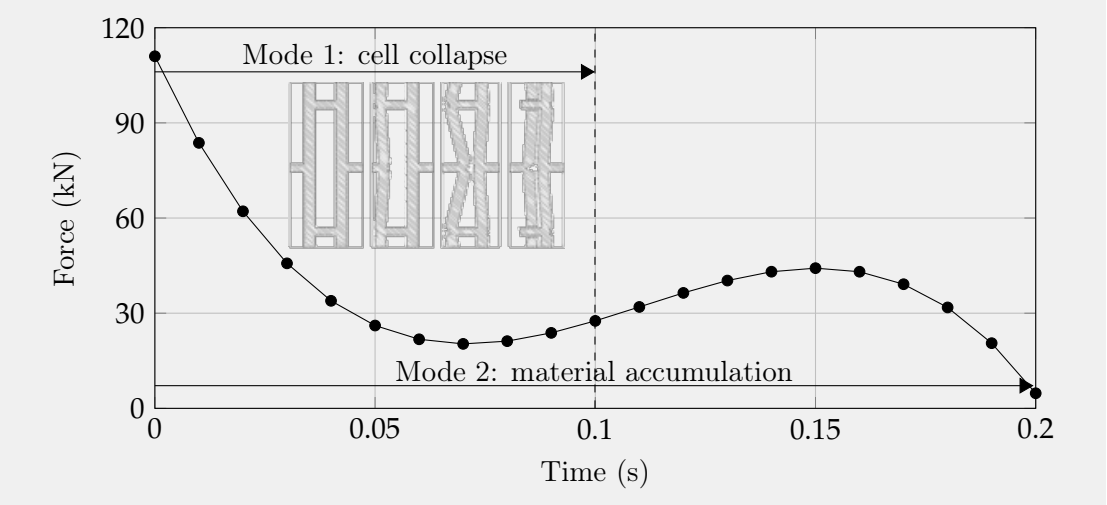

Figure 4.13: Time evolution of force acting on a non-deformable flat-nosed cart after crashing into the full-scale specimen.

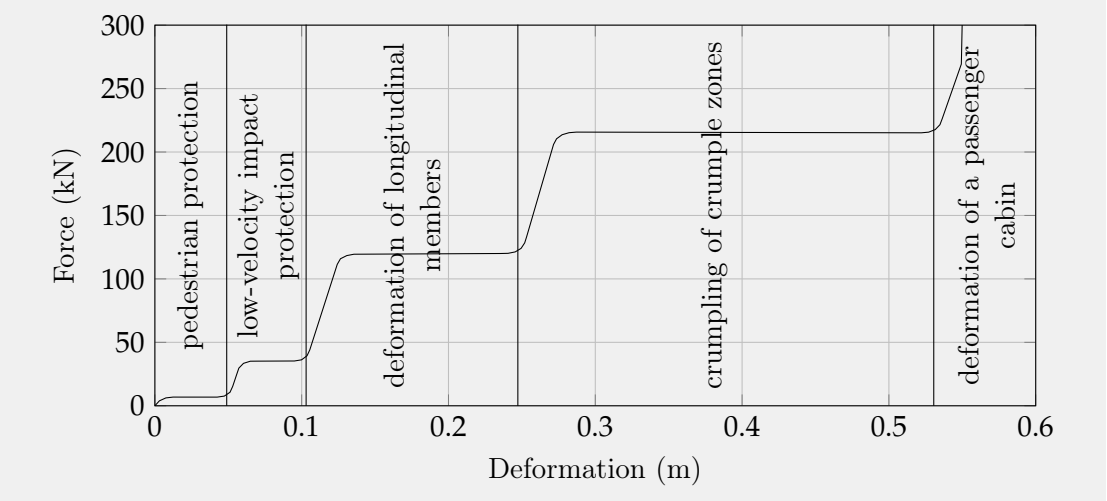

Figure 4.14: The correlation between the force acting on the front of a vehicle and the deformation of an ordinary passenger vehicle [69].

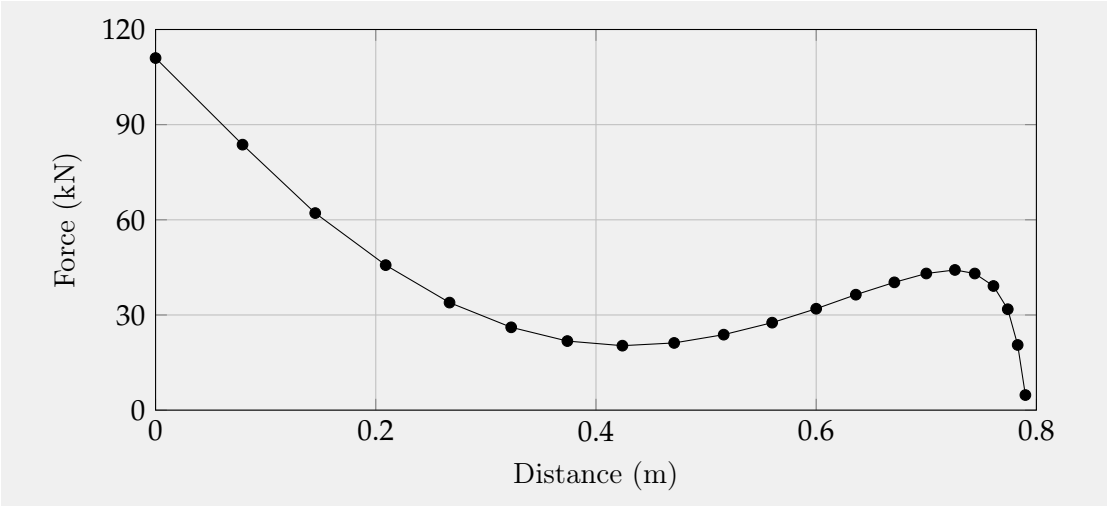

Figure 4.15: Force-distance curve used to evaluate energy absorption.

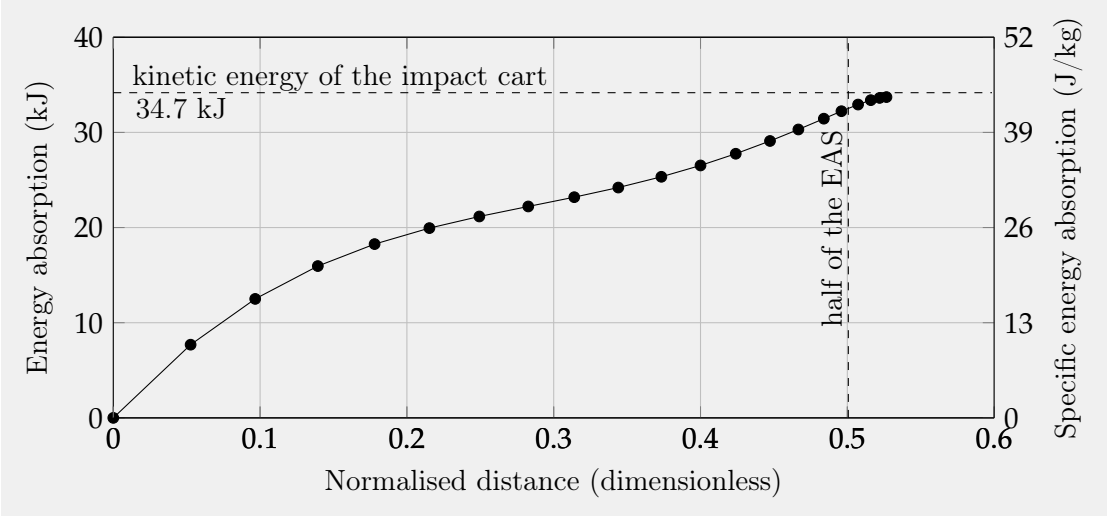

Figure 4.16: Energy absorption of the full-scale specimen impacted by a non-deformable flat-nosed cart.

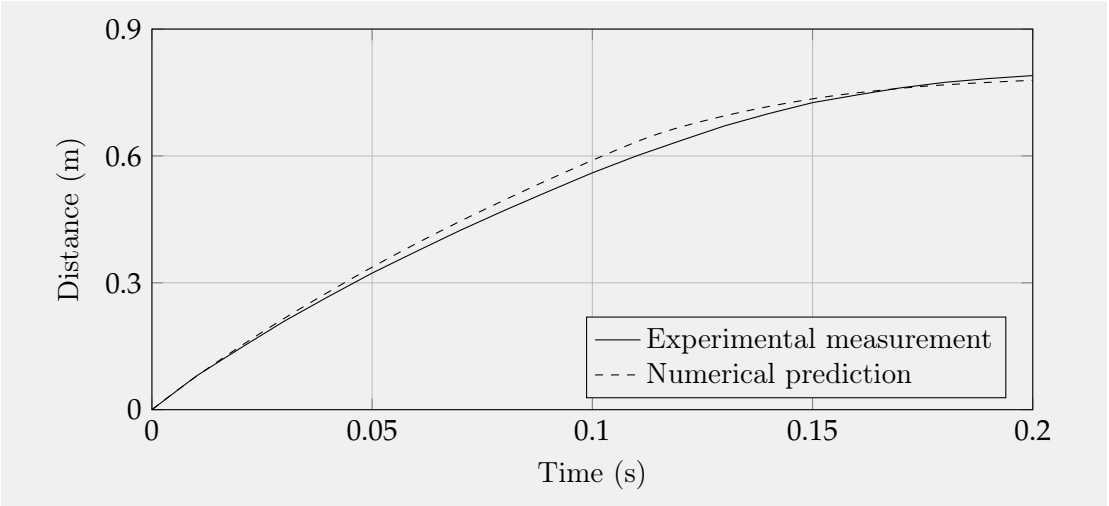

Figure 4.17: Time evolution of distances travelled by a non-deformable flat-nosed cart obtained experimentally after crashing into the full-scale specimen and through numerical simulation of the same experiment.

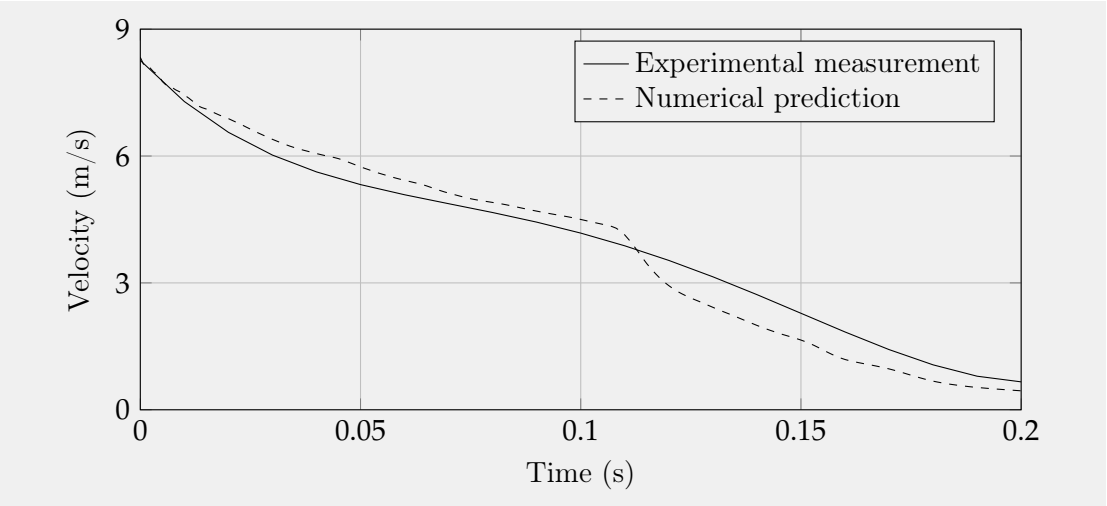

Figure 4.18: Time evolution of a non-deformable flat-nosed cart velocities obtained experimentally after crashing into the full-scale specimen and through numerical simulation of the same experiment.

4.5.2 Reduced-scale impact test

The EAS response during the reduced-scale impact test was similar to that of the full-scale impact test. During the reduced-scale test, time evolution for impactor motion and velocity after the first contact with specimen were obtained directly from the video recording device and can be seen in Figure 4.20 and 4.21, respectively. All five specimens showed very similar behaviour and the resulting response was determined by averaging the measured values.

Figure 4.22 shows the progressive collapse of the reduced-scale specimen. As with the full-scale test, two dissipation modes were observed. The two modes took place together up to 45 ms, and then, when the cellular structure collapsed completely, the dissipation mode 2, representing the accumulation of pieces of debris, took place separately. Due to the short length of specimens, the pieces of debris accumulated rapidly and the impactor stopped shortly after the end of the fracture process.

Experimental measurements were employed to validate the numerical model. A very good agreement of experimental and numerical methods was achieved for the collapse

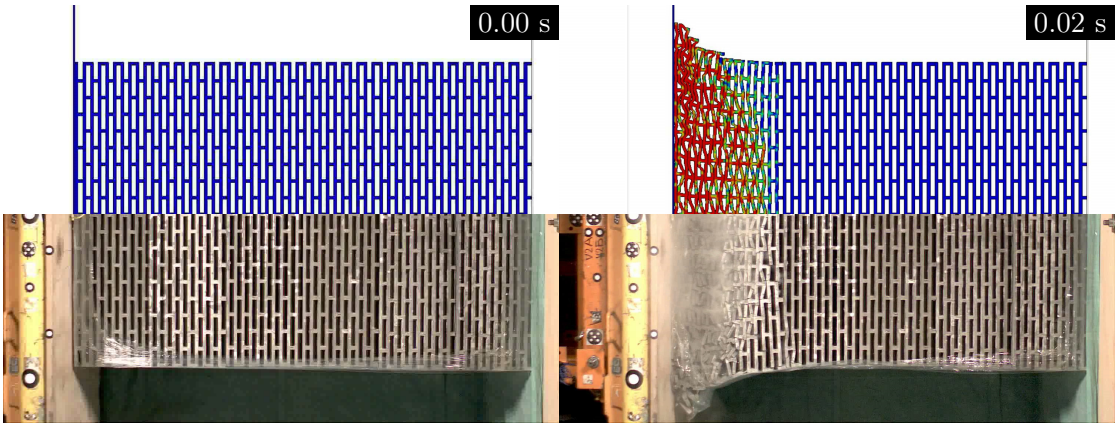

Figure 4.19: Progressive collapses of the full-scale specimen as recorded with a high-speed camera and predicted by numerical simulation.

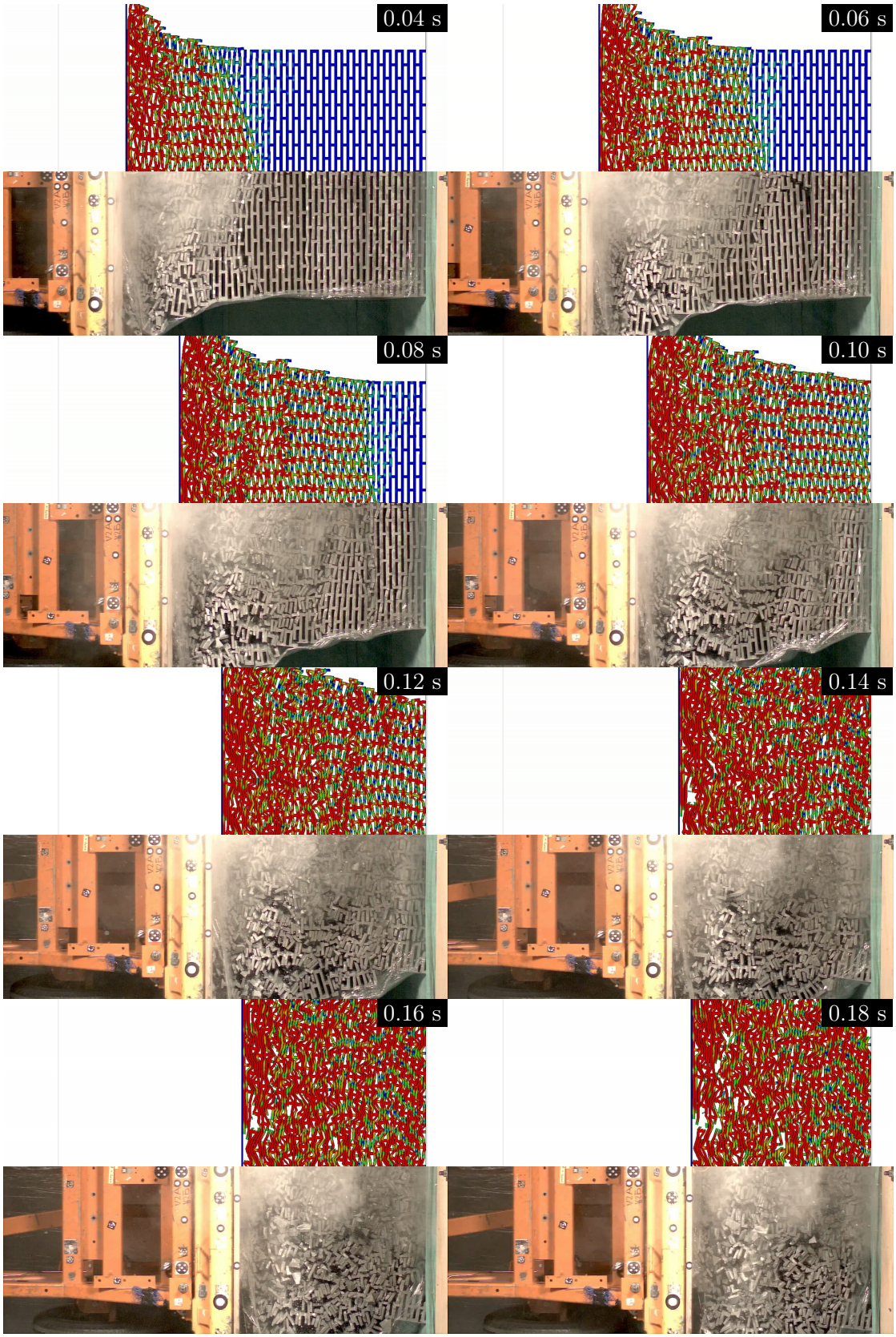

Figure 4.19: (continued)

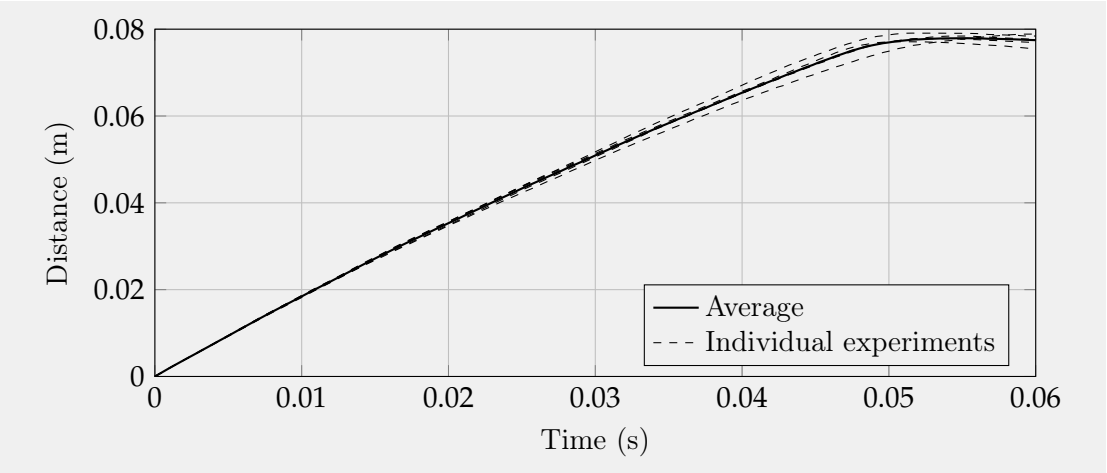

Figure 4.20: Time evolution of distance travelled by an impactor after crashing into the reduced-scale specimen.

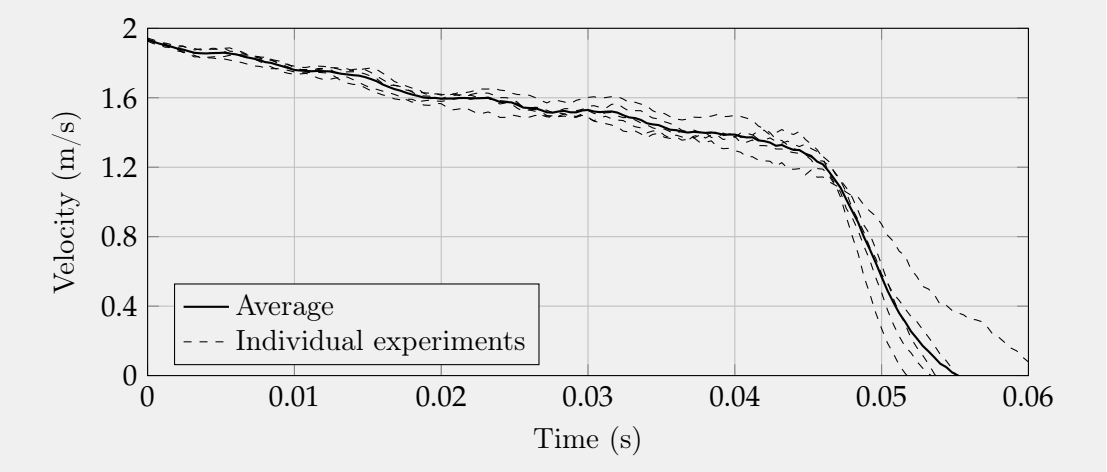

Figure 4.21: Time evolution of an impactor velocity after crashing into the reduced-scale specimen.

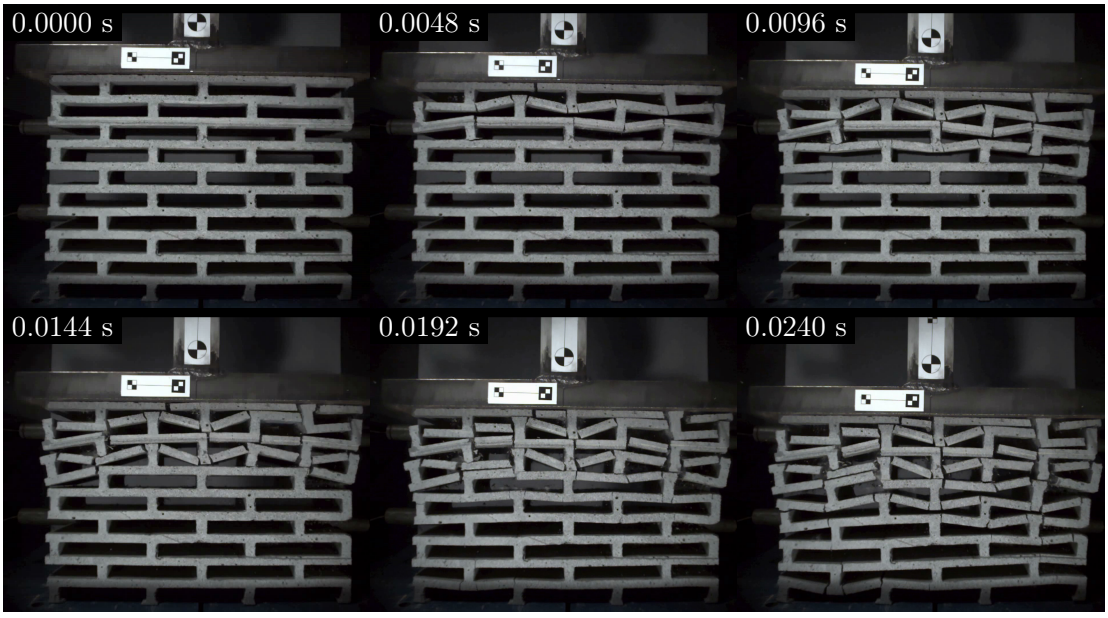

Figure 4.22: Progressive collapses of the reduced-scale specimen.

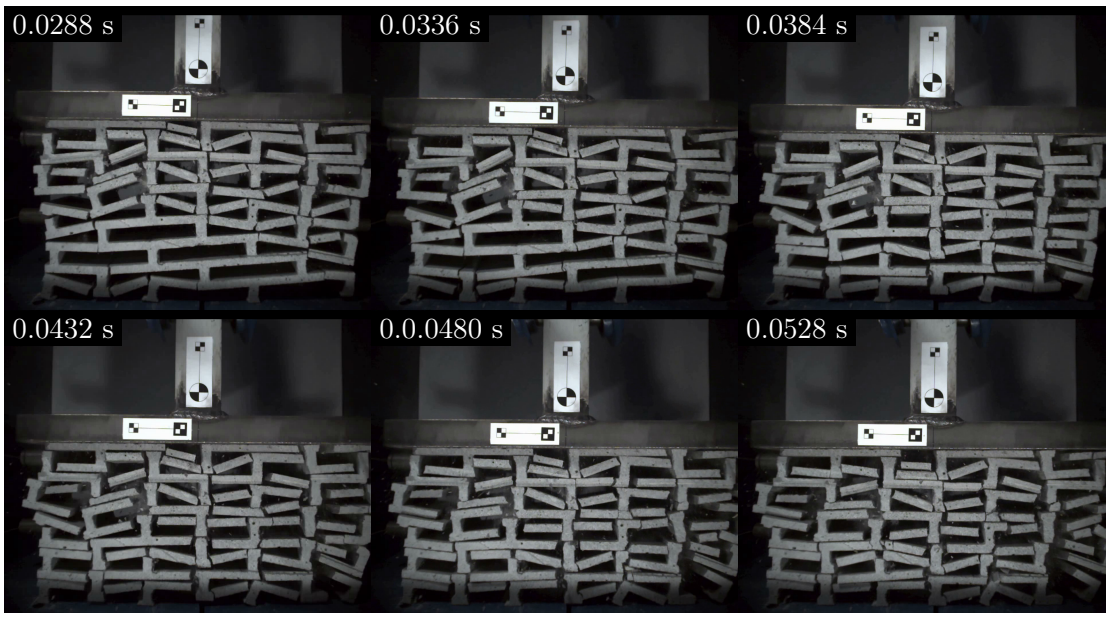

Figure 4.22: (continued)

process, as well as for the time evolution of motion and velocity, as seen in Figures 4.24, 4.25 and 4.23, respectively. The numerical model replicated the EAS response during both dissipation modes with very high accuracy, as well as the exact moment of the end of the dissipation mode 1.

4.5.3 Quasi-static test

A good agreement of numerical outputs with experimental results was also observed when evaluating the bearing capacity. The maximum compressive strength of one-third of the deformation block was determined experimentally (Figure 4.26a) at 21.0 MPa and numerically (Figure 4.26b) at 20.8 MPa. The standard deviation of the experimentally measured data was 1.1 MPa. Remarkably, after reaching the maximum compressive strength, instead of the brittle collapse of the block, a residual compressive strength of approximately 4 MPa was recorded (Figure 4.26c). It was not possible to accurately determine the residual compressive strength because only the applied force was recorded and the base area of the block changed with material crushing. The block was not crushed completely and the residual compressive strength was recorded for the remainder of the test until the maximum displacement of the moving part of the loading machine was reached. The determined maximum compressive strength of the EAS in the direction perpendicular to the expected impact can be compared with the compressive strength of conventional concrete and sufficient load-bearing capacity of the proposed EAS can be expected.

Both numerical simulations and experiments demonstrated that EAS presented in this paper meets all the required criteria. Although only a limited number of specimens were tested due to very expensive and time-consuming experiments, a similar specimen response and good agreement with the numerical predictions can confirm the accuracy of the results.

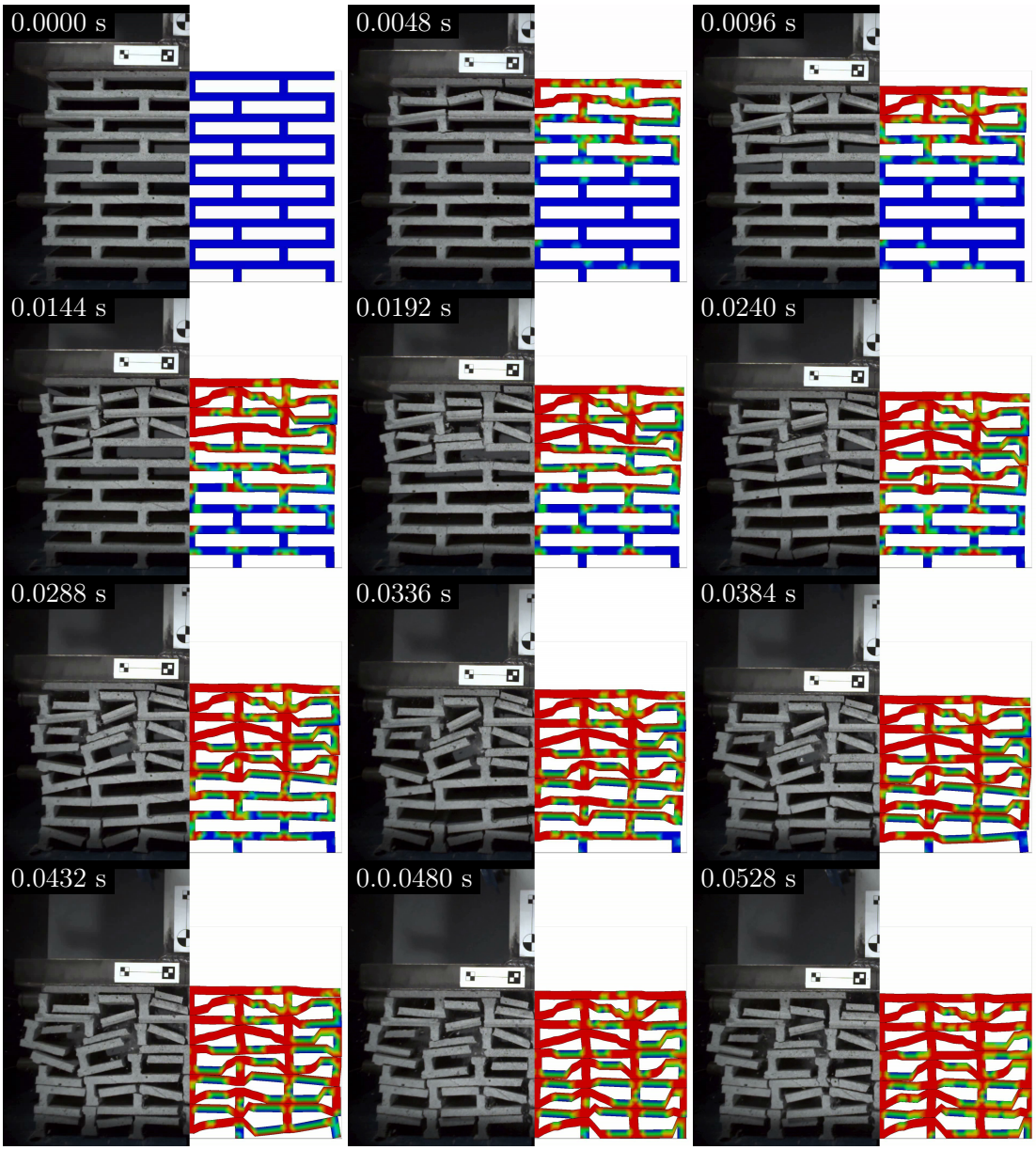

Figure 4.23: Progressive collapses of the reduced-scale specimen as recorded with a high-speed camera and predicted by numerical simulation.

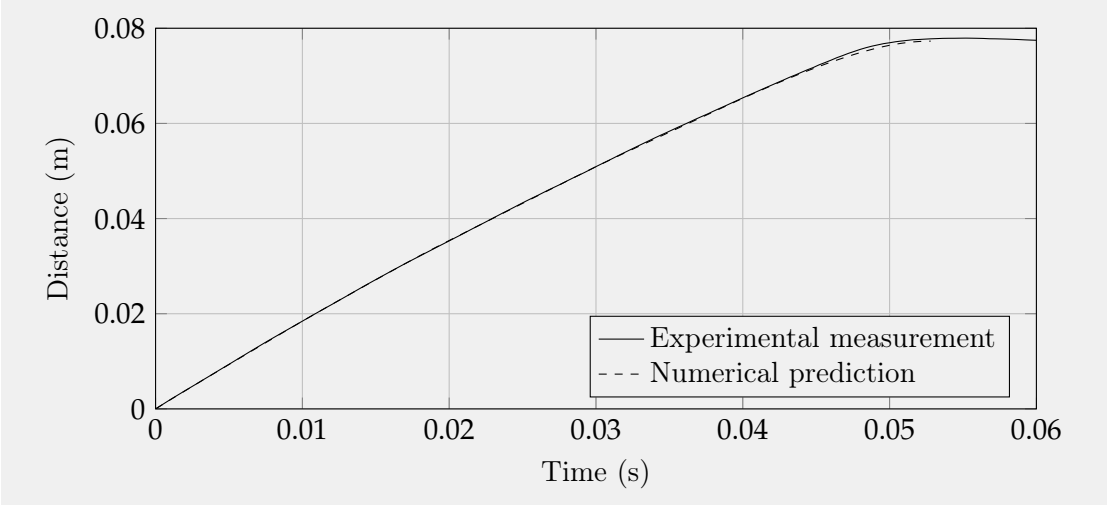

Figure 4.24: Time evolution of distances travelled by an impactor obtained experimentally after crashing into the reduced-scale specimen and through numerical simulation of the same experiment.

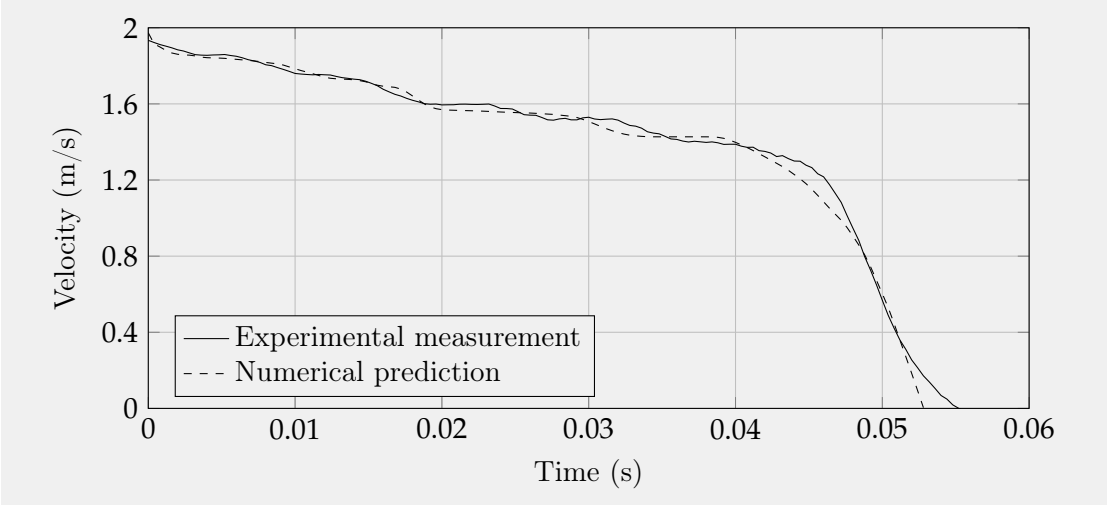

Figure 4.25: Time evolution of an impactor velocities obtained experimentally after crashing into the reduced-scale specimen and through numerical simulation of the same experiment.

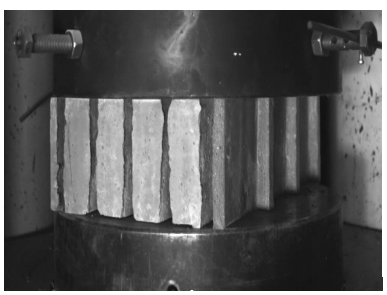

(a) At maximum compressive strength: Experiment.

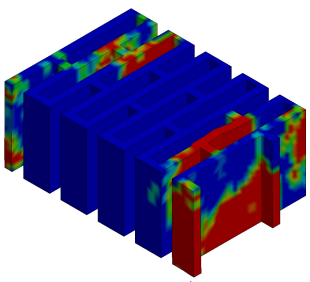

(b) At maximum compressive strength: Numerical prediction.

(c) At residual compressive strength: Experiment.

Figure 4.26: The reduced-scale specimen under quasi-static loading.

4.6 Conclusions and further outlook

The objective of the presented research was to develop the high-load-bearing energy-absorbing system (EAS) with enhanced environmental resistance and controlled deformation. The behaviour of EAS subjected to impact and quasi-static loads was investigated using experimental and numerical analyses. The following inferences can be drawn from the study:

1. It is possible to develop the EAS made of high-performance concrete with reasonable energy dissipation capacity.
2. At the same time, the EAS has sufficient load-bearing capacity in the direction perpendicular to the expected impact.
3. The forces acting on the vehicle during the collision with EAS were kept below the threshold at which the crumple zone of the vehicle is crumpled.
4. At the end of the energy absorption process, the impact vehicle had negligible residual velocity.
5. The energy absorption process can be divided into two dissipation modes: one represents the collapse of cellular structure and the other represents the subsequent material accumulation.
6. The developed numerical models were able not only to replicate the impactor motion but also both modes of energy absorption process in EAS. The numerical models can be used in future studies since they were validated with experimental data.
7. Due to the very expensive and time-consuming experimental procedures, only one type of cellular structure was investigated. Future studies will clarify in more detail the effect of the geometric design on the response of EAS subjected to a vehicle impact.

Chapter 5

Interpretation and outlook

5.1 Introduction

This thesis presents the design, production, and testing of an energy-absorbing system that dissipates the impact energy and has sufficient load-bearing capacity in the direction perpendicular to the expected impact. The developed EAS is also characterised by reasonable production cost, suitability for mass production, and for use in harsh environments. The thesis is a compendium of three full-length research articles that are interrelated by this chapter and supplement by Appendixes A and B. Chapters 2 and 3 presents an alpha version of the block that has fulfilled all the requirements with the exception of durability. Chapter 4 introduces a beta version where durability is provided by the use of high-performance concrete as the base material. A gamma version made of high-performance fibre-reinforced concrete is proposed at the end of this chapter. All three versions consist of blocks with cellular structures that absorb impact energy because of the gradual fracture process. The specifications of the developed energy-absorbing system allow for a wide range of applicability even in places where currently produced energy-absorbing systems cannot be installed and its use as a cushioning element in cross-drainage culverts could decrease transportation hazards.

5.2 Discussion

5.2.1 General remarks

Specimens of the alpha version were cut out of commercially available blocks made of fired clay. Only blocks' sides needed to be cut off to create a specimen consisting only of a cellular structure. This makes specimens easily and inexpensively obtainable in large quantities. However, given that the original blocks are not manufactured as cushioning elements but as thermal-insulating structural elements, the resulting specimens had many disadvantages. Their internal structure was slightly irregular by design and occasionally pre-cracks occurred. This weakened some cells and could cause an atypical collapse. The blocks are processed in two different manufacturing plants, as a result of which their mechanical characteristics also differed. Moreover, the blocks were not designed to be directly exposed to harsh environmental conditions and may therefore fail during the service life of a structure.

In order to increase durability, the beta version was made of high-performance concrete. However, this also led to an increase in the production price. The specimens were produced in the lab using a special mould and to prevent the cell wall collapse during demoulding, it was necessary to design thicker walls than those of the alpha version. Moreover, specimens had to be made from scratch, which slowed down their production

and reduced their availability. However, this shortcoming has now been almost eliminated thanks to cooperation with a private sector partner who is able to mass-produce the designed blocks.

5.2.2 Quasi-static load-bearing test

One of the requirements for the EAS is the sufficient load-bearing capacity in the direction perpendicular to the expected impact, which should be provided by the walls of the cellular structures. Both versions were tested using a hydraulic loading machine, which consists of stationary and movable parts. Alpha-version blocks are manufactured as structural elements and their load-bearing capacity is guaranteed by the manufacturer. To verify this data, but at the same time to maintain a reasonable time-consuming experimental work, only one type of block was tested. The experimentally determined load capacity was consistent with that stated by the manufacturer. Blocks of the beta version were also tested, but unfortunately due to the different sample sizes, it was not possible to compare the responses of the two versions. Taking into account the measured values, the higher compressive strength of the base material, and thicker cell walls, it could be assumed that the load-bearing capacity of the beta version will be higher. However, these assumptions have not been confirmed (but also not refuted) in this thesis. Nevertheless, the load-bearing capacity of both versions seems promising. Unfortunately, only reduced-scale specimens were tested in this thesis. The full-scale quasi-static load-bearing tests will be part of a larger experimental program involving samples made by the private sector partner.

5.2.3 Quasi-static energy-absorption test

Quasi-static energy-absorption tests were conducted only to examine the effect of a loading rate on the crashworthiness and crushing process of EAS. It was found, that in contrast to impact loading, the collapse of cellular structures subjected to quasi-static loading is irregular and progresses from their weakest part. Due to the imperfections of the cellular structures, the location of the weakest part was different for different samples tested and this resulted in a varying crushing process. The crushing forces developed during quasi-static loading were smaller, which resulted in the reduction of the risk of injury but also of the energy absorption capacity. This was most likely due to a different collapse mode and the negligibility of inertia and strain rate effects.

5.2.4 Reduced-scale impact test

To reduce the cost of the experimental program, part of impact tests was performed using reduced-scale specimens. The specimen was suspended to avoid friction at the vertical support, placed against a rigid support, and impacted by a flat-nosed impactor travelling in a circular trajectory and hitting the specimen at the bottom-return point. Unfortunately, during the beta version testing, only the movement of the impactor was tracked using fiducials and high-speed video, and its deceleration was not measured by accelerometers, which made it impossible to determine the indicators of crashworthiness. Thus, the EAS versions can only be compared based on the crushing process and the time evolution of impactor motion and velocity. However, even with these comparisons, caution is required due to the different sample sizes.

It is noteworthy that, in contrast to the collapse of the beta version, which progressed from the stricken end to the support, the progressive collapse of the alpha version at the stricken end stopped after some time, and then the collapse progressed from the

support. Since the progress of collapse from the support was also observed in the sample of the alpha version of the P15 type, which has the same cell shape as the beta version and similarly thick walls, the difference in the collapse of both versions could be due to different base material, a ratio of cell wall thickness to cell width, or sample dimensions. Effect of these parameters on the crushing process should be investigated in future studies.

The impactor velocity time histories were used to determine the kinetic energy evolution of the impactor:

$$E_k = \frac{1}{2} m_0 v^2 \tag{5.1}$$

where m_0 is the mass of the impactor and v is its velocity. The evolution of the kinetic energies of the impactor after crashing into various samples is plotted in Figure 5.1 as a function of a crushing stroke. The rate of loss of kinetic energy of the impactor is more pronounced within the alpha version blocks for samples of type F30 and F44 and even more so for type P15. This corresponds to their increased average force. The increase in the average force is associated with an increase in energy absorption capacity, but also with an increase in the risk of injury. The increased the average force of samples F30 and F44 was linked in Chapter 3 to the shorter cell width and their larger number across the width of the sample. The even more increased the average force of sample P15 was linked in Appendix A to even shorter cell width, a larger number of cells across the sample width, but also to a thicker cell wall. The rate of loss of kinetic energy of the impactor recorded during the collision with the beta version sample was similar to the rate recorded for the collision with the P15 alpha version sample. This similarity is probably due to the similar thickness of their cell walls and the fact that the strength of sample P15, which can be attributed to the narrower cells and their increased number across the sample width, was compensated by the increased strength of the base material of the beta version. In contrast to the collapse of sample P15, at the end of the absorption process of the beta version, there was a rapid decrease in the kinetic energy of the impactor with a relatively small increase in crushing stroke. This was due to the fact that the beta version sample was shorter and during its collapse the pieces of debris broken off of the cellular structure were accumulated and compacted between the impactor and the fixed support, while the longer sample P15 absorbed all of the kinetic energy of the impactor before the pieces of debris could be compacted.

To compare samples length utilisation, $u_{\max}$ had to be used instead of u_{eff}, which could not be determined for the sample of the beta version, because the data needed to plot the sample's force-displacement curve were not recorded. Therefore, Equation 3.10 was modified as follows:

$$CE_{\max} = \frac{u_{\max}}{L} \tag{5.2}$$

where L is the sample length. The $CE_{\max}$ values of the compared samples are given in Table 5.1. Sample P15 was excluded from this comparison because its $u_{\max}$ was not reached during the test. $CE_{\max}$ of the beta version was lower than $CE_{\max}$ of any sample of the alpha version. This was most likely due to the cellular structure of the beta version, which contained cell walls parallel to the direction of impact. These walls accumulated during the collapse between the impactor and the support and subsequently stopped the impactor (Figure 4.22).

5.2.5 Full-scale impact test

Samples of both versions in full-scale were subjected to the impact of a flat-nosed impact cart. The beta version was placed against a rigid wall. A semi-stiff part was placed between the alpha version and a rigid wall.

The evolution of the kinetic energy of the impact cart after crashing into the alpha or the beta version of EAS is plotted in Figure 5.2 as a function of the crushing stroke. The kinetic energy of the impactor is in the early phase of crushing absorbed by the beta version at a higher rate than by the alpha version. This is consistent with the conclusion drawn in Appendix B that the initial ASI values (and therefore the crushing force) of the beta version are higher than those of the alpha version, which was attributed to the greater strength of the base material and a thicker cell wall. The impactor was crushing the cells of the beta version on a shorter stroke than those of the alpha version. This was most likely due to earlier material accumulation of pieces of debris as described in the previous section. The pieces of debris of the alpha version were compacted on a shorter stroke than those of the beta version. This is consistent with the higher second ASI peak of the alpha version (Figure B.3). Both versions are comparable in collision severity and the corresponding occupant injury potential was assessed as low.

In Chapters 2 and 4, it was stated that during the deformation process of the full-scale cellular structure, in addition to the cell crushing, there is also an accumulation of pieces of debris between the impact cart and the support. Based on the more detailed observations made in Chapter 3, the material accumulation mode can be further subdivided into the relocation of pieces of debris and their subsequent compaction. It can be summarised that the energy absorption process under impact loading consists of three main components: cell crushing, acceleration of the pieces of debris broken off of the cellular structure, and compaction of the pieces of debris.

5.2.6 Full-scale car crash test

EAS was built into a cross-drainage culvert embedded in the ground and subjected to the impact of an ordinary passenger vehicle to demonstrate that the damaging consequences of a collision with culverts could be significantly reduced by building culverts using blocks of EAS. In contrast to frontal impact with the rigid wall, impact with the EAS allowed intact parts of the vehicle to decelerate to zero for more than a three times as large area and for a more than four times as long time. Vehicular crumple zones were not even crumpled during the collision with EAS, vehicle bounce off was eliminated, and gradual deceleration of the vehicle was recorded. Even when the airbags were deactivated, the driver dummy did not even touch the steering wheel. The acceleration severity index was 3.5 times lower and kept below its strictest threshold, thus the risk of passenger injury was significantly reduced and is considered very low. In this thesis, only the alpha version was tested, the specimens of which were cheaply and easily available. The response of the beta version on the impact of a passenger vehicle will be examined in a larger experimental program involving samples made by the private sector partner.

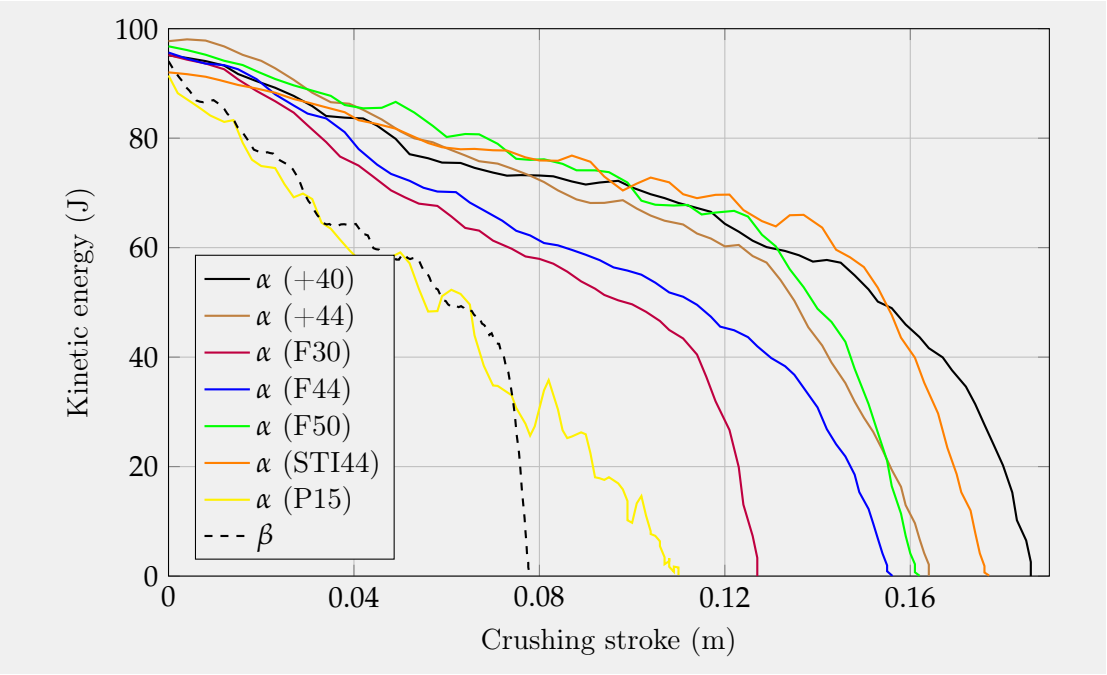

Figure 5.1: The evolution of the kinetic energy of the impactor with respect to the crushing stroke after crashing into various samples.

Table 5.1: Maximum crush efficiency.

α (+40)	α (+44)	α (F30)	α (F44)	α (F50)	α (STI44)	β
0.578	0.524	0.499	0.503	0.535	0.584	0.314

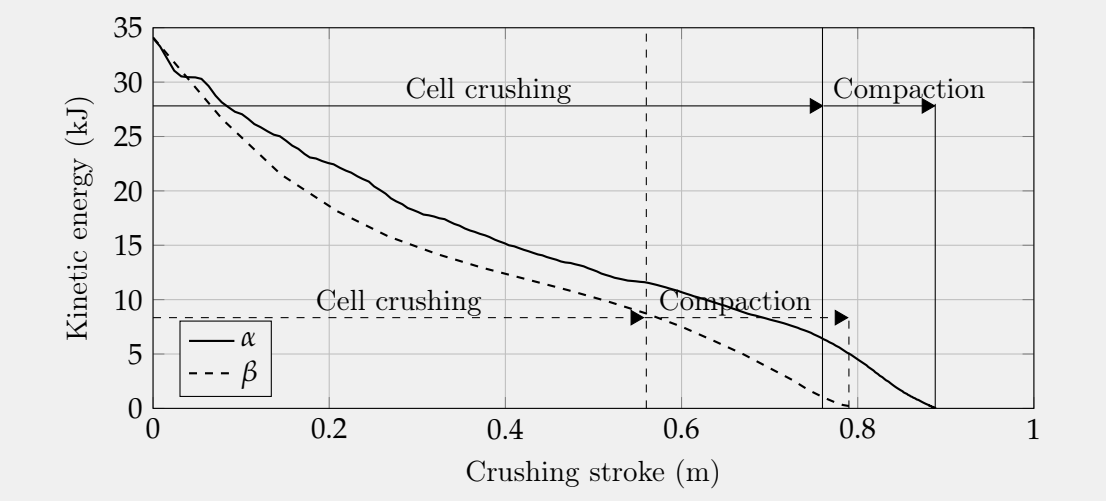

Figure 5.2: The evolution of the kinetic energy of the impact cart with respect to the crushing stroke after crashing into the alpha or the beta version of EAS.

5.3 Conclusions

Within this thesis, the high-load-bearing energy-absorbing system with controlled deformation was developed. To my best knowledge, the presented data is the first of its kind. The following inferences can be drawn from the thesis:

1. Blocks tested here were able to absorb impact energy because of the gradual brittle fracture process in their cellular structures.
2. Blocks exhibit different levels of crashworthiness at different loading rates.
3. Relatively small changes in the design of cellular structure can lead to the production of blocks with distinguishable levels of crashworthiness.
4. Energy-absorbing system can be modified, by composing it of blocks with different levels of crashworthiness, to gradually absorb different levels of impact energy and to decrease the collision severity.
5. The energy-absorbing system can be cast form high-performance concrete, which makes it suitable for use in harsh environments while still having reasonable production costs and the ability to be mass-produced.
6. The energy absorption process under impact loading consists of three main components: cell crushing, acceleration of the pieces of debris broken off of the cellular structure, and compaction of the pieces of debris.
7. The developed numerical models can be used in future studies since they were validated with experimental data. They are able not only to replicate the impactor motion but also all components of energy absorption process in EAS.
8. The damaging consequences of passenger vehicle collisions with cross-drainage culverts could be significantly reduced by replacing stones and solid blocks in cross-drainage culverts by the developed EAS as cushioning element.
9. The forces acting on the vehicle during the collision with EAS were kept below the threshold at which the crumple zone of the vehicle is crumpled.
10. In contrast to the collision with the non-deformable culvert, while impacting the culvert composed of the EAS as cushioning element, the acceleration severity index was 3.5 times lower and kept below its strictest threshold, thus the risk of passenger injury was significantly reduced and is considered very low.
11. Vehicle bounce off was eliminated during the collision with EAS, gradual deceleration of the vehicle was recorded, and the driver dummy did not even touch the steering wheel, even if the airbags were turned off.
12. The specifications of the developed EAS allow for a wide range of applicability even in places where currently produced energy-absorbing systems cannot be installed.
13. This thesis has additionally laid the cornerstone for cooperating with a private sector partner. The cooperation has been established in the area of product development and manufacture and is supported by the Technology Agency of the Czech Republic [grant number TH04010066].

5.4 Suggestions for future research

- Inferences drawn from this thesis help in collaborating on the production of a prototype with the private sector and the final product can be tested using the methodology developed here. At the same time, however, it is still necessary to address a lot of issues such as transport and installation of blocks on site, or the final overall design of the cross-drainage culvert.
- A follow-up study could further explore the crushing process of a cellular structure subjected to impact loading and determine the effect of support on a collapse mode. Impact test setup from Section 3.2.2.2.2 could be modified by relocating the support and forming a gap between the support and the specimen, which would eliminate the effect of support on the specimen in the early stages of collapse and thus the interaction of the incident and reflected stress waves from the supported end, which was reported by Zou et al. [58]. One of the main goals of the study would be to determine whether the collapse of the cellular structure progresses from the support as a result of these waves, or as a result of the specimen gaining the velocity from the impactor and colliding with the support. The pattern could be sprayed on the specimen and the wave propagation could be monitored by photogrammetry and compared with the response of the supported specimen. Studies on the propagation of stress waves through cellular structure and its effect on the collapse mode have already been published (e.g. [58, 60, 153]), however, they utilised only a supported specimen. Hu and Yu in [61] simulated the impact of the sample into the support, but as the authors of the previously mentioned studies, they used only numerical methods and ductile materials.
- Another subsequent study could be devoted to the study of the combination of samples with different crashworthiness measures. It was concluded in Chapter 3 that it is possible to design a specimen composed of brittle blocks with cellular structures able to gradually absorb different levels of impact energy by combining elements of different stiffness. It was also suggested in Appendix B that the collision severity could be reduced by placing a stiffer element behind the softer one. A deeper understanding of this topic would be beneficial to design crash cushions able to absorb the impacts of vehicles with different mass and impact velocity and could lead to further reduction of passenger injury potential. Blocks with different levels of crashworthiness identified in Chapter 3 and Appendix A could be used for this study. Namely, the samples cut out of manufactured blocks HELUZ STI 44, HELUZ PLUS 40, and HELUZ P15 30 could be considered as soft, semi-soft, and semi-stiff elements, respectively. These blocks are manufactured structural elements, making them easily and inexpensively obtainable in large quantities. Density graded cellular structures have already been studied by Ajdari et al. [62] and Zheng et al. [63]. However, they used only numerical methods and elastic perfectly-plastic materials. The proposed study would experimentally describe the behaviour of functionally graded brittle cellular structures subjected to impact loading and their response under different levels of impact energy. Thanks to the three identified blocks with distinguishable levels of crashworthiness, several variations of specimens with adjustable lengths and with increasing, decreasing, or variable gradients are available.
- The aforementioned study could be supplement by the finite element study utilising the numerical models developed in Chapter 4. In addition to the effects of length and density gradient, the proposed parametric study would also examine

the effect of the shape of cells, cell volume fraction, cell wall thickness, and a wide range of impact velocities. Instead of validating numerical models against the experimental data presented in Chapter 4, a sensitivity study on the stability of the computational model, identification of important parameters, and recalculation with different material models could be added to make simulations more reliable and provide additional insights into structural performance of *EAS*. In the related published articles, responses of ductile metallic cellular structures (in [53, 56, 57]) simulated by elastic perfectly-plastic material model (in [56–58, 60–62]) are usually studied. The proposed study would describe the behaviour of cellular structures made of high-performance concrete and simulated by advanced material models. Moreover, the majority of published works (e.g. [56–58, 61, 62]) on the impact response of cellular structures includes constant crushing velocity. However, this condition is close to reality only when the impact mass is sufficiently large compared to the mass of the cellular structure [61]. Even though some works [61, 62] also studied the effect of non-constant crushing velocity, the results were discussed only marginally. In the proposed study, the initial kinetic energy of the impact mass does not remain constant and is dissipated by a gradual fracture process in the brittle cellular structure.

- The further study could be devoted to the development of the gamma version of the energy absorbing system, which would be made of high-performance fibre-reinforced concrete. The main objective would be to develop a concrete mixture containing fibres, which would give the *EAS* ductility and thus an increased energy absorption ability, but at the same time, there would be no or negligible increase in strength associated with increased injury potential. The final crashworthiness design of the block could follow the observations made in previous studies and, as a result, the next generation of high-load energy-absorbing system would be developed.

Appendix A

The crashworthiness of brittle blocks with rectangular and hexagonal cellular structures made of fired clay

A.1 Introduction

This Appendix complements the comparative study contained in Chapter 3 and proves the robustness of the assessment methodology introduced in it. Two additional blocks with different cellular structures made of fired clay are subjected to impact tests: one consists of rectangular cells and the other is composed of rectangular and hexagonal cells. These specimens were excluded from Chapter 3 due to their undesirable behaviour when subjected to impact load. Their crushing process, force-displacement curves, and a wide range of indicators of crashworthiness are examined and their shortcomings are discussed.

A.2 Methodology

Both tested specimens P15 and MK (Figure A.1) were obtained by trimming the commercially available fired clay blocks HELUZ P15 30 and HELUZ AKU MK 36.5. The longitudinal sides of both types of blocks were trimmed to eliminate tongue and groove joints. Moreover, the transverse sides of block type HELUZ AKU MK 36.5 had to be trimmed to obtain regular cellular structure. After trimming, none of the examined cellular structures contained any walls which could brace during loading. Specimen P15 consists of rectangular cells and MK is composed of rectangular and hexagonal cells. The cells are distributed regularly; each row is offset by half the cell spacing. The shapes of cells are depicted in Figure A.2 and the corresponding dimensions are listed in Table A.1. Thickness of all samples were approximately 100 mm. The test setup and assessment methodology are the same as in Chapter 3 and are, therefore, omitted for the sake of brevity.

A.3 Results

Tests were conducted at least six times, each under identical test conditions to determine mean values of indicators of crashworthiness with acceptable standard deviations. The exact number of tests conducted is listed in Table A.2.

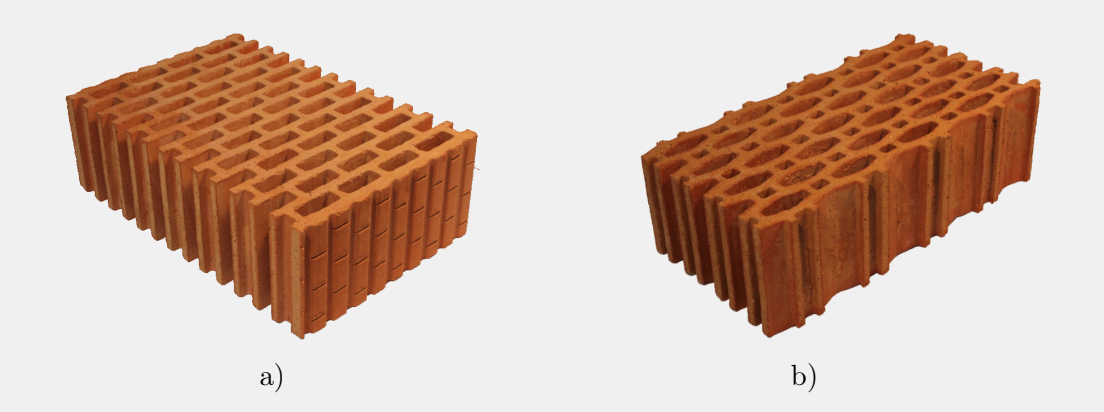

Figure A.1: Tested ceramic specimens cut out of fired clay blocks: a) P15; b) MK.

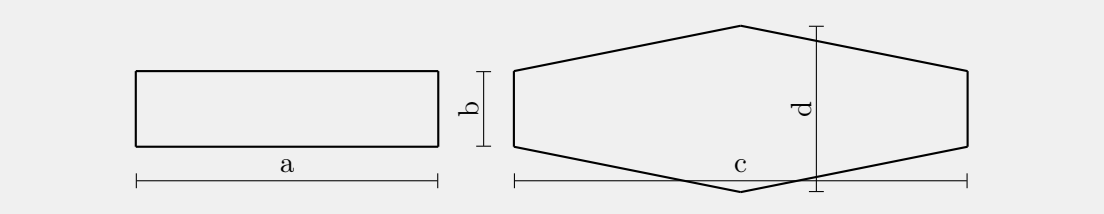

Figure A.2: Sketches of cells with dimension lines.

Table A.1: Weight and dimensions of specimens tested.

		P15	MK
Block mass	m (kg)	4.84	4.96
Block volume	V (dm^3)	6.45	5.61
Block width	W (mm)	215	330
Block length	L (mm)	300	170
Rectangular cell width	a (mm)	33.5	12.1
Rectangular cell length	b (mm)	13.1	7.5
Hexagonal cell width	c (mm)	-	41.4
Hexagonal cell length	d (mm)	-	14.3
Cell wall thickness	t (mm)	9.4	10.8

Table A.2: The number of tests conducted.

Specimen	P15	MK
Number of tests	8	6

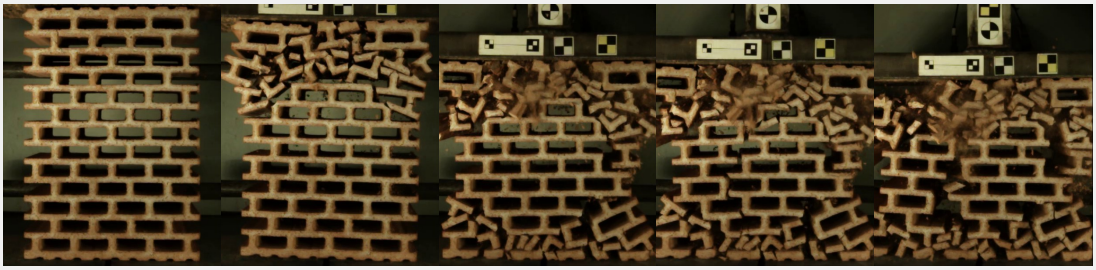

(a) Block P15 before the test. (b) The ∧ band at stricken end. (c) The ∨ band at supported end. (d) The longitudinal crack. (e) Maximum crushing stroke.

Figure A.3: Different stages of the collapse of specimen P15.

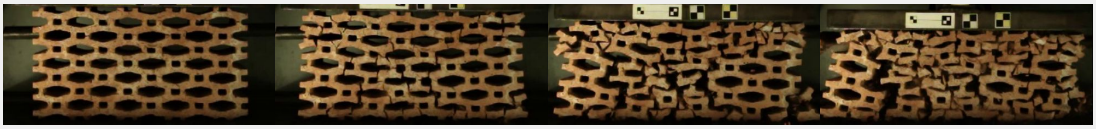

(a) Block MK before the test. (b) The X band across the block. (c) Cell fracture at both ends. (d) Maximum crushing stroke.

Figure A.4: Different stages of the collapse of specimen MK.

A.3.1 Crushing process

Several stages of the crushing process of block P15 shown in Figure A.3 resembled those described in Section 3.3.1. When the impactor comes into contact with a sample, the cells at the stricken end fracture. Unlike the blocks with thin-walled diamond-like cells examined in Chapter 3, where the collapse progressed from the impactor until the crushing band ∧ was formed, the crushing band is formed immediately and the cells between the crushing band and the impactor are not crushed A.3b). This is probably associated with a small ratio of cell wall thickness to cell width, leading to higher stiffness of the cellular structure. During half of the experiments, the crushing band ∨ was formed instead of the ∧ band. This variation was likely due to the imperfections of the cellular structures mentioned in Section 3.2.2.1 or the imperfect contact between the impactor and the specimen. Unfortunately, it was not possible to ensure that the impactor impacted the sample at an ideal perpendicular angle. In contrast to the crushing process in Section 3.3.1, the crushing band does not progress. In most cases, a longitudinal crack propagates through the sample from the impactor to the support. This may be due to the imperfections and weakening of the cellular structure. Similar to stage 3 of the crushing process described in Section 3.3.1, the cells at the supported end fracture (Figure A.3c). If the single crack does not propagate through the sample, the cells at the supported end will fracture anyway and a longitudinal crack will form later (Figure A.3d). The longitudinal crack divides the sample into two parts, which are pushed aside. The impact energy is fully absorbed by the sample and the remaining parts of the sample are not crushed (Figure A.3e).

Stages of the crushing process of block MK are shown in Figure A.4. The crushing band X is formed across the entire sample immediately upon contact with the impactor, dividing the sample into 4 parts (Figure A.4b). This is most likely associated with a very large block width to length ratio and increased block stiffness. In the next phase of the collapse process, the parts adjacent to the impactor and the support are crushed (Figure A.4c). The order of crush of parts at the stricken end or the supported end appeared to be random. More tests would be needed to determine the most likely order

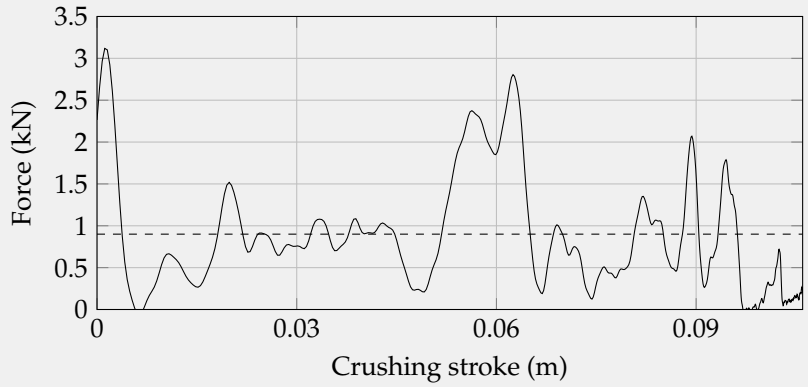

Figure A.5: Force-crushing stroke curves of the tested specimen P15. Dashed line represents the average force.

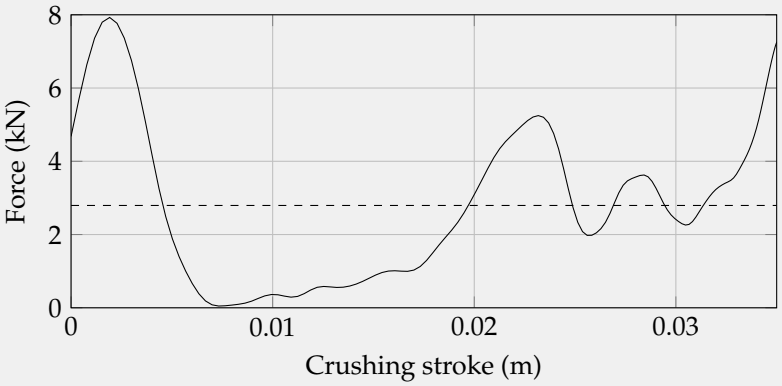

Figure A.6: Force-crushing stroke curves of the tested specimen MK. Dashed line represents the average force.

of collapse of these two parts. The parts on the sides are pushed aside. The pieces of debris are compacted, the impact energy is fully absorbed by the sample, and the maximum crush stroke is reached (Figure A.4d).

A.3.2 Load response

Figures A.5 and A.6 illustrate the force-displacement curves for the selected samples from the series P15 and MK, respectively. Curves of specimens with results closest to the mean values are shown. The initial peak recorded for both types of the block was also the largest or one of the largest, indicating that all of the impact energy could be absorbed by the sample. The average force of the block P15 was approximately 3 times greater than the average force of the blocks examined in Chapter 3, which is probably related to the block's thicker cell walls and shorter cell width. Probably for the same reason the peak force of block P15 was also approximately 3 times greater. Another reason may be the imperfection of the progressive collapse of the sample P15, during which more cells were crushed at the same time, which could also increase the value of the maximum force. The maximum and the average forces of the block MK are more than twice as large as those of block P15. This is very likely associated with the larger width of block MK. Similarly, the shorter length of block MK led to a significantly shorter crushing stroke. Due to the different dimensions of the blocks, the crashworthiness of their cellular structures cannot be easily compared on the basis of force-displacement

curves. Therefore, the indicators of crashworthiness are needed to compare the overall crashworthiness of samples.

A.3.3 Indicators of crashworthiness

A.3.3.1 Energy absorption

Both tested blocks absorbed all the impact energy and, therefore, their crashworthiness cannot be compared on the basis of the indicator EA. For the same reason, SEA, $VSEA$, and multiple-criteria decision making methods are not discussed. Higher impact energy would be needed to establish the energy absorption of the tested blocks. Based on current observations (given the number of intact cells and the amount of pieces of debris accumulated between the impactor and the support), it can only be assumed that the energy absorption capacity of the block P15 would be greater. However, it can be noted that both blocks tested here show a higher energy absorption capacity than the blocks tested in Chapter 3.

A.3.3.2 Peak crush force

The peak crush force of blocks P15 and MK was 3014 kN and 7775 kN, respectively. This significant difference is probably associated with different sample widths and different crushing processes, during which different cell numbers fractured together. The peak crush forces of both blocks were many times larger than those of blocks studied in Chapter 3, and a significantly higher deceleration would be expected to be felt by the occupants of a vehicle during a collision. This is likely linked to thicker cell walls, a smaller ratio of cell width to cell wall thickness, and a lack of collapse progressivity, as described in Section A.3.2.

A.3.3.3 Energy absorption efficiency

The energy absorption efficiency of blocks P15 and MK was 32.1 J/kN and 12.7 J/kN, respectively. However, comparing these two values could be misleading, as neither sample was exposed to higher impact energy than its energy absorption capacity. For the same reason, it is not possible to compare the values with those determined in Chapter 3. These were higher, but it can be expected that the EAE of the samples tested here would increase with increasing absorbed energy, while the value of the maximum force would remain similar.

A.3.3.4 Mean crush force

The mean crush force of blocks P15 and MK was 918 kN and 2581 kN, respectively. However, it would be misleading to compare these values, given the different sample dimensions. The dimensions of the block P15 were similar to those measured for the blocks in Chapter 3, but its MCF was significantly larger. It can be deduced that the collision with the block P15 is more serious and the risk of injury to vehicle occupants of the vehicle is higher. Possible reasons for this are mentioned in Section A.3.2

A.3.3.5 Crush force efficiency

The crush force efficiency of blocks P15 and MK was 0.306 and 0.334, respectively. Which is too small a difference to draw any substantive conclusions. Similar values were measured for blocks tested in Chapter 3.

A.3.3.6 Crush efficiency

The crush efficiency of blocks P15 and MK was 0.355 and 0.224, respectively. Not only did the sample reach higher CE, the gap between the impactor and the support at the end of its deformation process (Figure A.3e) indicates that its potential for compaction will be even higher. Therefore, it can be inferred that the length utilisation of block P15 is much higher than that of block MK. CE of blocks in Chapter 3 was even higher, however given the fact that the limit of crushing stroke was not reached during the collapse of block P15, it is not possible to compare their length utilisation.

A.3.3.7 Energy efficiency

The energy efficiency of blocks P15 and MK was 0.107 and 0.075, respectively. This suggests that the block P15 is better for achieving a stable reaction force throughout the long deformation process. A comparison with blocks from Chapter 3 could be misleading as the limit energy absorption and the limit crush stroke have not been reached.

A.3.3.8 Work efficiency

The work efficiency of blocks P15 and MK was 7.04 J/kg and 4.43 J/kg, respectively. However, caution is again required when comparing these values, due to impact energy and measured crushing stroke not exceeding the energy absorption and deformation limits, respectively. Due to the number of its intact cells and its potential for a significant prolongation of the deformation process, the block P15 could be described as more capable of absorbing more impact energy and allowing the impact body to decelerate on a larger stroke. The WE values of both blocks tested here were between the maximum and the minimum WE values measured in Chapter 3. However, this comparison would again be misleading, for all the reasons mentioned above.

A.4 Conclusions

This study investigated the impact responses of brittle blocks with thin-walled cellular structures that were excluded from the comparative study in Chapter 3. The following inferences can be drawn from the study:

1. The two blocks tested differed in their external dimensions and the composition of their cellular structure. Block P15 was longer, narrower, and consisted of rectangular cells; block MK was shorter, wider, and was composed of rectangular and hexagonal cells. Block P15 came out better from all feasible comparisons. By adding its potential for a significant prolongation of the deformation process and the number of its intact cells at the end of the crushing process, it can be concluded that the block P15 shows better crashworthiness.

2. Both blocks tested here showed enhanced energy absorption compared to those studied in Chapter 3. On the other hand, collision with these blocks would be much more severe for vehicle occupants. Given the fact, that the block P15 showed better crashworthiness compared to the block MK and its dimensions are similar to block dimensions in Chapter 3, it could be considered as a semi-stiff element in studies devoted to the study of the combination of samples with different crashworthiness measures, in which soft and semi-soft elements would be represented by samples +40 and STI44, respectively, from Chapter 3.

3. An increase risk of injury for imaginary vehicle occupants is associated with a thicker cell wall, a larger ratio of cell wall thickness to cell width, and a lack of collapse progressivity. If we omit the difference in the base material, the block in Chapter 4 had similarly thick walls as the block P15, but its ratio of cell wall thickness to cell width was 0.1 instead of 0.28, and the block gradually collapsed. Due to these shortcomings, the blocks tested here were excluded from the comparative study described in Chapter 3.

4. Despite the shortcomings of the tested blocks, it was possible to compare them in terms of crashworthiness using the methodology introduced in Chapter 3, which proves the robustness of this assessment methodology.

Appendix B

The severity of a collision with brittle blocks with cellular structures

B.1 Introduction

The proportion of motor vehicle crash deaths involving a collision with fixed objects has remained between 19% and 23% since 1979 in the USA according to the U.S. National Highway Traffic Safety Administration [68] and between 20% and 28% since 2000 in the Czech Republic according to the Directorate of Traffic Police Service of the Police Presidium of the Czech Republic [71]. To address this issue and consequently to decrease transportation hazards, a novel crash cushion comprised of brittle blocks with cellular structures was introduced [1–3]. The contained brittle blocks can be used as cushioning elements dissipating the impact energy because of the gradual brittle fracture process in their cellular structures with their cell walls serving as supporting elements. Two versions of the novel crash cushion have been developed: the alpha version [1, 2] made of fired clay (FC) and the beta version [3] made of high-performance concrete (HPC). Both versions are capable of decelerating the impact vehicle gradually, have reasonable production cost, and are suitable for mass production. The alpha version has a limited lifetime in harsh environmental conditions and may, therefore, fail during the service life of a structure; the beta version is suitable for use in harsh environments due to the durability of the base material. The crash cushions were subjected to a testing program involving impact of a 50 kg flat-nosed impactor [2, 3], a 1,000 kg flat-nosed cart [1, 3], and a 1,100 kg passenger vehicle [1]. In the past investigations, significant insight into the energy absorption process of crash cushions was gained and the vehicle kinematics and deformations, the developed crushing forces, and the crashworthiness of cushioning elements were carefully examined and described in detail. In this contribution, the recorded data are used to evaluate the acceleration severity index that is assumed to be proportional to passenger injury risk. There is a significant reduction in the severity of the impact due to the crash cushions compared to a rigid wall frontal impact. In addition, the effect of impact velocity on collision severity is discussed and both versions of crash cushions are compared in occupant injury potential. Inferences drawn from this study can be used by designers and contractors to assess the collision severity and optimise the use of the cushioning elements. The presented cushioning elements can replace stones and solid blocks in cross-drainage culverts, but hypothetically they could also be used in other structures which pose risks around traffic lanes or in underwater protection of bridge piers.

Table B.1: Tolerable acceleration limits for different restraint conditions. Values are in multiples of earth's gravity. [163]

	Longitudinal	Transverse	Vertical
Unrestrained occupant	7	5	6
Lap belt restraint	12	9	10
Lap and shoulder harness	20	15	17

B.2 Methodology

B.2.1 Assessment methodology

To assess a collision severity, Acceleration Severity Index (ASI) is most commonly used [154–163] and it is considered to be the most representative parameter determining the effect of a collision on vehicle passengers [155, 157]. The $ASI(t)$ is a scalar function of time and its time history can be evaluated using all three normalised accelerations measured at the vehicle's centre of gravity:

$$ASI(t) = \sqrt{\left(\frac{\bar{a}_L}{\hat{a}_L}\right)^2 + \left(\frac{\bar{a}_T}{\hat{a}_T}\right)^2 + \left(\frac{\bar{a}_V}{\hat{a}_V}\right)^2} \tag{B.1}$$

where $\hat{a}_L$, $\hat{a}_T$, $\hat{a}_V$ are limit acceleration values along longitudinal, transverse, and vertical axis respectively. The limit values related to the thresholds of human tolerability for different restraint conditions are shown in Table B.1. Generally used threshold accelerations for the fastened passenger ([154, 156, 157, 159–161, 164], which are also the limit values used in this study) are 12g, 9g, and 10g respectively. $\bar{a}_L$, $\bar{a}_T$, $\bar{a}_V$ are accelerations of the vehicle's centre of gravity for each component direction. These acceleration components should be filtered to remove high-frequency noise before substituting into Equation B.1.

Several authors [154, 156, 157, 159, 161] averaged the measured accelerations over a moving time interval:

$$\bar{a}(t) = \frac{\int_t^{t+t_f} a\mathrm{d}t}{t_f} \tag{B.2}$$

where t_f is 50 ms or its equivalent in the units used.

Later [160, 164], the moving average filter with a 50 ms window was replaced by a fourth order phaseless Butterworth digital filters. In the first step, the measured accelerations are filtered using the low-pass filter CFC180 [126–129] as recommended in [165]. The Channel Frequency Class (CFC) filters were derived from analog Butterworth filters that had a corner frequency equal to the CFC designation divided by 0.6 and their filter sequence is described by the following difference equation [129]:

$$Y(k) = a_0X(k) + a_1X(k-1) + a_2X(k-2) + b_1Y(k-1) + b_2Y(k-2) \tag{B.3}$$

where $X(k)$ is the k$^{\text{th}}$ element of the input data sequence, $Y(k)$ is the k$^{\text{th}}$ element of the filtered output data sequence and a_0, a_1, a_2, b_1, and b_2 are filter constants:

$$a_0 = \frac{w_a^2}{1 + \sqrt{2}w_a + w_a^2} \tag{B.4}$$

$$a_1 = 2a_0 \tag{B.5}$$

$$a_2 = a_0 \tag{B.6}$$

$$b_1 = \frac{-2(w_a^2 - 1)}{1 + \sqrt{2}w_a + w_a^2} \tag{B.7}$$

$$b_2 = \frac{-1 + \sqrt{2}w_a - w_a^2}{1 + \sqrt{2}w_a + w_a^2} \tag{B.8}$$

where

$$w_a = \tan\left(w_d \frac{T}{2}\right) \tag{B.9}$$

$$w_d = 2\pi CFCp \tag{B.10}$$

where T is a sampling rate in seconds, CFC is the filter class, and p is an empirical constant equal to 2.075. Following this, the data were further low-pass filtered using a fourth order phaseless Butterworth digital filter with a cut-off frequency of 13 Hz as recommended in [164]. The filter sequence was again described by the difference equation B.3 where only the filter constant w_d was quantified differently:

$$w_d = 2\pi CFR \tag{B.11}$$

where CFR is a cut-off frequency. The data of the two-channel filter (Equation B.3) has to run forwards as well as backwards to realise a four-channel filter and to prevent phase displacements.

The maximum value of $ASI(t)$ (Equation B.1) is a dimensionless parameter taken as a single measure of collision severity [154, 161]:

$$ASI = \max\left(ASI(t)\right) \tag{B.12}$$

It utilises vehicle accelerations that are expected to be transferred to the passenger [161] and indicates a collision severity for a passenger that is in constant contact with the vehicle [161] and sits in the seat close to the reference point [157]. The ASI increases with impact velocity and angle [160] and it is assumed to be proportional to passenger injury risk [161].

The threshold values of ASI were established and standardised in [166, 167]. The recommended limit value for impact at 30 km/h is 1 and the threshold values for impacts at 50 km/h and above are given in Table B.2. The standards define impact severity levels bounded by these threshold values assuming that each impact severity level corresponds to its own passenger injury level [158]. However, the standards do not give any reference to the expected injury severity associated with the established impact severity levels, nor to the theoretical or empirical evidence to support the threshold values [158]. It was stated in [161] that few studies were conducted on the relationship between ASI and actual passenger injury and that the biomechanical basis for the threshold values was not well documented. Therefore, the correlation between the ASI and occupant injury risk was investigated using experimental and numerical analyses [159] and limits at which the risk of injury could be considered acceptable were proposed (see Table B.3). The neck was identified as a human body part most prone to injury. Its injury measurements were found to be below the limits derived from volunteering testing for crashes with ASI up to 1.5. Moreover, these limits are expected to be significantly lower than the levels at which injuries may occur. For crashes with ASI up to 1.8, neck injuries measurements above the tolerable thresholds for injury were considered unconvincing. Unacceptable injury measurements for the neck were recorded in crashes with ASI above 2. The injury

Table B.2: Threshold values of the Acceleration Severity Index (ASI) for support structures with high energy absorption capacity impacted at a speed of 50 km/h and above [166, 167].

	$ASI < 1$	$1 < ASI < 1.2$	$1.2 < ASI < 1.4$
Passenger safety level	3	2	1
Impact severity level	A	B	B

Table B.3: Correlation between the risk of injury and the Acceleration Severity Index (ASI) [159].

	$ASI < 1.5$	$1.5 < ASI < 1.8$	$2 < ASI$
Head injury	very low risk	very low risk	high risk
Neck injury	very low risk	low risk	high risk
Chest injury	very low risk	very low risk	high risk

measurements for the head and chest were within acceptable limits for impacts with ASI below 2 and the threshold values of abdomen and pelvis injuries were not exceeded in the study. It was stated elsewhere [163] that no injuries of an unrestrained passenger and a passenger with a fastened seatbelt are expected for crashes with ASI up to 1 and 1.6 respectively. However, this statement was not supported by relevant studies.

B.2.2 Review of experimental methodology

It is apparent from Equation B.1 that the desired output of experiments is three acceleration components of an impact vehicle. Two different vehicles were employed: a non-deformable flat-nosed cart and an ordinary passenger vehicle. A triaxial accelerometer was placed on the body of each vehicle to record the data needed to plot the time evolution of the ASI. The global maximum of the curve can be taken as an indication of passenger injury potential. Two versions of the novel crash cushion were tested. Both are composed of brittle blocks with cellular structures; one is made of high-performance concrete, the other of fired clay. Cells were distributed regularly; each row was offset by half of the cell spacing. A detailed description of test setups can be found in [1, 3] and is, therefore, omitted for the sake of brevity here.

B.2.2.1 Impact of non-deformable flat-nosed cart

Both versions of crash cushion were subjected to the impact of a 1000 kg non-deformable flat-nosed impact cart (Figure B.1). Their back face was placed against a rigid wall while their lateral movement was not restricted.

The alpha version made of fired clay was composed of two parts. The stricken part comprised of 45 ground bricks, 5 wide and 3 tall/long. The longitudinal sides of its bricks were trimmed to eliminate tong and groove joint. The width of a block was 200 mm. The second part adjacent to the rigid wall was wrapped in plastic foil and comprised of 36 bricks, 4 wide and 3 tall/long. The cells of its bricks were filled with polystyrene. The width of a block was 250 mm. Cells of blocks used in both parts were diamond-shaped with dimensions of 63.4 mm × 10.2 mm (width × height) and a wall thickness of 3.7 mm. The dimensions of a block were 500 mm × 250 mm (length × height). Dimensions of the entire specimen were 1000 mm × 3000 mm × 750 mm (width × length × height).

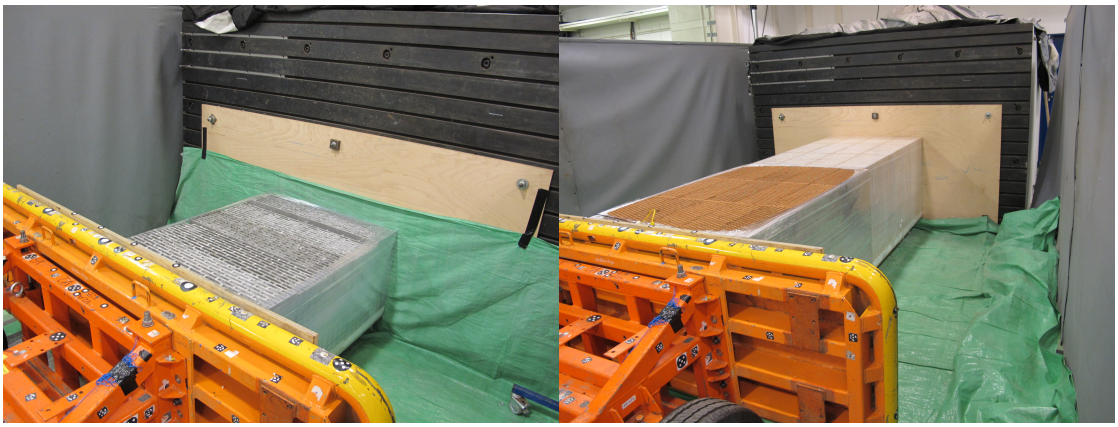

(a) Collision with a crash cushion made of high-performance concrete.

(b) Collision with a crash cushion made of fired clay.

Figure B.1: Impact of a non-deformable flat-nosed cart.

(a) Collision with a crash cushion made of fired clay.

(b) Collision with a non-deformable reinforced concrete wall.

Figure B.2: Impact of a passenger vehicle with crumple zones.

The beta version made of high-performance concrete comprised of 24 blocks, 1 wide, 4 tall, and 6 long. The cells were rectangular with dimensions of 100 mm × 15 mm (width × height) and a wall thickness of 10 mm. Dimensions of a block were 1000 mm × 250 mm × 125 mm (width × length × height). Dimensions of the entire specimen were 1000 mm × 1500 mm × 500 mm (width × length × height).

Both versions were impacted at a speed of 30 km/h, which set impact energy at 34.7 kJ. Moreover, the crash cushion made of fired clay was impacted at a speed of 50 km/h, which set impact energy at 96.5 kJ. Although the accelerometer was attached to the nose of the impact cart and not placed precisely at the cart's centre of gravity, it is expected that similar values to those required by Equation B.1 were recorded due to the cart rigidity.

B.2.2.2 Impact of passenger vehicle with crumple zones

The crash cushion made of fired clay was subjected to the frontal impact of an ordinary passenger vehicle (commercially available Skoda Fabia, 3rd generation). The mass of vehicle was 1.1 t and its impact velocity was 50 km/h, which set impact energy at 106 kJ. The specimen comprised of 162 bricks with trimmed longitudinal sides, 9 wide, 3 tall, 6 long. Bricks had similar dimensions as those described in the previous section. Dimensions of the entire specimen were 2000 mm × 3000 mm × 750 mm (width × length × height). For comparison purposes, the frontal collision of a similar vehicle with a stiff reinforced concrete wall was also conducted. Both impacted specimens were built into cross-drainage culverts embedded in the ground (Figure B.2).

B.3 Results

As outlined in the introduction, the main purpose of the tests was to establish the severity of a collision with crash cushions. Moreover, two versions of the crash cushion are compared in collision severity and the effect of impact velocity is studied. To investigate this, time histories and maximum values of acceleration severity index were closely examined. The recorded data were processed using the graphical development environment LabView [131] included in the National Instruments Diadem software package.

The graph showing ASI time histories for collisions of a non-deformable flat-nosed impact cart is shown in Figure B.3. By examining this graph, it can be concluded that two ASI peaks were recorded for each specimen. The first peak is associated with the first contact with the specimen. The second ASI increase is linked to the compaction of pieces of debris broken off of the cellular structure. At that time, the gradual fracture process of the cellular structure reaches the support or the semi-stiff part and the resulted pieces of debris are compacted. The semi-stiff part of the alpha version was not crushed at lower impact velocity. The detail description of the collapse process can be found in [1, 3] and is, therefore, omitted for the sake of brevity here.

At lower impact velocity, the maximum ASI values recorded for collisions with crash cushions made of high-performance concrete or fired clay were both equal to 0.5. It is noteworthy that although the maximum values are similar for both crash cushions, these maximums were reached at a different stage of collapse. It was reached at the first peak during the collision with the beta version, and at the second peak during the collision with the alpha version. The stricken part of alpha version, which consisted of trimmed hollow bricks, had a larger face and the same length as the beta version. Unlike the beta version, the stricken part of alpha version was placed against a semi-stiff part composed of filled bricks instead of against a rigid wall. If it were placed against a rigid wall, the second peak would be expected to be even higher. Taking this into account, it can be concluded that the beta version is preferable design for the 1.5m long crash cushion subjected to this specific impact condition. It gradually decelerated the impact cart and absorbed more energy during the collapse process. It showed greater stiffness, which is likely linked to its thicker cell walls. However, if the impact energy was lower or the crash cushion longer, the alpha version could be preferred.

When the impact velocity was higher, the maximum ASI value for the alpha version was 0.9, which is almost twice as large as when the velocity was lower. This confirms that ASI parameter increases with increasing impact velocity. Compared to the lower speed impact, the first peak was reached at about the same time and the second peak was reached much earlier. This is most likely linked to a faster collapse of the cellular structure. The gradual deceleration of the impact cart was observed. The semi-stiff part was crushed and the second ASI peak was significantly lower than the first. If the stricken part was softer and the semi-stiff part stiffer, the first peak could be lower and the second higher, thus the maximum ASI value and the associated risk of potential passenger injury lower. The strictest ASI limit of 1 was not exceeded during any test and it can be expected that the ASI values would not increase if a vehicle with crumple zones and the same mass were used, so the potential for occupant risk is considered very low.

The graph showing ASI time histories for collisions of an ordinary 1.1 t passenger vehicle is shown in Figure B.4. The maximum ASI value for the collision with the alpha version was 0.8, similar to the collision of a 1 t cart at the same impact velocity. The strictest ASI limit was not exceeded, thus the risk of injury for the passenger of the impacting

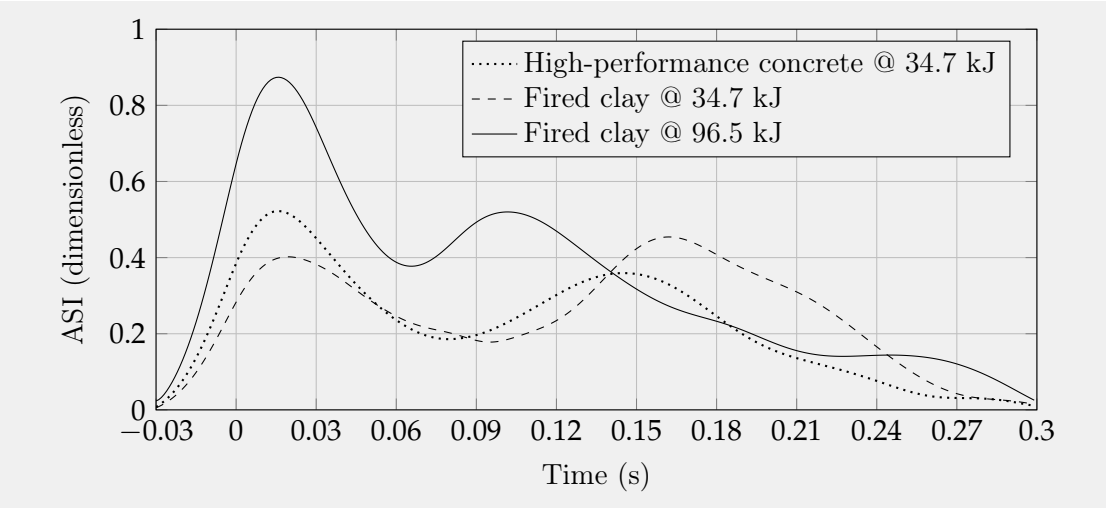

Figure B.3: Time evolution of Acceleration Severity Index during collisions of a non-deformable flat-nosed cart impacting at different impact energies with crash cushions made of various materials.

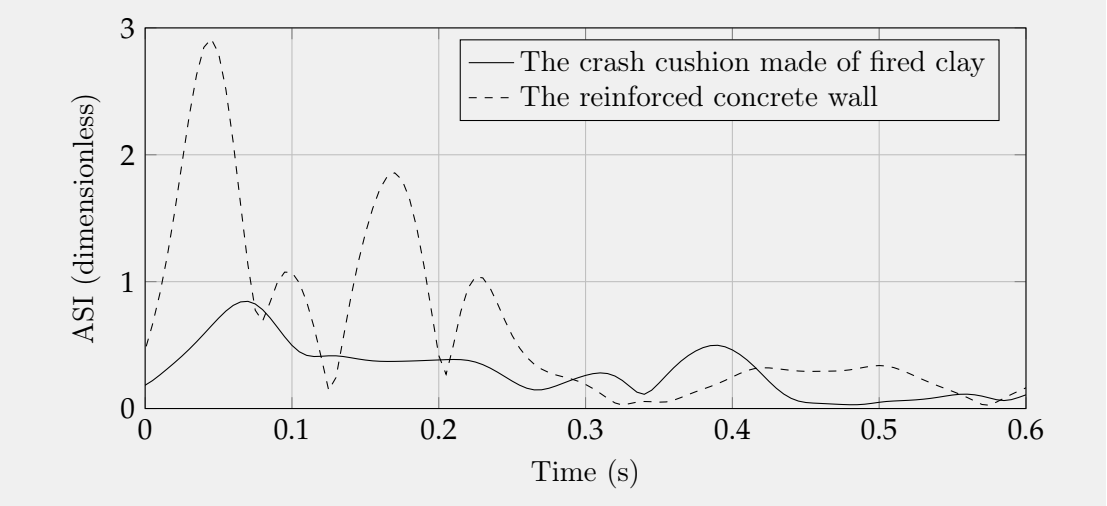

Figure B.4: Time evolution of Acceleration Severity Index during collisions of a passenger vehicle with a crash cushion and a reinforced concrete wall.

vehicle is considered very low. In contrast, the maximum ASI value for the collision with the reinforced concrete wall was 2.9, which is 3.5 times higher compared to the collision with the crash cushion. This value exceeds every recommended threshold, thus the risk of passenger injury is considered very high. This demonstrates the ability of the presented crash cushion to significantly decrease the collision severity.

B.4 Conclusions

The previously performed impact tests of brittle blocks with cellular structures made of fired clay or high-performance concrete were revisited and new findings were obtained regarding the effect of the collision on vehicle passengers. To the author's knowledge, the data presented are the first of their kind. The following inferences can be drawn from the study:

1. The ASI parameter increases with increasing impact velocity.

2. Two ASI peaks were recorded for collisions of a non-deformable flat-nosed impact cart. The first peak is associated with the first contact with the specimen. The second ASI peak is linked to the compaction of pieces of debris broken off of the cellular structure or to the collapse of the semi-stiff part placed between the stricken part and the rigid wall.

3. The results indicate that the ASI value could be lowered by combining parts with different stiffness. The stricken part—impacted at full speed—should be softer to reduce the initial ASI peak. The second part—impacted at reduced velocity—could be designed stiffer to fully decelerate the vehicle. However, each additional peak should always be lower than the initial. This design process will be verified in future work.

4. The blocks made of high-performance concrete were stiffer than those of fired clay. They were more suitable for a crash cushion with maximum external dimensions limited to 1000 mm × 1500 mm × 750 mm (width × length × height), which was subjected to an impact of a 1000 kg non-deformable cart at 30 km/h. The crash cushion made of high-performance concrete was able to fully decelerate the impact cart and the second peak associated with the compaction of the resulted pieces of debris was lower than the initial.

5. In contrast to the collision with the reinforced concrete wall, while impacting the crash cushion, the ASI parameter was 3.5 times lower and kept below its strictest threshold, thus the risk of passenger injury was significantly reduced and is considered very low.

6. The ability of the presented crash cushion to significantly decrease the collision severity was verified. However, the ASI parameter only measures vehicle kinematics and can be only used for indirect estimates of occupant injury risk. It was noted [162] that vehicle kinematics may not accurately predict head kinematics during impact testing. An upper cockpit deformation can reduce measured ASI values and the head of a passenger is more likely to hit a deformed cockpit. This study could be extended to evaluate other parameters, such as Theoretical Head Impact Velocity ($THIV$), Real Head Impact Velocity ($RHIV$), Head Injury Criterion (HIC_{15}), Neck injury Criterion (N_{ij}), Abbreviated Injury Scale (AIS), and Vehicle Cockpit Deformation Index ($VCDI$). However, this was outside the scope of this study, where only vehicle accelerations were examined and not head or neck accelerations etc. Also, the cockpit deformation was not observed during the crash tests.

Bibliography

[1] Petr Hála et al. “Fracture behaviour of ceramic blocks with thin-walled cellular structures under dynamic loadings”. In: Thin-Walled Structures 122 (2017), pp. 597–605. issn: 02638231. doi: 10.1016/j.tws.2017.10.050.

[2] Petr Hála et al. “Comparative study on the crashworthiness of brittle blocks with thin-walled cellular structures”. In: Thin-Walled Structures 148.December 2019 (2020). issn: 02638231. doi: 10.1016/j.tws.2019.106578.

[3] Petr Hála et al. “Energy absorbing system made of high performance concrete”. In: Construction and Building Materials 139 (2017), pp. 64–80. issn: 09500618. doi: 10.1016/j.conbuildmat.2017.02.048.

[4] Petr Hála et al. High-Load Bearing Deformation Block Made of UHPC. Albany, New York, 2019.

[5] Xianqian Wu et al. “Dynamic response of shear thickening fluid under laser induced shock”. In: Applied Physics Letters 106.7 (2015). issn: 00036951. doi: 10.1063/1.4913423.

[6] Xianqian Wu, Qiuyun Yin, and Chenguang Huang. “Experimental study on pressure, stress state, and temperature-dependent dynamic behavior of shear thickening fluid subjected to laser induced shock”. In: Journal of Applied Physics 118.17 (2015). issn: 10897550. doi: 10.1063/1.4934857.

[7] Xianqian Wu et al. “Dynamic energy absorption behavior of lattice material filled with shear thickening fluid”. In: Procedia Engineering 199 (2017), pp. 2514–2518. issn: 18777058. doi: 10.1016/j.proeng.2017.09.431.

[8] Amanda S Lim et al. “Investigating the transient response of a shear thickening fluid using the split Hopkinson pressure bar technique”. In: Rheologica Acta 49.8 (2010), pp. 879–890. issn: 1435-1528. doi: 10.1007/s00397-010-0463-8.

[9] Scott R. Waitukaitis and Heinrich M. Jaeger. “Impact-activated solidification of dense suspensions via dynamic jamming fronts”. In: Nature 487.7406 (July 2012), pp. 205–209. issn: 00280836. doi: 10.1038/nature11187.

[10] Weifeng Wanquan Jiang et al. “Stress pulse attenuation in shear thickening fluid”. In: Applied Physics Letters 102.10 (2013). doi: 10.1063/1.4795303.

[11] Jonathan Bender and Norman J. Wagner. “Reversible shear thickening in monodisperse and bidisperse colloidal dispersions”. In: Journal of Rheology 40.5 (1996). doi: 10.1122/1.550767.

[12] Edward F. O’Neil et al. “Development of frangible concrete to reduce blast-related casualties”. In: ACI Materials Journal 109.1 (2012), pp. 31–40. issn: 0889325X.

[13] Weiguo Shen et al. “Investigation on the safety concrete for highway crash barrier”. In: Construction and Building Materials 70 (2014), pp. 394–398. issn: 09500618. doi: 10.1016/j.conbuildmat.2014.07.060.

[14] A. G. Mamalis et al. “Crashworthy capability of composite material structures”. In: Composite Structures 37.2 (1997), pp. 109–134. issn: 02638223. doi: 10.1016/S0263-8223(97)80005-0.

[15] Qiang Liu et al. “Lateral crushing and bending responses of CFRP square tube filled with aluminum honeycomb”. In: Composites Part B: Engineering 118 (2017), pp. 104–115. issn: 13598368. doi: 10.1016/j.compositesb.2017.03.021.

[16] Jie Song, Yan Chen, and Guoxing Lu. “Light-weight thin-walled structures with patterned windows under axial crushing”. In: International Journal of Mechanical Sciences 66 (2013), pp. 239–248. issn: 00207403. doi: 10.1016/j.ijmecsci.2012.11.014.

[17] Jie Song and Fenglin Guo. “A comparative study on the windowed and multi-cell square tubes under axial and oblique loading”. In: Thin-Walled Structures 66 (2013), pp. 9–14. issn: 02638231. doi: 10.1016/j.tws.2013.02.002.

[18] Hamid Nikkhah et al. “The effect of different shapes of holes on the crushing characteristics of aluminum square windowed tubes under dynamic axial loading”. In: Thin-Walled Structures 119 (2017), pp. 412–420. issn: 02638231. doi: 10.1016/j.tws.2017.06.036.

[19] C. Graciano, G. Martínez, and D. Smith. “Experimental investigation on the axial collapse of expanded metal tubes”. In: Thin-Walled Structures 47.8-9 (2009), pp. 953–961. issn: 02638231. doi: 10.1016/j.tws.2009.02.002.

[20] C. Graciano, G. Martínez, and A. Gutiérrez. “Failure mechanism of expanded metal tubes under axial crushing”. In: Thin-Walled Structures 51 (2012), pp. 20–24. issn: 02638231. doi: 10.1016/j.tws.2011.11.001.

[21] G. Martínez, C. Graciano, and P. Teixeira. “Energy absorption of axially crushed expanded metal tubes”. In: Thin-Walled Structures 71 (2013), pp. 134–146. issn: 02638231. doi: 10.1016/j.tws.2013.05.003.

[22] D. Smith et al. “Axial crushing of flattened expanded metal tubes”. In: Thin-Walled Structures 85 (2014), pp. 42–49. issn: 02638231. doi: 10.1016/j.tws.2014.08.001.

[23] Helio Borges, Gabriela Martínez, and Carlos Graciano. “Impact response of expanded metal tubes: A numerical investigation”. In: Thin-Walled Structures 105 (2016), pp. 71–80. issn: 02638231. doi: 10.1016/j.tws.2016.04.005.

[24] A. Ghodsbin Jahromi and H. Hatami. “Energy absorption performance on multi-layer expanded metal tubes under axial impact”. In: Thin-Walled Structures 116 (2017), pp. 1–11. issn: 02638231. doi: 10.1016/j.tws.2017.03.005.

[25] H. Hatami, M. Shokri Rad, and A. Ghodsbin Jahromi. “A theoretical analysis of the energy absorption response of expanded metal tubes under impact loads”. In: International Journal of Impact Engineering 109 (2017), pp. 224–239. issn: 0734743X. doi: 10.1016/j.ijimpeng.2017.06.009.

[26] Ahmad Baroutaji, Mustafa Sajjia, and Abdul Ghani Olabi. “On the crashworthiness performance of thin-walled energy absorbers: Recent advances and future developments”. In: Thin-Walled Structures 118.April (2017), pp. 137–163. issn: 02638231. doi: 10.1016/j.tws.2017.05.018.

[27] M. Avalle and L. Goglio. “Static lateral compression of aluminium tubes: Strain gauge measurements and discussion of theoretical models”. In: Journal of Strain Analysis for Engineering Design 32.5 (1997), pp. 335–343. issn: 03093247. doi: 10.1243/0309324971513454.

[28] N. K. Gupta, G. S. Sekhon, and P. K. Gupta. “Study of lateral compression of round metallic tubes”. In: Thin-Walled Structures 43.6 (2005), pp. 895–922. issn: 02638231. doi: 10.1016/j.tws.2004.12.002.

[29] Zhihua Fan et al. “Dynamic lateral crushing of empty and sandwich tubes”. In: International Journal of Impact Engineering 53 (2013), pp. 3–16. issn: 0734743X. doi: 10.1016/j.ijimpeng.2012.09.006.

[30] Shanqing Xu et al. “Collision and rebounding of circular rings on rigid target”. In: International Journal of Impact Engineering 79 (2015), pp. 14–21. issn: 0734743X. doi: 10.1016/j.ijimpeng.2014.07.005.

[31] A. Baroutaji et al. “Crush analysis and multi-objective optimization design for circular tube under quasi-static lateral loading”. In: Thin-Walled Structures 86 (2015), pp. 121–131. issn: 02638231. doi: 10.1016/j.tws.2014.08.018.

[32] A. Baroutaji, E. Morris, and A. G. Olabi. “Quasi-static response and multi-objective crashworthiness optimization of oblong tube under lateral loading”. In: Thin-Walled Structures 82 (2014), pp. 262–277. issn: 02638231. doi: 10.1016/j.tws.2014.03.012.

[33] N. K. Gupta, G. S. Sekhon, and P. K. Gupta. “A study of lateral collapse of square and rectangular metallic tubes”. In: Thin-Walled Structures 39.9 (2001), pp. 745–772. issn: 02638231. doi: 10.1016/S0263-8231(01)00033-7.

[34] Abbas Niknejad et al. “Theoretical and experimental study on the flattening deformation of the rectangular brazen and aluminum columns”. In: Archives of Civil and Mechanical Engineering 13.4 (2013), pp. 449–464. issn: 16449665. doi: 10.1016/j.acme.2013.04.008.

[35] T. N. Tran and T. N T Ton. “Lateral crushing behaviour and theoretical prediction of thin-walled rectangular and square tubes”. In: Composite Structures 154.December (2016), pp. 374–384. issn: 02638223. doi: 10.1016/j.compstruct.2016.07.068.

[36] Abbas Niknejad and Danesh M. Rahmani. “Experimental and theoretical study of the lateral compression process on the empty and foam-filled hexagonal columns”. In: Materials and Design 53 (2014), pp. 250–261. issn: 18734197. doi: 10.1016/j.matdes.2013.06.077.

[37] Peng Wang et al. “Quasi-static crushing behaviors and plastic analysis of thin-walled triangular tubes”. In: Journal of Constructional Steel Research 106 (2015), pp. 35–43. issn: 0143974X. doi: 10.1016/j.jcsr.2014.12.004.

[38] Hualin Fan et al. “Lateral compression behaviors of thin-walled equilateral triangular tubes”. In: International Journal of Steel Structures 15.4 (2015), pp. 785–795. issn: 20936311. doi: 10.1007/s13296-015-1202-x.

[39] Trong Nhan Tran. “Crushing and theoretical analysis of multi-cell thin-walled triangular tubes under lateral loading”. In: Thin-Walled Structures 115.February (2017), pp. 205–214. issn: 02638231. doi: 10.1016/j.tws.2017.02.027.

[40] Edmund Morris, A. G. Olabi, and M. S.J. Hashmi. “Analysis of nested tube type energy absorbers with different indenters and exterior constraints”. In: Thin-Walled Structures 44.8 (2006), pp. 872–885. issn: 02638231. doi: 10.1016/j.tws.2006.08.014.

[41] T. Yella Reddy and S. R. Reid. “Lateral compression of tubes and tube-systems with side constraints”. In: International Journal of Mechanical Sciences 21.3 (1979), pp. 187–199. issn: 00207403. doi: 10.1016/0020-7403(79)90023-7.

[42] Yuli Chen et al. “A novel self-locked energy absorbing system”. In: Journal of the Mechanics and Physics of Solids 87 (Feb. 2016), pp. 130–149. issn: 00225096. doi: 10.1016/j.jmps.2015.11.008.

[43] Kuijian Yang et al. “Internally nested self-locked tube system for energy absorption”. In: Thin-Walled Structures 119 (2017), pp. 371–384. issn: 02638231. doi: 10.1016/j.tws.2017.06.014.

[44] A. G. Olabi, Edmund Morris, and M. S.J. Hashmi. “Metallic tube type energy absorbers: A synopsis”. In: Thin-Walled Structures 45.7-8 (2007), pp. 706–726. issn: 02638231. doi: 10.1016/j.tws.2007.05.003.

[45] Edmund Morris, A. G. Olabi, and M. S.J. Hashmi. "Lateral crushing of circular and non-circular tube systems under quasi-static conditions". In: Journal of Materials Processing Technology 191.1-3 (2007), pp. 132–135. issn: 09240136. doi: 10.1016/j.jmatprotec.2007.03.006.

[46] Edmund Morris et al. "Experimental and Numerical Analysis of Circular Tube Systems Under Quasi-Static and Dynamic Loading ." In: Experimental Analysis of Nano and Engineering Materials and Structures. (2007), pp. 801–802. doi: 10.1007/978-1-4020-6239-1{_}398.

[47] A. G. Olabi et al. "Optimised design of nested circular tube energy absorbers under lateral impact loading". In: International Journal of Mechanical Sciences 50.1 (2008), pp. 104–116. issn: 00207403. doi: 10.1016/j.ijmecsci.2007.04.005.

[48] A. G. Olabi et al. "Optimised design of nested oblong tube energy absorbers under lateral impact loading". In: International Journal of Impact Engineering 35.1 (2008), pp. 10–26. doi: 10.1016/j.ijimpeng.2006.11.007.

[49] Haibo Wang et al. "Internally nested circular tube system subjected to lateral impact loading". In: Thin-Walled Structures 91 (2015), pp. 72–81. issn: 02638231. doi: 10.1016/j.tws.2015.02.014.

[50] A. Baroutaji, M. D. Gilchrist, and A. G. Olabi. "Quasi-static, impact and energy absorption of internally nested tubes subjected to lateral loading". In: Thin-Walled Structures 98 (2016), pp. 337–350. issn: 02638231. doi: 10.1016/j.tws.2015.10.001.

[51] Abbas Niknejad and Pourya Heidari Orojloo. "A novel nested system of tubes with special cross-section as the energy absorber". In: Thin-Walled Structures 100 (2016), pp. 113–123. issn: 02638231. doi: 10.1016/j.tws.2015.12.009.

[52] Scott D. Papka and Stelios Kyriakides. "In-plane crushing of a polycarbonate honeycomb". In: International Journal of Solids and Structures 35.3-4 (Jan. 1998), pp. 239–267. issn: 0020-7683. doi: 10.1016/S0020-7683(97)00062-0.

[53] S.D. Papka and S. Kyriakides. "Experiments and full-scale numerical simulations of in-plane crushing of a honeycomb". In: Acta Materialia 46.8 (May 1998), pp. 2765–2776. issn: 1359-6454. doi: 10.1016/S1359-6454(97)00453-9.

[54] S. D. Papka and S. Kyriakides. "Biaxial crushing of honeycombs - Part I: Experiments". In: International Journal of Solids and Structures 36.29 (1999), pp. 4367–4396. issn: 00207683. doi: 10.1016/S0020-7683(98)00224-8.

[55] S. D. Papka and S. Kyriakides. "In-plane biaxial crushing of honeycombs - Part II: Analysis". In: International Journal of Solids and Structures 36.29 (1999), pp. 4397–4423. issn: 00207683. doi: 10.1016/S0020-7683(98)00225-X.

[56] D. Ruan et al. "In-plane dynamic crushing of honeycombs - A finite element study". In: International Journal of Impact Engineering 28.2 (2003), pp. 161–182. issn: 0734743X. doi: 10.1016/S0734-743X(02)00056-8.

[57] Zhijun Zheng, Jilin Yu, and Jianrong Li. "Dynamic crushing of 2D cellular structures: A finite element study". In: International Journal of Impact Engineering 32.1-4 (2006), pp. 650–664. issn: 0734743X. doi: 10.1016/j.ijimpeng.2005.05.007.

[58] Z. Zou et al. "Dynamic crushing of honeycombs and features of shock fronts". In: International Journal of Impact Engineering 36.1 (2009), pp. 165–176. issn: 0734743X. doi: 10.1016/j.ijimpeng.2007.11.008.

[59] S.R. Reid and C. Peng. "Dynamic uniaxial crushing of wood". In: International Journal of Impact Engineering 19.5-6 (1997), pp. 531–570. issn: 0734743X. doi: 10.1016/S0734-743X(97)00016-X.

[60] G. W. Ma, Z. Q. Ye, and Z. S. Shao. "Modeling loading rate effect on crushing stress of metallic cellular materials". In: International Journal of Impact Engineering 36.6 (2009), pp. 775–782. issn: 0734743X. doi: 10.1016/j.ijimpeng.2008.11.013.

[61] L. L. Hu and T. X. Yu. "Mechanical behavior of hexagonal honeycombs under low-velocity impact - Theory and simulations". In: International Journal of Solids and Structures 50.20-21 (2013), pp. 3152–3165. issn: 00207683. doi: 10.1016/j.ijsolstr.2013.05.017.

[62] Amin Ajdari, Hamid Nayeb-Hashemi, and Ashkan Vaziri. "Dynamic crushing and energy absorption of regular, irregular and functionally graded cellular structures". In: International Journal of Solids and Structures 48.3-4 (2011), pp. 506–516. issn: 00207683. doi: 10.1016/j.ijsolstr.2010.10.018.

[63] Jie Zheng, Qinghua Qin, and T. J. Wang. "Impact plastic crushing and design of density-graded cellular materials". In: Mechanics of Materials 94 (2016), pp. 66–78. issn: 01676636. doi: 10.1016/j.mechmat.2015.11.014.

[64] Jinxiu Qiao and Changqing Chen. "In-plane crushing of a hierarchical honeycomb". In: International Journal of Solids and Structures 85-86 (2016), pp. 57–66. issn: 00207683. doi: 10.1016/j.ijsolstr.2016.02.003.

[65] Jianguang Fang et al. "On design of multi-cell tubes under axial and oblique impact loads". In: Thin-Walled Structures 95 (2015), pp. 115–126. issn: 02638231. doi: 10.1016/j.tws.2015.07.002.

[66] J. Marsolek and H. G. Reimerdes. "Energy absorption of metallic cylindrical shells with induced non-axisymmetric folding patterns". In: International Journal of Impact Engineering 30.8-9 (2004), pp. 1209–1223. issn: 0734743X. doi: 10.1016/j.ijimpeng.2004.06.006.

[67] Javad Marzbanrad and Mohammad Reza Ebrahimi. "Multi-Objective Optimization of aluminum hollow tubes for vehicle crash energy absorption using a genetic algorithm and neural networks". In: Thin-Walled Structures 49.12 (2011), pp. 1605–1615. issn: 02638231. doi: 10.1016/j.tws.2011.08.009.

[68] The National Highway Traffic Safety Administration. Fatality Analysis Reporting System Encyclopedia. 2017. url: www-fars.nhtsa.dot.gov/Main/index.aspx.

[69] Tomáš Mičunek, Zuzana Schejbalová, and Drahomír Schmidt. "Access Bridge Design Measures for Safety Increase of Road Infrastructure". In: Safety and Security in Traffic Preliminary Communication 25.6 (2013), pp. 543–554. doi: 10.7307/ptt.v25i6.436.

[70] Insurance Institute for Highway Safety and Highway Loss Data Institute. Collisions with fixed objects and animals. url: https://www.iihs.org/topics/fatality-statistics/detail/collisions-with-fixed-objects-and-animals.

[71] Policie České republiky. Statistika nehodovosti. 2019. url: https://www.policie.cz/clanek/statistika-nehodovosti-900835.aspx.

[72] Dean L. Sicking et al. "Safety grates for cross-drainage culverts". In: Transportation Research Record 2060 (2008), pp. 67–73. doi: 10.3141/2060-08.

[73] Y. Zhou et al. "Field test and numerical modeling of vehicle impact on a boulder with impact-induced fractures". In: International Journal of Protective Structures 7.1 (2016), pp. 3–17. issn: 2041-4196. doi: 10.1177/2041419615622725.

[74] Elham Sahraei Esfahani and Kenneth S Opiela. "Safety Performance of Concrete Median Barriers under Updated Crashworthiness Criteria". In: Test October (2008).

[75] K.K. Mak and D.L. Sicking. "Rollover Caused by Concrete Safety Shaped Barrier". In: I.January (1989).

[76] Bo Hu, Guo Qiang Li, and Jian Yun Sun. "Numerical investigation of K4-rating shallow footing fixed anti-ram bollard system subjected to vehicle impact". In: International Journal of Impact Engineering 63 (2014), pp. 72–87. issn: 0734743X. doi: 10.1016/j.ijimpeng.2013.08.006.

[77] Lin Chen et al. "Test and numerical simulation of truck collision with anti-ram bollards". In: International Journal of Impact Engineering 75 (2015), pp. 1–10. issn: 0734743X. doi: 10.1016/j.ijimpeng.2014.07.011.

[78] Petr Máca, Jan Zatloukal, and Radoslav Sovják. "Design of a novel horizontal impact machine for testing of concrete specimens". In: WIT Transactions on the Built Environment 141 (2014), pp. 149–158. issn: 17433509. doi: 10.2495/SUSI140131.

[79] Elfetori F. Abdewi et al. "Quasi-static axial and lateral crushing of radial corrugated composite tubes". In: Thin-Walled Structures 46.3 (2008), pp. 320–332. issn: 02638231. doi: 10.1016/j.tws.2007.07.018.

[80] Na Qiu et al. "Crashworthiness analysis and design of multi-cell hexagonal columns under multiple loading cases". In: Finite Elements in Analysis and Design 104 (2015), pp. 89–101. issn: 0168874X. doi: 10.1016/j.finel.2015.06.004.

[81] F. Tarlochan et al. "Design of thin wall structures for energy absorption applications: Enhancement of crashworthiness due to axial and oblique impact forces". In: Thin-Walled Structures 71 (2013), pp. 7–17. issn: 02638231. doi: 10.1016/j.tws.2013.04.003.

[82] Zhibin Li, Rong Chen, and Fangyun Lu. "Comparative analysis of crashworthiness of empty and foam-filled thin-walled tubes". In: Thin-Walled Structures 124 (2018), pp. 343–349. issn: 02638231. doi: 10.1016/j.tws.2017.12.017.

[83] Fan Weili and Zhang Xinchun. "Dynamic energy absorption of circular honeycomb under in-plane impact loading". In: 2010 International Conference on Digital Manufacturing & Automation 1 (2010), pp. 585–588. doi: 10.1109/ICDMA.2010.443.

[84] H. R. Zarei and M. Kröger. "Optimization of the foam-filled aluminum tubes for crush box application". In: Thin-Walled Structures 46.2 (2008), pp. 214–221. issn: 02638231. doi: 10.1016/j.tws.2007.07.016.

[85] Hamidreza Zarei and Matthias Kröger. "Optimum honeycomb filled crash absorber design". In: Materials and Design 29.1 (2008), pp. 193–204. issn: 18734197. doi: 10.1016/j.matdes.2006.10.013.

[86] Xiong Zhang et al. "Optimum design for energy absorption of bitubal hexagonal columns with honeycomb core". In: International Journal of Crashworthiness 13.1 (Jan. 2008), pp. 99–107. issn: 13588265. doi: 10.1080/13588260701731732.

[87] Daniel Jato-Espino et al. "A review of application of multi-criteria decision making methods in construction". In: Automation in Construction 45 (2014), pp. 151–162. issn: 09265805. doi: 10.1016/j.autcon.2014.05.013.

[88] Mahdi Bitarafan et al. "Selecting the best design scenario of the smart structure of bridges for probably future earthquakes". In: Procedia Engineering 57 (2013), pp. 193–199. issn: 18777058. doi: 10.1016/j.proeng.2013.04.027.

[89] Rajan L. Wankhade and Amarsinh B. Landage. "Non-destructive testing of concrete structures in karad region". In: Procedia Engineering 51 (2013), pp. 8–18. issn: 18777058. doi: 10.1016/j.proeng.2013.01.005.

[90] Y. Ilker Topcu. "A decision model proposal for construction contractor selection in Turkey". In: Building and Environment 39.4 (2004), pp. 469–481. issn: 03601323. doi: 10.1016/j.buildenv.2003.09.009.

[91] Kamal M.Al Subhi Al-Harbi. "Application of the AHP in project management". In: International Journal of Project Management 19.1 (2001), pp. 19–27. issn: 02637863. doi: 10.1016/S0263-7863(99)00038-1.

[92] Tarek Zayed, Mohamed Amer, and Jiayin Pan. "Assessing risk and uncertainty inherent in Chinese highway projects using AHP". In: International Journal of Project Management 26.4 (2008), pp. 408–419. issn: 02637863. doi: 10.1016/j.ijproman.2007.05.012.

[93] M. El-Mikawi and A.S. Mosallam. "A methodology for evaluation of the use of advanced composites in structural civil engineering applications". In: Composites Part B: Engineering 27.3-4 (1996), pp. 203–215. issn: 13598368. doi: 10.1016/1359-8368(95)00030-5.

[94] Jui Sheng Chou. "Applying AHP-Based CBR to Estimate Pavement Maintenance Cost". In: Tsinghua Science and Technology 13.SUPPL. 1 (2008), pp. 114–120. issn: 10070214. doi: 10.1016/S1007-0214(08)70136-6.

[95] E.K. Zavadskas, Z. Turskis, and J. Tamosaitiene. "Selection of construction enterprises management strategy based on the SWOT and multi-criteria analysis". In: Archives of Civil and Mechanical Engineering 11.4 (2011), pp. 1063–1082. issn: 16449665. doi: 10.1016/S1644-9665(12)60096-X.

[96] Bahareh Reza, Rehan Sadiq, and Kasun Hewage. "Sustainability assessment of flooring systems in the city of Tehran: An AHP-based life cycle analysis". In: Construction and Building Materials 25.4 (2011), pp. 2053–2066. issn: 09500618. doi: 10.1016/j.conbuildmat.2010.11.041.

[97] Yu Ting Lai, Wei Chih Wang, and Han Hsiang Wang. "AHP- and simulation-based budget determination procedure for public building construction projects". In: Automation in Construction 17.5 (2008), pp. 623–632. issn: 09265805. doi: 10.1016/j.autcon.2007.10.007.

[98] Chun Chang Lin, Wei Chih Wang, and Wen Der Yu. "Improving AHP for construction with an adaptive AHP approach (A3)". In: Automation in Construction 17.2 (2008), pp. 180–187. issn: 09265805. doi: 10.1016/j.autcon.2007.03.004.

[99] K. Nassar, Walid Thabet, and Yvan Beliveau. "A procedure for multi-criteria selection of building assemblies". In: Automation in Construction 12.5 SPEC. (2003), pp. 543–560. issn: 09265805. doi: 10.1016/S0926-5805(03)00007-4.

[100] Christof Knoeri, Claudia R. Binder, and Hans Joerg Althaus. "Decisions on recycling: Construction stakeholders' decisions regarding recycled mineral construction materials". In: Resources, Conservation and Recycling 55.11 (2011), pp. 1039–1050. issn: 09213449. doi: 10.1016/j.resconrec.2011.05.018.

[101] P. Kayastha, M. R. Dhital, and F. De Smedt. "Application of the analytical hierarchy process (AHP) for landslide susceptibility mapping: A case study from the Tinau watershed, west Nepal". In: Computers and Geosciences 52 (2013), pp. 398–408. issn: 00983004. doi: 10.1016/j.cageo.2012.11.003.

[102] G. S. Kalamaras et al. "Application of multicriteria analysis to select the best highway alignment". In: Tunnelling and Underground Space Technology 15.4 (2000), pp. 415–420. issn: 08867798. doi: 10.1016/S0886-7798(01)00010-4.

[103] L Hjalmarsson and J Odeck. "Efficiency of trucks in road construction and maintenance: An evaluation with data envelopment analysis". In: Computers & Operations Research 23.4 (1996), pp. 393–404. issn: 03050548. doi: 10.1016/0305-0548(95)00047-X.

[104] A. Charnes, W. W. Cooper, and E. Rhodes. "Measuring the efficiency of decision making units". In: European Journal of Operational Research 2.6 (1978), pp. 429–444. issn: 03772217. doi: 10.1016/0377-2217(78)90138-8.

[105] Mohammad S. El-Mashaleh, Shaher M. Rababeh, and Khalied H. Hyari. "Utilizing data envelopment analysis to benchmark safety performance of construction contractors". In: International Journal of Project Management 28.1 (2010), pp. 61–67. issn: 02637863. doi: 10.1016/j.ijproman.2009.04.002.

[106] Nikolai Bobylev. "Comparative analysis of environmental impacts of selected underground construction technologies using the analytic network process". In: Automation in Construction 20.8 (2011), pp. 1030–1040. issn: 09265805. doi: 10.1016/j.autcon.2011.04.004.

[107] Shih Tong Lu, Cheng Wei Lin, and Ping Hui Ko. "Application of Analytic Network Process (ANP) in assessing construction risk of urban bridge project". In: Second International Conference on Innovative Computing, Information and Control, ICICIC 2007 October 2007 (2008). doi: 10.1109/ICICIC.2007.172.

[108] Jin Wang, Yujie Xu, and Zhun Li. "Research on project selection system of pre-evaluation of engineering design project bidding". In: International Journal of Project Management 27.6 (2009), pp. 584–599. issn: 02637863. doi: 10.1016/j.ijproman.2008.10.003.

[109] Hong Yan Yan. "The construction project bid evaluation based on gray relational model". In: Procedia Engineering 15 (2011), pp. 4553–4557. issn: 18777058. doi: 10.1016/j.proeng.2011.08.855.

[110] J Hokkanen and P Salminen. "Choosing a solid waste management system using multicriteria decision analysis". In: European Journal of Operational Research 98.1 (1997), pp. 19–36. issn: 03772217. doi: 10.1016/0377-2217(95)00325-8.

[111] Georgios Banias et al. "Assessing multiple criteria for the optimal location of a construction and demolition waste management facility". In: Building and Environment 45.10 (2010), pp. 2317–2326. issn: 03601323. doi: 10.1016/j.buildenv.2010.04.016.

[112] C. Martin, Y. Ruperd, and M. Legret. "Urban stormwater drainage management: The development of a multicriteria decision aid approach for best management practices". In: European Journal of Operational Research 181.1 (2007), pp. 338–349. issn: 03772217. doi: 10.1016/j.ejor.2006.06.019.

[113] M. M. Marzouk. "ELECTRE III model for value engineering applications". In: Automation in Construction 20.5 (2011), pp. 596–600. issn: 09265805. doi: 10.1016/j.autcon.2010.11.026.

[114] Ching-Lai Hwang, Young-Jou Lai, and Ting-Yun Liu. "A new approach for multiple objective decision making". In: Computers & Operations Research 20.8 (1993), pp. 889–899. issn: 03050548. doi: 10.1016/0305-0548(93)90109-V.

[115] Bariş Şimşek, Yusuf Tansel Iç, and Emir H. Şimşek. "A TOPSIS-based Taguchi optimization to determine optimal mixture proportions of the high strength self-compacting concrete". In: Chemometrics and Intelligent Laboratory Systems 125 (2013), pp. 18–32. issn: 01697439. doi: 10.1016/j.chemolab.2013.03.012.

[116] Sazzadur Rahman et al. "Product-cost modelling approach for the development of a decision support system for optimal roofing material selection". In: Expert Systems with Applications 39.8 (2012), pp. 6857–6871. issn: 09574174. doi: 10.1016/j.eswa.2012.01.010.

[117] A. Kaklauskas, E. K. Zavadskas, and V. Trinkunas. "A multiple criteria decision support on-line system for construction". In: Engineering Applications of Artificial Intelligence 20.2 (2007), pp. 163–175. issn: 09521976. doi: 10.1016/j.engappai.2006.06.009.

[118] Arturas Kaklauskas et al. "Selection of low-e windows in retrofit of public buildings by applying multiple criteria method COPRAS: A Lithuanian case". In: Energy and Buildings 38.5 (2006), pp. 454–462. issn: 03787788. doi: 10.1016/j.enbuild.2005.08.005.

[119] Edmundas Kazimieras Zavadskas et al. "Multicriteria selection of project managers by applying grey criteria". In: Technological and Economic Development of

Economy 14.4 (2008), pp. 462–477. issn: 1392-8619. doi: 10.3846/1392-8619.2008.14.462-477.

[120] HELUZ. HELUZ - bricks, lintels, chimneys, ceiling systems for constructions of family houses. 2019. url: www.heluz.com.

[121] Haipeng Han, Farid Taheri, and Neil Pegg. "Quasi-static and dynamic crushing behaviors of aluminum and steel tubes with a cutout". In: Thin-Walled Structures 45.3 (2007), pp. 283–300. issn: 02638231. doi: 10.1016/j.tws.2007.02.010.

[122] Petr Máca, Radoslav Sovják, and Petr Konvalinka. "Impact Testing of Concrete: The Measurement Device". In: International Journal of Civil and Structural Engineering– IJCSE 1.4 (2014), pp. 20–24. issn: 2372-3971. doi: 10.15224/978-1-63248-025-5-66.

[123] Marcus Hering and Manfred Curbach. "A new testing method for textile reinforced concrete under impact load". In: MATEC Web of Conferences 199 (2018), p. 11010. doi: 10.1051/matecconf/201819911010.

[124] S. K. Al-Oraimi and A. C. Seibi. "Mechanical characterisation and impact behaviour of concrete reinforced with natural fibres". In: Composite Structures 32.1-4 (1995), pp. 165–171. issn: 02638223. doi: 10.1016/0263-8223(95)00043-7.

[125] R. Yu et al. "Impact resistance of a sustainable Ultra-High Performance Fibre Reinforced Concrete (UHPFRC) under pendulum impact loadings". In: Construction and Building Materials 107 (2016), pp. 203–215. issn: 09500618. doi: 10.1016/j.conbuildmat.2015.12.157.

[126] Nabim Alem and Matthew Perry. Design of Digital Low-pass Filters for Time-Domain Recursive Filtering of Impact Acceleration Signals. Tech. rep. 95. United States Army Aeromedical Research Laboratory, 1995, pp. 1–30.

[127] Warren N Hardy et al. "A Study of the Response of the Human Cadaver Head to Impact". In: Stapp Car Crash Journal 51.October (2007), pp. 17–80. issn: 1532-8546. doi: 10.1016/j.bbi.2008.05.010.

[128] Stephanie M. Beeman, Andrew R. Kemper, and Stefan M. Duma. "Neck forces and moments of human volunteers and post mortem human surrogates in low-speed frontal sled tests". In: Traffic Injury Prevention 17.S1 (2016), pp. 141–149. issn: 1538957X. doi: 10.1080/15389588.2016.1205190.

[129] Dinu Covaciu and Sorin Dima. "Crash Tests Data Acquisition and Processing". In: International Congress of Automotive and Transport Engineering. 2017, pp. 782–789. isbn: 978-3-319-45446-7. doi: 10.1007/978-3-319-45447-4.

[130] IDT Vision. The Motion Studio Software. url: www.idtvision.com/products/software/motion-studio/.

[131] National Instrument. LabVIEW. url: www.ni.com/labview.

[132] Jafar Rouzegar et al. "Geometrical discontinuities effects on lateral crushing and energy absorption of tubular structures". In: Materials and Design 65 (2015), pp. 343–359. issn: 18734197. doi: 10.1016/j.matdes.2014.09.041.

[133] Yonghui Wang and J. Y Richard Liew. "Blast performance of water tank with energy absorbing support". In: Thin-Walled Structures 96 (2015), pp. 1–10. issn: 02638231. doi: 10.1016/j.tws.2015.07.022.

[134] S. Boria, A. Scattina, and G. Belingardi. "Axial energy absorption of CFRP truncated cones". In: Composite Structures 130 (2015), pp. 18–28. issn: 02638223. doi: 10.1016/j.compstruct.2015.04.026.

[135] Zou Meng et al. "The energy absorption of bamboo under dynamic axial loading". In: Thin-Walled Structures 95 (2015), pp. 255–261. issn: 02638231. doi: 10.1016/j.tws.2015.06.017.

[136] M.G. Alexander and K. Stanish. “Durability design and specification of reinforced concrete structures using a multi-factor approachTitle”. In: Third Int. Conference on Construction Materials (2005).

[137] Kay Wille and Christopher Boisvert-Cotulio. “Material efficiency in the design of ultra-high performance concrete”. In: Construction and Building Materials 86 (2015), pp. 33–43. issn: 09500618. doi: 10.1016/j.conbuildmat.2015.03.087.

[138] K. Wille, A.E. Naaman, and G.J. Parra-Montesinos. “Ultra-high performance concrete with compressive strength exceeding 150 MPa (22 ksi): a simpler way”. In: ACI Materials Journal (2011), pp. 46–54.

[139] J. Xie, A.E. Elwi, and J.G. MacGregor. “Mechanical properties of three high-strength concretes containing silica fume”. In: ACI Materials Journal (1995).

[140] Petr Máca, Radoslav Sovják, and Tomáš Vavřiník. “Experimental Investigation of Mechanical Properties of UHPFRC”. In: Procedia Engineering 65.0 (2013), pp. 14–19. doi: 10.1016/j.proeng.2013.09.004.

[141] P.K. Mehta. “Concrete technology at the crossroads–problems and opportunities”. In: ACI Special Publication 144 (1994), pp. 1–30.

[142] J Marchand et al. “The frost durability of high-performance concrete”. In: Concrete Under Severe Conditions: Environmental and Loading 1 (1995), p. 273. issn: 0419198504.

[143] Michel Pigeon et al. “Freezing and thawing tests of high-strength concretes”. In: Cement and Concrete Research 21.5 (Sept. 1991), pp. 844–852. issn: 00088846. doi: 10.1016/0008-8846(91)90179-L.

[144] Göran Fagerlund. “Frost resistance of high performance concrete–some theoretical considerations: a contribution to RILEM-3C-Workshop" Durability of high performance concrete", Wien 14th-15th February, 1994”. In: Report TVBM (1993). issn: 0348-7911.

[145] Benjamin A Graybeal. “Compressive behavior of ultra-high-performance fiber-reinforced concrete”. In: ACI Materials Journal 104.2 (2007), p. 146.

[146] Zdeňka Bažantová et al. “Multi-Functional High-performance Cement Based Composite”. In: Key Engineering Materials 677 (2016), pp. 53–56. doi: 10.4028/www.scientific.net/KEM.677.53.

[147] Zdeňka Bažantová et al. “Controlled Hardening of Silicate Binders for the Optimization of High Performance Composites”. In: Key Engineering Materials 722 (2016), pp. 281–285. doi: 10.4028/www.scientific.net/KEM.722.281.

[148] Karel Kolář et al. “Measurement of Volume Changes of High Performance Cement Based Composites”. In: Applied Mechanics and Materials. Vol. 827. Trans Tech Publications, Feb. 2016, pp. 328–331. isbn: 978-3-03835-531-1. doi: 10.4028/www.scientific.net/AMM.827.328.

[149] J.O. Hallquist. LS-DYNA Theory manual. Livermore, California: Livermore Software Technology Corporation, 2006. isbn: 0-9778540-0-0.

[150] Yvonne Murray. “Users Manual for LS-DYNA Concrete Material Model 159”. In: Federal Highway Administration May (2007), p. 77.

[151] LSTC. LS-DYNA Keyword User’s Manual Volume I R7.1. Vol. I. 2014. isbn: 9254492507.

[152] Yvonne Murray, Akram Abu-Odeh, and Roger Bligh. “Evaluation of LS-DYNA Concrete Material Model 159”. In: May (2007), p. 190.

[153] Stavros Gaitanaros and Stelios Kyriakides. “On the effect of relative density on the crushing and energy absorption of open-cell foams under impact”. In: International Journal of Impact Engineering 82 (2015), pp. 3–13. issn: 0734743X. doi: 10.1016/j.ijimpeng.2015.03.011.

[154] M. Shojaati. “Correlation between injury risk and impact severity index ASI”. In: 3rd Swiss Transport Research Conference. Zurich, 2003.

[155] M. Borovinšek et al. “Simulation of crash tests for high containment levels of road safety barriers”. In: Engineering Failure Analysis 14.8 SPEC. ISS. (2007), pp. 1711–1718. issn: 13506307. doi: 10.1016/j.engfailanal.2006.11.068.

[156] Z. Ren and M. Vesenjak. “Computational and experimental crash analysis of the road safety barrier”. In: Engineering Failure Analysis 12.6 SPEC. ISS. (2005), pp. 963–973. issn: 13506307. doi: 10.1016/j.engfailanal.2004.12.033.

[157] Mariusz Pawlak. “The Acceleration Severity Index in the impact of a vehicle against permanent road equipment support structures”. In: Mechanics Research Communications 77 (2016), pp. 21–28. issn: 00936413. doi: 10.1016/j.mechrescom.2016.08.005.

[158] Carlos Roque and João Lourenço Cardoso. “Observations on the relationship between european standards for safety barrier impact severity and the degree of injury sustained”. In: IATSS Research 37.1 (2013), pp. 21–29. issn: 03861112. doi: 10.1016/j.iatssr.2013.04.002.

[159] Richard Sturt and Christina Fell. “The relationship of injury risk to accident severity in impacts with roadside barriers”. In: International Journal of Crashworthiness 14.2 (2009), pp. 165–172. doi: 10.1080/13588260802614365.

[160] Nikil Abraham et al. “Assessment of the impact speed and angle conditions for the EN1317 barrier tests”. In: International Journal of Crashworthiness 21.3 (2016), pp. 211–221. issn: 17542111. doi: 10.1080/13588265.2016.1164444.

[161] Douglas Gabauer and Hampton Gabler. “Evaluation of Threshold Values of Acceleration Severity Index by Using Event Data Recorder Technology”. In: Transportation Research Record 1904 (2005). doi: 10.3141/1904-04.

[162] Jasper Chell et al. “Limitations of the European barrier crash testing regulation relating to occupant safety”. In: Accident Analysis and Prevention 133.July (2019), p. 105239. issn: 00014575. doi: 10.1016/j.aap.2019.07.015.

[163] Graeme D Weaver and Eugene L Marquis. “Safety aspects of roadside slope combinations”. In: 53rd Annual Meeting of the Highway Research Board. Washington District of Columbia, US, 1975, pp. 25–28.

[164] European Standard EN 1317-1, Road restraint systems - Part 1: Terminology and general criteria for test methods.

[165] European Standard EN 1317-2, Road restraint systems - Part 2: Performance classes, impact test acceptance criteria and test methods for safety barriers including vehicle parapets.

[166] European Standard EN 12767:2007, Passive safety of support structures for road equipment - Requirements and test methods.

[167] European Standard EN 1317-3, Road restraint systems - Part 3: Performance classes, impact test acceptance criteria and test methods for crash cushions.